Advances in Quantitative Susceptibility Mapping for Human Brain: Applications in Hemorrhage, Motion, Blood Vessels

by

Ashmita De

A thesis submitted in partial fulfillment of the requirements for the degree of

Doctor of Philosophy

Department of Biomedical Engineering

University of Alberta

Abstract

Quantitative Susceptibility Mapping (QSM) is an emerging postprocessing method, computed from phase images, which is finding wide application in quantifying iron content in healthy and pathological tissue. However, QSM is still not commonly used in clinical practice. This thesis discusses the challenges that come during the application of QSM to patient studies and makes advances to solve problems such as long acquisition times, motion, and works towards finding more applications for QSM. The focus for this work is on stroke applications where methods such as Susceptibility Weighted Imaging (SWI) and Time-of-Flight (TOF) MR Angiography (MRA) are already used.

SWI finds one application in the study of hemorrhage, and it has been shown in previous studies that QSM can be reconstructed from the single echo SWI sequence. However, whole brain SWI requires an acquisition time of about 5 mins which is often too long for hemorrhagic patients to remain still inside the scanner. In Chapter 2, a rapid single-shot Echo-planar Imaging (EPI) sequence with acquisition time of 0.45 mins was applied to subjects with intracerebral hemorrhage (ICH) which enabled rapid measurement of ICH area and mean magnetic susceptibility, with reduced motion as compared to standard SWI. EPI requires minimal additional acquisition time and hence can be incorporated into iron tracking studies in ICH.

Motion effects cause artifacts in magnitude as well as phase images. Hence, Chapter 3 investigates the quantitative effects of movement and respiratory fluctuations on QSM in the brain. QSM was found to be more sensitive to motion caused by movement than magnitude images and thus post-processing motion correction or faster sequences may be beneficial for QSM applications. However, respiratory fluctuations did not cause statistically significant differences in susceptibility values in group study; although, these variations might be considered important in individual follow-up studies.

SWI is widely used in the study of veins, hematoma, lesions etc. However, since it uses filtered phase for its computation, SWI has certain limitations such as artifacts arising from phase wraps, blooming effects, dependence of phase value on the orientation of object with main magnetic field etc. In order to overcome SWI limitations, a new method called quantitative susceptibility weighted imaging also known as true susceptibility weighted imaging (tSWI), has been recently introduced which uses susceptibility maps instead of filtered phase. Chapter 4 aims at optimizing tSWI parameters for strong susceptibility sources like hemorrhage and investigates the benefits and limitations of tSWI for hemorrhages. In hemorrhage, tSWI minimizes both blooming effects and phase wrap artifacts observed in SWI. However, unlike SWI, tSWI requires an alteration in the threshold limits for best hemorrhage depiction that greatly differs from the standard values. tSWI can be used as a complementary technique for visualizing hemorrhages along with SWI.

It is always desirable to obtain maximum information from a single acquisition. Hence in Chapter 5, a new sequence has been introduced to simultaneously compute TOF-MRA, QSM, SWI and transverse relaxation rate R2* while maintaining all the key features of standard TOF-MRA such as multiple overlapping thin slab acquisition (MOTSA), ramped RF pulses and venous saturation. The effect of these TOF features on QSM and SWI was studied. The proposed sequence with the

TOF features provided TOF-MRA and SWI with similar CNRs to standard methods. The mean susceptibility values for brain structures had no significant susceptibility variation between the proposed and standard methods as well. Thus, this sequence is able to provide similar TOF-MRA to standard TOF methods while enabling additions of SWI, R2* and QSM.

Preface

A version of Chapter 2 has been published in the Journal of Magnetic Resonance Imaging as: A. De, H. Sun, D. J. Emery, K. S. Butcher, and A. H. Wilman, "Rapid quantitative susceptibility mapping of intracerebral hemorrhage," J. Magn. Reson. Imaging JMRI, vol. 51, no. 3, pp. 712–718, Mar. 2020, doi: 10.1002/jmri.26850.

A part of Chapter 3 has been presented at ISMRM as: A. De, H. Sun, A. Elkady, P. Seres and A. H. Wilman, "Effects of Motion in Quantitative Susceptibility Mapping of Brain", ISMRM, Paris, France, 2018. ISMRM, Paris, France, 2018.

A version of Chapter 4 has been accepted for publication in Magnetic Resonance Imaging with author list and title as: A. De, H. Sun, D. J. Emery, K. S. Butcher, and A. H. Wilman," Quantitative susceptibility-weighted imaging in presence of strong susceptibility sources: Application to hemorrhage".

A version of Chapter 5 is under review in Magnetic Resonance in Medicine with author list and title as: A. De, J. Grenier and A. H. Wilman," Simultaneous Time-of-Flight (TOF) MR

Angiography and Quantitative Susceptibility Mapping (QSM) without compromising TOF features".

A version of Appendix A has been presented at ISMRM as: A. De, H. Sun, K. S. Butcher, and A. H. Wilman, "Application of Fourier-domain Analysis Based Unwrapping Technique in Quantitative Susceptibility Mapping (QSM) of Intracerebral Hemorrhage", ISMRM, Virtual, 2020.

Data collection for stroke patients were performed by Dr. Kenneth Butcher's group. All other scans were acquired by the author, with assistance from Peter Seres or Justin Grenier. Dr. Alan Wilman supervised and provided guidance for all works done in this thesis. MATLAB (Mathworks Inc) codes for computing QSM were inherited from past graduate student Dr. Hongfu Sun, which served as a starting point for further modification. QSM codes were modified by the author to optimize the method in order to obtain accurate susceptibility values for the specific applications in this thesis. Justin Grenier assisted the author with sequence modifications made on IDEA (version VE11C, Siemens Healthcare). All other post-processing and analysis of MRI data done in this thesis was performed by the author.

The research projects, of which this thesis is a part, received research ethics approval from the University of Alberta Research Ethics Board, Project Name MRI in Neurological Disease Pro00000906.

Acknowledgements

I would like to thank my supervisor Dr. Alan Wilman for his guidance, mentorship and advice throughout my program. His insightful feedback has been invaluable for my research. Moreover, I am extremely grateful for his immense support and patience during the pandemic. I would also like to thank my committee members: Dr. Richard Thompson and Dr. Atiyah Yahya for their valuable feedback. I am also thankful to my examiners Dr. Keith Wachowicz, Dr. Alexander Rauscher and the exam chair Dr. Christian Beaulieu.

I would like to thank Justin Grenier, Peter Seres and Karim Damji for assisting me with MRI experiments and sharing their knowledge with me. I am thankful to past and present lab members for helping me in various ways during my PhD program. And of course, a big thanks to all my friends, family and loved ones who have supported and encouraged me over all these years.

And finally, I want to express my gratitude and thank my parents for their constant love, support, and encouragement throughout this journey.

Table of Contents

List of Tables

List of Figures

Chapter 1

Introduction

1.1 Overview of Magnetic Resonance Imaging (MRI)

The purpose of this introduction is to provide a brief overview of the principles of the imaging modality called MRI [1]–[4]. MRI is a non-invasive imaging technique sensitive to a broad range of tissue properties. MRI techniques have helped in understanding the anatomy and functionality of the human body. Alongside research, this imaging modality has found its place in clinical application for diagnosis of diseases. MRI can generate images having different contrasts with a considerably high resolution which has helped in the study of the human body. MRI originates from the concept of nuclear magnetic resonance (NMR). The principle of MRI is based on the interaction of the proton in the hydrogen atom with an external magnetic field. Since a major part of the human body is composed of water this creates an abundance of hydrogen protons. Each hydrogen proton has its own nuclear spin and angular momentum. In absence of an external magnetic field, the spins are oriented in random directions; however, when exposed to an external

static magnetic field, B_0 the individual magnetic moment vectors tend to align with or against the field, producing a net longitudinal magnetization aligned with the field, while the transverse components precess about the field direction with random phase leading to no net transverse magnetization. The spins exhibit a motion similar to a spinning gyroscope. The precession angular frequency for the proton is given by:

$$\omega_0 = \gamma * B_0 \quad \ldots\ldots\ldots\ldots \quad (1.1)$$

where γ is called the gyromagnetic ratio. The above equation is referred to as the Larmor equation and ω_0 is called the Larmor frequency. This precession happens around the main magnetic field (B_0) i.e. the z axis and at equilibrium and as mentioned the net transverse component sums up to be zero due to the spins having different phases.

In order to detect the spins, a radio frequency (RF) wave is applied perpendicular to the B_0 direction which tips the longitudinal spin magnetization into the transverse plane. The precession in the transverse plane can be detected using a receiver coil that picks up the magnetic flux created by the oscillating transverse magnetization; however, the spins tend to return to their original equilibrium position causing the transverse magnetization to decay away. This occurs due to longitudinal relaxation (dependent on T1) and transverse relaxation (dependent on T2).

Longitudinal relaxation, also called the T1 relaxation or the spin-lattice relaxation, is a process that occurs due to energy exchange between the spins and the lattice. This occurs as the spins tend to return to their original aligned position to maintain thermal equilibrium resulting in recovery of the longitudinal magnetization. Transverse relaxation, also known as T2 relaxation or spin-spin relaxation, is a result of loss of phase coherence of the spins following the excitation. Interaction between spins and B_0 inhomogeneities result in dephasing and loss of coherence of the spins thus causing decrease in the transverse magnetization. The transverse relaxation occurs as a combined

effect of static and dynamic processes. The apparent or observed rate of relaxation T2* is expressed as:

$$\frac{1}{T2*} = \frac{1}{T2'} + \frac{1}{T2} \quad \text{..... (1.2)}$$

In eq (1.2), T2' is the decay time for the static processes caused by B_0 imperfections, susceptibility variations and chemical shift. T2 is the decay time for the dynamic processes caused by thermodynamic spin-spin interaction.

These relaxation times also determine the contrast of the acquired images. The acquired signal measurements are then mapped to spatial locations by applying gradient pulses.

Gradient pulses are utilized to perform spatial encoding which allows the localization of signal from a small region.

1.2 Pulse Sequence and Signal Acquisition

The basic components of a pulse sequence comprise an excitation RF wave, and spatial encoding gradients applied before and during data acquisition. These components are played out at specific timings to acquire the desired MRI contrast and are displayed in Figure 1.1.

Depending on the purpose of the data acquisition, the timing and location of these components can be varied to design different pulse sequences. This thesis primarily studies images acquired using different variations of a Gradient Recalled Echo (GRE) sequence.

1.2.1 Gradient Recalled Echo Sequence

In a GRE sequence, the static sources for proton dephasing, such as magnetic field inhomogeneity and magnetic susceptibility differences, contribute to the signal decay. Hence, the echo time, TE

determines the amount of T2* weighting in a gradient echo image. This sequence is commonly used for phase imaging. Variations of GRE are used to acquire images to compute Susceptibility Weighted Imaging (SWI), Quantitative Susceptibility Mapping (QSM), and Time-of-Flight (TOF) angiography, which are all applied in this thesis.

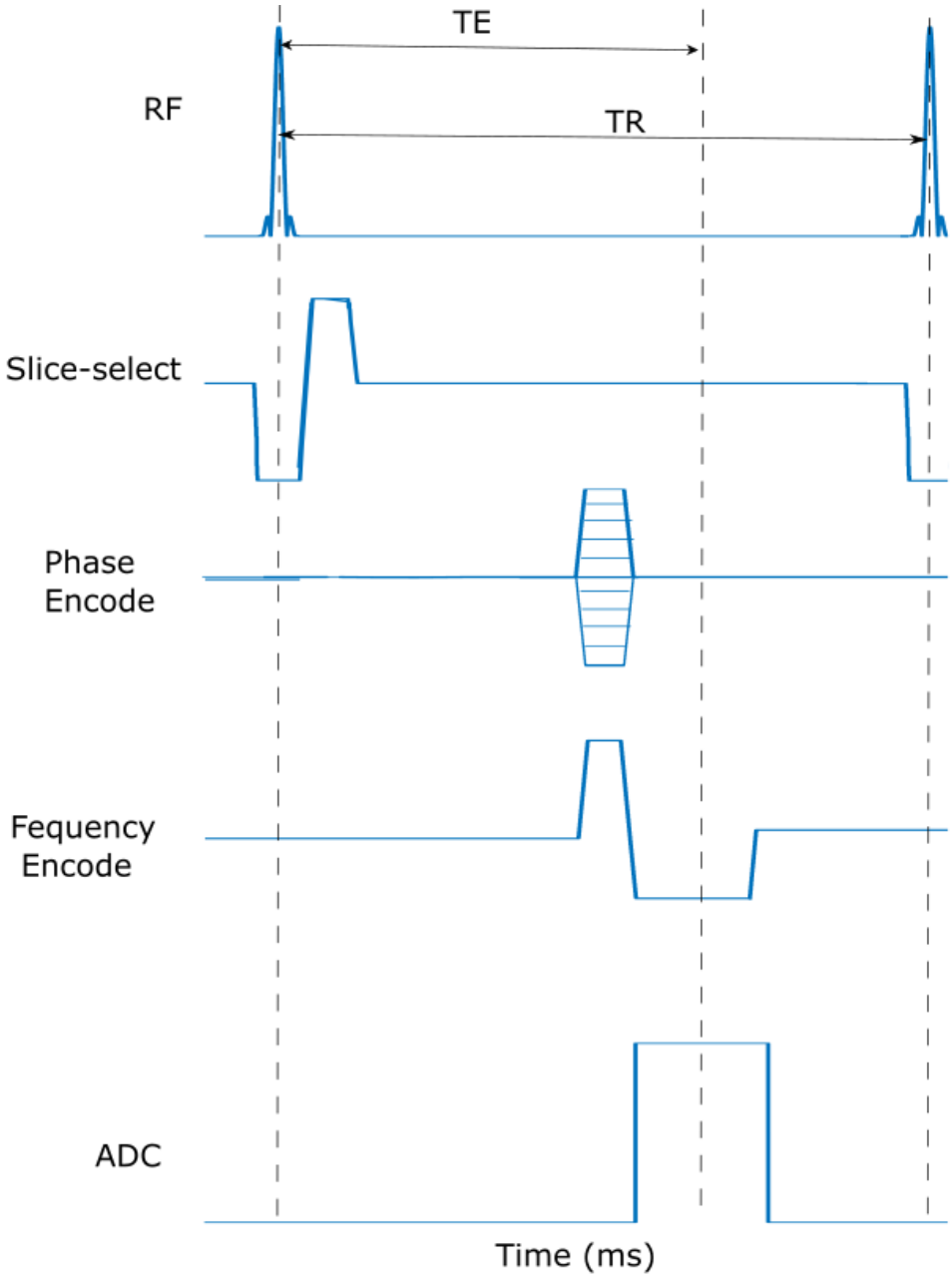

Figure 1.1: Timing diagram of a simple 2D gradient-echo sequence.

The simplest GRE sequence consists of a slice-selective RF pulse, a slice selection gradient pulse, a frequency encoding gradient pulse (readout), a phase encoding gradient pulse and the output readout acquisition.

The RF is turned on during the slice-select gradient. The RF pulse is typically applied at the resonant frequency with an envelope that defines both the resulting flip angle and the shape of the RF profile. A standard RF pulse could be a weighted truncated sinc function, for instance; however, depending on the application, different kinds of RF pulses are used. For example, in TOF angiography, a ramped RF is used. Once the RF pulse is completed, the slice-select gradient is rewound in order to rewind the added dephasing of the transverse signal. The phase encoding gradient follows and varies for each repetition of the pulse sequence. This is followed by the frequency encoding gradient during which the signal generated is recorded. The raw signal (k-space data) received is Fourier transformed to produce data in image space. The data obtained is in complex form with a real and imaginary part. Thus, magnitude and phase images are produced. Magnitude images are the most widely utilized form. Phase images from the GRE sequences give extra insight into the magnetic field variations and are useful to study susceptibility effects.

Images with different contrasts can be produced by altering acquisition timings, particularly the echo time TE and repetition time TR, but also the amplitude, duration and timing of the gradients. Sometimes GRE sequences are obtained with multiple echoes which can be formed by the addition of more gradients in the frequency encode direction. Multi-echo and single echo GREs are utilized for R2* mapping and QSM computations. Sometimes flow compensation gradients are added to nullify the effects of flow in blood vessels [5]. Flow compensation gradients are used in SWI and TOF sequences which have been discussed in the next section. Another variation of GRE is the Echo-planar imaging (EPI) sequence which has been studied in the thesis. This is a rapid gradient

echo sequence and QSM can be computed from data obtained from EPI sequence [6]. In the EPI sequence as shown in Figure 1.2, the image is acquired using a set of echoes after the RF excitation with small phase encode gradients between the read out echoes. The corresponding k-space data is shown in Figure 1.3, and for comparison a GRE k-space acquisition is also shown. As it can be seen in Figure 1.3, for each TR only one line of k-space is acquired for a single echo GRE sequence whereas the corresponding EPI sequence has several lines of k-space acquired in one TR. Hence EPI sequences can acquire images with a much lower acquisition time.

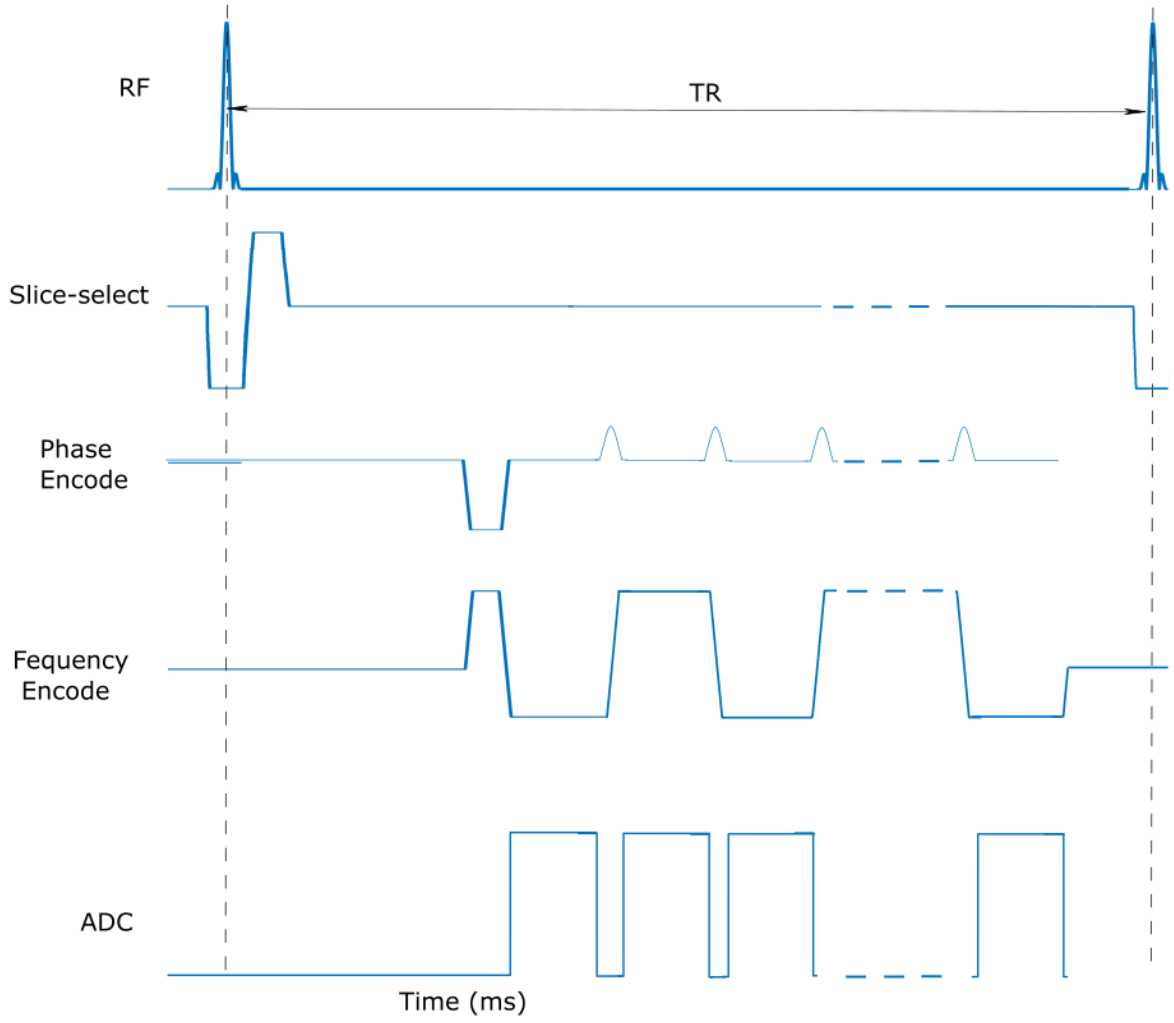

Figure 1.2: Sequence diagram showing the phase encoding and read gradient for an 2D EPI sequence.

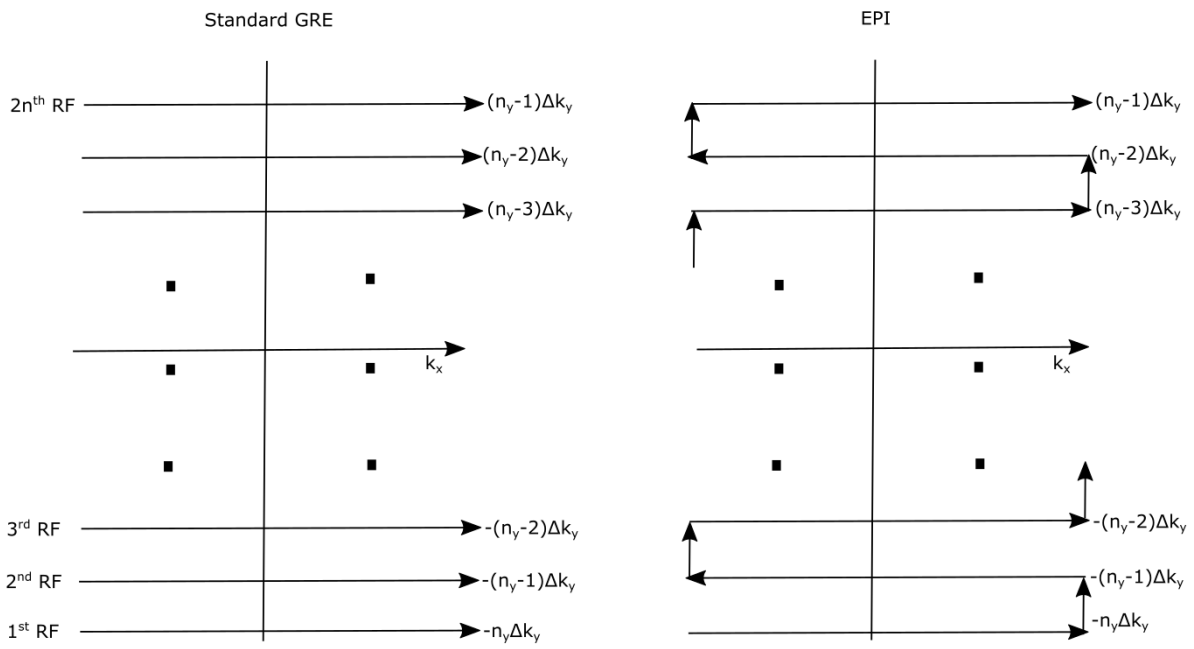

Figure 1.3: Showing temporal order of k-space covering for GRE and EPI.

The standard GRE sequence requires a new TR for each acquisition line, while single-shot EPI acquires all lines after one excitation.

1.2.2 Flow compensation

Several MRI sequences add flow compensation gradients in order to reduce artifacts caused by blood flow [5]. Flow artifacts may cause blurring or ghosting artifacts. The problem arises because the moving spins in blood are not receiving identical gradient encoding compared to stationary tissue. For example, if we apply a gradient pulse with amplitude G for a time t, the phase shift of the spins at a location r is given by:

$$\varphi(r) = \gamma \int G.\, r(t)\, dt \quad \ldots\ldots (1.3)$$

Now, if $r(t) = r_0 + vt$, with v being the velocity in the direction of G, the phase shift will be:

$$\varphi(r) = \gamma \int G.\, (r_0 + vt)\, dt = \gamma.G\, [r_0 t + vt^2/2] \neq 0 \quad \ldots\ldots (1.4)$$

This phase shift causes signal loss when the spins in the voxel do not move at the same rate. Also change in blood velocity over time (i.e. pulsatile flow) can cause ghosting effects by altering the phase shifts across the different k-space lines. Hence, flow compensation gradients are applied to null the first order gradient moments. For example, a simple bipolar gradient pulse has no net dephasing effect on static spins, yet spins moving in the gradient direction will not be fully refocused. The simplest means of flow compensation is the use of three gradient pulses to null both zero and first order components; however, flow compensation gradient extends the time of gradient playout.

1.3 Magnetic Susceptibility

A GRE sequence is utilized to acquire data to generate SWI and QSM images. These images help to study the magnetic susceptibility of tissues. When exposed to an external magnetic field, different materials behave in different manners depending on an intrinsic property of the material defined as magnetic susceptibility, χ. Magnetization can be defined as the amount of magnetic moment exerted by the magnetic field per unit mass or volume of an object. The magnetization, M that is induced in the material due to the applied magnetic field, H is defined as:

$$M = \chi * H \quad \text{(1.5)}$$

Susceptibility being independent of magnetic field strength and orientation can be used as a quantitative measure. On the basis of susceptibility, a substance can be classified as diamagnetic, paramagnetic and ferromagnetic. A major part of the human body is composed of water which has a susceptibility value of -9 ppm. Any change in the magnetic property of the material will cause a change in the local field, which can be manifested as a phase change. This phase change due to susceptibility effect can be measured at echo time, TE is given by:

$\Delta\varphi = -\gamma.\Delta B.TE$……...… (1.6)

where the field change ΔB can be defined as a function of susceptibility: $\Delta B = f(\Delta\boldsymbol{\chi}) = \Delta\boldsymbol{\chi}$. B_0 and B_0 is the external magnetic field. In order to study the susceptibility of tissues, acquisition of phase is required.

1.4 Susceptibility Weighted Imaging (SWI)

SWI is a post processing method where phase images are used to create filtered phase weighted masks which get multiplied into magnitude images to enhance susceptibility contrast. A 3D flow compensated GRE sequence is used to acquire the data for SWI reconstruction. The phase images are passed through a homodyne high pass filter to remove the low-spatial frequency components [7]. This filtered phase is then utilized to produce a phase mask as follows:

$$filtered\ phase\ mask = \begin{cases} \frac{\pi-\varphi}{\pi} & for\ \varphi > 0 \\ 1 & otherwise \end{cases}$$

……. (1.7)

The phase mask has values between zero and one. The mask is designed such that to set to unity when no change in magnitude is desired and to set to other numbers to decrease the signal intensity where phase takes certain values. Typically, the phase mask is multiplied to the magnitude four times to generate a susceptibility weighted image.

$SWI = mag * (filtered\ phase\ mask)^4$……...……...……..... (1.8)

A minimum intensity projection (mIP) can be utilized to observe the veins in resulting data. Figure 1.4 shows the SWI and mIP of a healthy volunteer along with the different components of SWI computation. SWI images provide better differentiation between gray and white matter than corresponding magnitude images. This method improves the visibility of paramagnetic

susceptibility sources such as hemorrhage, veins and microbleeds; hence, SWI finds extensive use in diagnosing several neurovascular and neurodegenerative diseases.

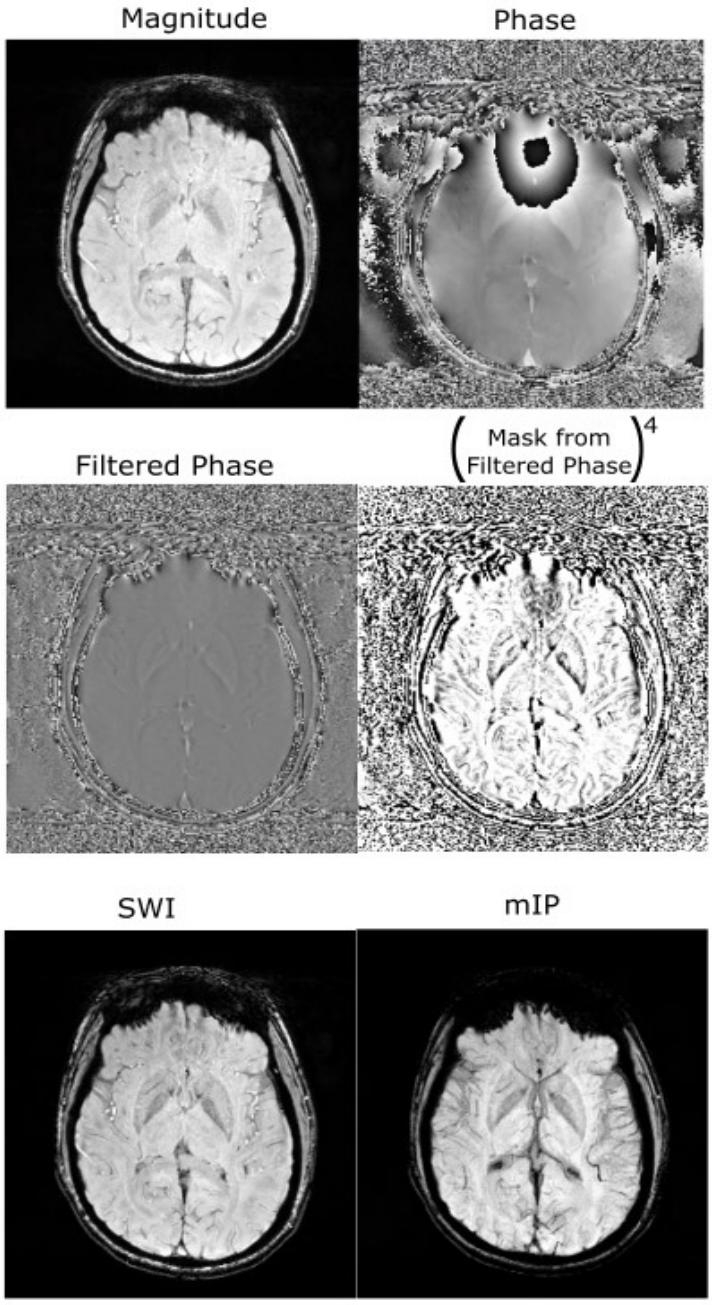

Figure 1.4: Magnitude, Phase, filtered phase, phase mask, SWI and mIP of a typical SWI of a healthy subject for venous imaging at 3 T using whole head coverage via 1.5-mm slices of 3D SWI.

1.5 Quantitative Susceptibility Mapping

Quantitative Susceptibility Mapping (QSM) is a postprocessing method that utilizes raw phase images obtained from a gradient echo sequence to produce susceptibility maps. The reconstruction steps of QSM involve multi-channel coil combination, phase unwrapping, background removal and dipole field inversion [8] as shown in Figure 1.5.

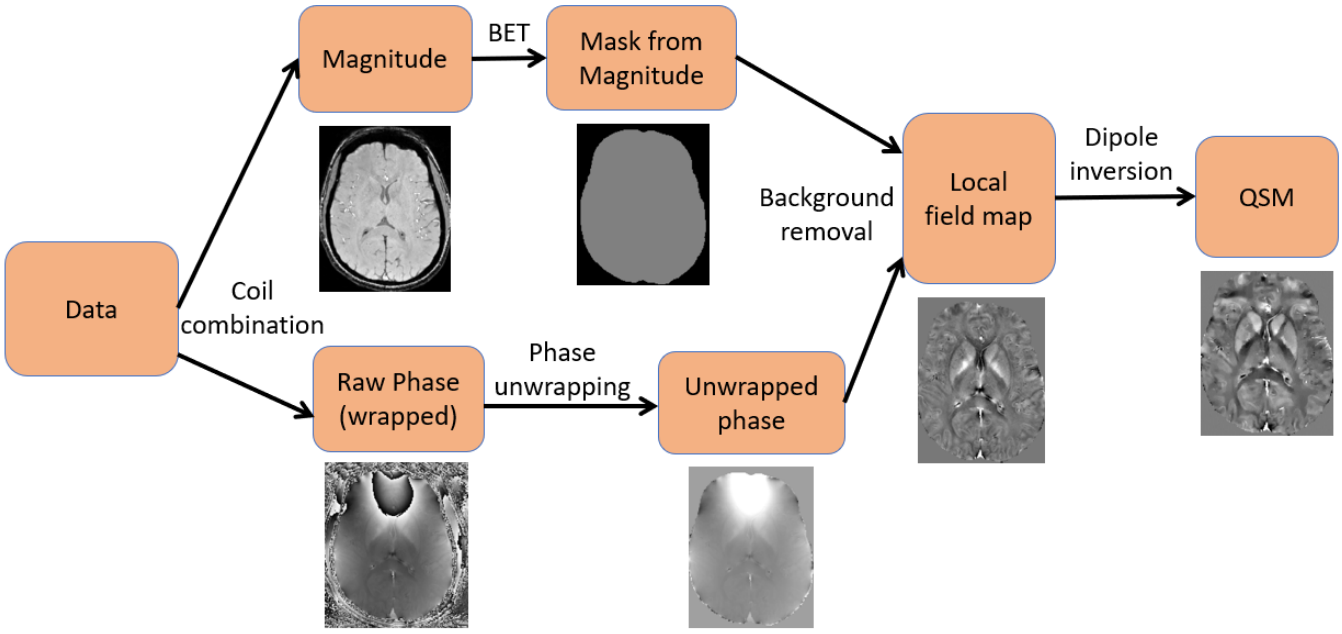

Figure 1.5: QSM computation steps.

1.5.1 Coil Combination

In current MRI scanners, multi-channel receiver coils are used to increase the SNR of the images and also reduce scan time by allowing parallel imaging. The simplest method of coil combination is the sum of squares of the signals from each coil element [9]. This method, though appropriate for magnitude images, does not produce accurate coil combinations for phase images. Along with

a dependence on field shift and echo time, the phase images get a different phase offset (φ_{IC}) from each channel which can cause improper coil combinations.

$\varphi = -\gamma.\Delta B.TE+\varphi_{IC}$ ..... (1.9)

Several methods have been proposed which address the phase offset when combining the phase [8], [10], [11]. Some of these coil combination methods include the Roemer method [12], [13] which estimates the receiver sensitivities by normalizing the head array data by using a body coil image, thus necessitating additional reference acquisitions. Dual echo methods make use of phase information from two different TEs to solve this problem [11], [14]. Combining Phase data using a Short Echo-time Reference scan (COMPOSER) method [15] employs a reference scan with short TE for sensitivity estimation and does not require a body coil acquisition. Singular Value Decomposition (SVD) technique [16] compresses the head array data into a virtual body coil, which is then used as a phase reference for coil sensitivity estimation [17]. For single echo phase data, an adaptive combining method can be used, without estimation of coil sensitivities [18]. In this thesis, the data acquired utilized the inbuilt adaptive coil combination from the 3T Siemens Prisma scanner unless otherwise mentioned.

1.5.2 Creating Brain Masks

Binary brain masks are generated to extract the region of interest which is the brain tissue in this thesis. The brain masks are generated from the magnitude images and are obtained by using Brain Extraction Tool (BET) [19] of FMRIB software library (FSL).

1.5.3 Phase Unwrapping

The phase is computed as the angle of the complex signal and hence the values cannot exceed $[-\pi,\pi)$. As this phase accumulates over time, the phase becomes aliased and wraps within the boundary limits. This results in discontinuous jumps in the phase values when the boundary limit is reached and thus causing phase wraps. Phase unwrapping is the method to remove these wraps and recover the phase information.

Several methods have been introduced for phase unwrapping [20]–[25]. The path-based methods like Phase Region Expanding Labeller for Unwrapping Discrete Estimates (PRELUDE) [20] and best path [23] unwrap the phase wraps by adding a multiple of 2π at the phase jump location. The Laplacian based method [21], [22] applies the Laplacian function in the Fourier domain to compute the true unwrapped phase value. In computation with multi-echo sequences, temporal phase correction can be made using the multiple echoes.

All these methods are widely used depending on the dataset. The second order derivatives in the Laplacian may cause difficulty in large phase changes. Hence, Laplacian methods have been found to underestimate regions with strong susceptibility sources [25] such as hemorrhage and veins. Hence, in this thesis path-based phase unwrapping was implemented using best path [23] and PRELUDE [20].

1.5.4 Background Removal

The total field perturbation observed is a result of the contribution from the local tissue susceptibility as well as other sources such as main field inhomogeneity, chemical shift and the dominant air-tissue susceptibility interfaces. In order to compute the local susceptibility values of

the tissue the field-to-susceptibility equation needs to be applied on the local field. The local field can be computed from the total field by removing the background field contribution using eq (1.10)

$$B_{local} = B_{total} - B_{background} \quad \ldots\ldots\ldots\ldots\ldots\ldots\ldots \quad (1.10)$$

Ths QSM step is known as background field removal. It can be performed by using different techniques such as homodyne high-pass filtering, projection onto dipole fields (PDF) [26], [27], Sophisticated Harmonic Artifact Removal for Phase data (SHARP) [28], [29], regularization-enabled sophisticated harmonic artifact reduction for phase data (RESHARP) [30], Laplacian Boundary Value (LBV) [31], Extended RESHARP (ESHARP) [32] and Variable-kernel SHARP (V-SHARP) [33], [34] etc.

While homodyne high-pass filtering is the easiest background removal approach, it removes all phase components in the low frequency spectrum, and thus some of the local field is removed. The PDF method decomposes the background field inside the brain tissue into a field originating from dipoles outside using a projection theorem. However, this method fails to remove background fields that do not originate from susceptibility dipoles outside the brain such as B_0 inhomogeneity from imperfect shimming. Then there are methods such as SHARP which attempt to solve this problem by utilizing the spherical mean value (SMV) property of harmonic functions. According to Maxwell's equations, the dipole field induced by sources outside the brain is harmonic across the brain [28]. By utilizing the SMV property of harmonic functions, the background field can be removed by convolving the total field with a non-negative, radially symmetric, normalized convolution kernel. However, results at the boundaries are not accurate for this method due to the violation of SMV theorem in locations where the kernel overlaps the brain edge. RESHARP [30] utilizes Tikhonov regularization in formulating the background field removal as an optimization problem. This method allows suppression of non-harmonic components and although it eliminates

the contribution of non-internal sources, it might remove the non-harmonic components of the local field as well. Both these methods have a common problem of erosion of the boundaries due to the convolution with the spherical kernel. VSHARP [33], [35], [36] employs varying sizes of spherical kernels to solve this problem. In this method, the kernel size is reduced when near the boundaries of the brain to preserve more brain regions. Similarly, ESHARP [32] tries to solve this problem by using the analytic property of the harmonic background field. In this method Taylor series is utilized to expand the edge-eroded background field. Laplacian Boundary Value (LBV) [31] utilizes Laplace's equation to solve the background removal problem. It is assumed that the background field is harmonic inside the brain and hence Laplace's equation inside the brain is given as:

$$\nabla^2 B_{bkg} = 0 \,\forall\, brain \quad \text{......} \quad (1.11)$$

And the non-harmonic local field satisfies the Poisson equation:

$$\nabla^2 B_{local} = f \,\forall\, brain \quad \text{......} \quad (1.12)$$

For a finite domain, a unique solution can be obtained to the Laplace's equation. Since the local field is significantly smaller than the background field, it is assumed that the background field at the boundary is equal to the total field. Under these assumptions, Laplace's equation is an elliptic partial differential equation [37] and the boundary problems can be solved using numerical schemes, such as finite difference methods [38].

1.5.5 Dipole Inversion

As discussed previously, the magnetization, M that is induced when a material with susceptibility χ is placed in an external magnetic field, B is defined as:

$$M = \chi . H = \chi . \frac{\boldsymbol{B}}{\mu} = \frac{\chi}{\mu_0(1+\chi)} B \quad \text{......} \quad (1.13)$$

μ is the permeability of material, μ_0 is the permeability of vacuum. The net induced magnetic field distribution can be expressed as [8]:

$$\Delta B(r) = \frac{\mu_0}{4\pi}\int d^3r'\{\frac{3M(r').(r-r')}{|r-r'|}(r-r') - \frac{M(r')}{|r-r'|^3}\}_{r\neq r'} \quad \text{..... (1.14)}$$

Now, when calculated in k-space using rotating frame of reference, this equation becomes:

$$\Delta B(k) = \frac{\mu_0}{3}\frac{3cos^2\beta - 1}{2}\,(M(k) - 3M_z(k)\,\hat{z}) \quad \text{..... (1.15)}$$

Where $\hat{z}$ is the unit vector in z-direction and β is the angle between k and $\hat{z}$.

Hence, $cos^2\beta = \frac{k_z^2}{k_x^2+k_y^2+k_z^2}$

For MRI, some assumptions can be made to simplify the equations.

In eq(1.12), the susceptibility values of brain tissues are much less than 1, hence:

$$M \approx \frac{\chi}{\mu_0}B \quad \text{.....(1.16)}$$

Now, in isotropic material, the induced magnetization is along the same direction as the main field, and the z-component is dominant in the main magnetic field. Therefore, the eq (1.15) can be simplified as:

$$\Delta B(k) = -\frac{\mu_0(3cos^2\beta-1)}{3}\,M_z(k) \quad \text{..... (1.17)}$$

Now the relative induced field perturbation is:

$$\delta_B(k) = \frac{\Delta B_z(k)}{B_0} = (\frac{1}{3} - \frac{k_z^2}{k_x^2+k_y^2+k_z^2}).\chi(k) \quad \text{..... (1.18)}$$

This equation can be interpreted as a convolution of susceptibility distribution with a unit dipole response (d):

$$d = FT\,(\frac{1}{3} - \frac{k_z^2}{k_x^2+k_y^2+k_z^2}) = \frac{3cos^2\beta - 1}{4\pi\,|r|^3}_{\,r\neq 0} \quad \text{..... (1.19)}$$

This can be simplified as:

$$\delta_B(k) = D(k).\chi(k) \quad \text{..... (1.20)}$$

where $D(k) = \frac{1}{3} - \frac{k_z^2}{k_x^2+k_y^2+k_z^2}$

The inversion from local field map δ_B to its corresponding local susceptibility sources is an ill-posed problem because the property of the unit dipole kernel or convolution kernel is such that $D(k) = 0$ when $k_x^2 + k_y^2 = 2k_z^2$. As a result of this, there are two cones of zeros at the magic angle of 54.7^0 in the unit dipole kernel D(k). Hence the local susceptibility $\chi(\boldsymbol{k})$ cannot be directly solved by simple inversion $\frac{\delta_B}{D}$. It is equivalent to undersampling of $\chi(\boldsymbol{k})$, where information at the magic angle is lost. Several methods have been proposed to solve this problem including Calculation of Susceptibility through Multiple Orientation Sampling (COSMOS) [39],[65], Truncated k-Space Division (TKD) [26], Image space regularization etc. In COSMOS, the field created by the susceptibility distribution is sampled at multiple orientations with respect to the main magnetic field by rotating the object, and the susceptibility map is reconstructed such that it accounts for the signal void region in the dipole kernel. This is a stable and precise approach which allows quantitative mapping of arbitrary susceptibility distributions. Hence, COSMOS is often treated as a reference standard to compare other methods. However, acquiring data with multiple orientations is not realistic for patient studies. Total variation regularization [40] and Morphology enabled dipole inversion (MEDI) [41] have been used to perform QSM in this thesis.

1.6 Quantitative Susceptibility Weighted Imaging or True SWI (tSWI)

As described previously, SWI is a technique that offers means to study veins, lesions, hematoma and hence finds a wide range of clinical applications [4], [7], [42], [43]. However, this method

has some limitations because SWI is computed from filtered MR phase which along with susceptibility is also known to be dependent on shape and orientation of the structure of interest. Secondly, it has also been studied that the phase inside a vein perpendicular and parallel to the main magnetic field have opposite signs[44]. This leads to variable suppression effect with the phase mask computed from the filtered phase for SWI images; however, that doesn't happen for QSM. QSM also doesn't show any blooming effect around strong susceptibility objects as seen in SWI. Hence, a recent method called the true SWI (tSWI) has been introduced which utilizes the susceptibility maps to produce the mask instead of the filtered phase.

The threholded mask, W from the susceptibility map is computed as:

$$W=\begin{cases} 1 & \text{for } \chi \le \chi_1 \\ 1-\dfrac{\chi-\chi_1}{\chi_2-\chi_1} & \text{for } \chi_1 < \chi \le \chi_2 \\ 0 & \text{for } \chi > \chi_2 \end{cases} \quad \text{.....(1.21)}$$

where χ is the susceptibility value obtained from a susceptibility map, χ_1 is the lower threshold and χ_2 is the upper threshold of the range of susceptibility values. Finally, tSWI is generated by multiplying the magnitude image with the susceptibility weighted mask n times, similar to the usual SWI mask application:

$$tSWI = mag.W^n \quad \text{.....(1.22)}$$

In previous studies, this method was observed to provide a clearer depiction of vein at the magic angle (54.7^0 relative to main magnetic field) and also reduced blooming effect in microbleeds [45].

1.7 TOF Angiography

TOF MR angiography is an imaging method used to visualize blood vessels. The method distinguishes blood vessels from the surrounding static tissues by taking advantage of blood flow. The aim of this method is to allow blood signals to be refreshed over time by fresh inflow of blood while suppressing the background tissues to a lower signal level. For this to be possible, in the steady state equation, repetition time and the flip angle have to be chosen such that consistent fresh blood supply is maintained and the background is sufficiently low signal.

After the first RF pulse, the transverse magnetization is defined as:

$$M_{XY}(t = TE) = M_0\, exp(-\frac{TE}{T2^*})\, sin(\alpha) \quad \text{(1.23)}$$

where

TE: Echo time

T2*: Transverse relaxation of the sample for gradient echo sequences.

M_0: Longitudinal magnetization

M_{XY}: Transverse magnetization

α: Excitation flip angle

And longitudinal magnetization before the second RF pulse will be:

$$M_z(TR-) = M_0 + [M_z(0)cos(\alpha) - M_0]\, exp(-TR/T1) \quad \text{(1.24)}$$

Similarly, after n RF excitations, the equation can be described as:

$$M_z(n) = M_0 + [M_Z(n-1)cos(\alpha) - M_0]exp(-TR/T1) \quad \text{(1.25)}$$

$$M_{XY}(n) = Mz(n)exp(-\frac{TE}{T2^*})\, sin(\alpha) \quad \text{(1.26)}$$

T1: Longitudinal relaxation of the sample for gradient echo sequences.

M_0: Longitudinal magnetization

M_{XY}: Transverse magnetization

n: number of RF pulse experienced

Thus, the steady state is reached and is defined as

$$M_Z(steady) = M_0[1 - exp(-TR/T1)]/[1 - exp(-TR/T1)cos(\alpha)] \quad \text{.....(1.27)}$$

And the transverse magnetization at steady state is given as:

$$M_{XY}(TE \mid steady\ state) = \frac{M_0\left[1-\exp\left(-\frac{TR}{T1}\right)\right]\sin(\alpha)}{\left[1-\exp\left(-\frac{TR}{T1}\right)\cos(\alpha)\right]} exp(-\frac{TE}{T2^*}) \quad \text{.....(1.28)}$$

The steady state equation in eq (1.27) provides the signal of the tissues after several RF excitations. Now flowing blood enters the imaging field of view with fresh blood signal and is subjected to a lesser number of excitations than the stationary background tissue. As the fresh blood sees more and more RF excitation the signal intensity of the blood decreases as can be observed in eq (1.26). As n would increase the blood signal would decrease and the blood magnetization begins to saturate [46], [47]. This depends on the velocity of the blood in the slice selection direction, the thickness of the slab, TR and the flip angle. To ensure that fresh inflow of blood is maintained, overlapping slabs with small thicknesses are used in TOF imaging called multiple overlapping thin slab acquisition (MOTSA).

Along with that a special class of asymmetric pulses called ramped RF pulses [48] are used. As mentioned earlier, the blood tissue contrast will be highest when the fresh blood enters the slab and progressively decreases further into the slab as the blood becomes more saturated by repetitive RF-pulses. Now, since higher flip angle causes higher background suppression, in TOF an asymmetric ramped pulse is designed with flip angles that vary as a function of position such that the flip angles increase linearly along the direction of flow.

Moreover, TR and flip angle is also optimized to ensure adequate supply of fresh blood and sufficient suppression of background. If the TR is too short, the blood signal will not refresh fast

enough. While for a long TR, the background signal may fully recover leading to no contrast. Similarly, a moderate flip angle ensures some suppression of the background, but still a higher blood signal.

Another feature that TOF uses is applying a spatial saturation pulse for venous saturation. It is needed for separating arteries from the veins for better visualization of the arteries. To achieve this, a saturation pulse is applied above the imaging slab to suppress signal from intracerebral venous blood that flows in a downward direction. First a 90^0 RF pulse is applied and then the transverse magnetization is spoiled by crusher gradient lobes. This results in selective suppression of the longitudinal magnetization for the veins and allows improved arterial visualization.

The maximum intensity projection (MIP) of the magnitude images is used for arterial visualization. Figure 1.6 shows an example of the MIP of a TOF image with all these features.

Figure 1.6: MIP from a 3D-TOF scan of a healthy volunteer at 3T.

1.8 Intracerebral Hemorrhage (ICH)

Stroke is a leading cause of death and disability worldwide. Intracerebral hemorrhage (ICH) is the second most common type of stroke accounting for about 7% to 20% of all stroke admissions and is associated with early mortality in approximately 50% of these patients [49]–[51]. It

occurs when thin-walled arteries rupture and release blood into the brain tissue. As blood spills into the brain, the area that the arteries supply blood in, is deprived of oxygenated blood. Moreover, blood leaked into the brain parenchyma may cause toxic iron buildup that can lead to secondary inflammation and increased injury [52], [53]. An ICH can occur close to the surface or in deep areas of the brain. Sometimes deep hemorrhages expand into the ventricles causing blockage of the normal cerebrospinal (CSF) circulation resulting in enlargement of the ventricles (hydrocephalus). This can cause symptoms such as confusion, lethargy, and loss of consciousness [54], [55]. The different stages of hemorrhage have been described in detail in Table 1.1 [56],[8]. The nature of the accumulated hemoglobin, in hemorrhages, changes in form with time. Thus the susceptibility also changes from an initial diamagnetic state to various paramagnetic states as the lesion ages.

Table 1.1. Stages of Hemorrhage.

Stages	Time	Compartment	Hemoglobin	T1	T2
Hyperacute	<24 hrs	Intracellular	Oxyhemoglobin	Medium	Medium
Acute	1-3 days	Intracellular	Deoxyhemoglobin	Long	Short
Subacute-Early	3 days onwards	Intracellular	Methemoglobin	Short	Short
Subacute-Late	7 days onwards	Extracellular	Methemoglobin	Short	Long
Chronic-Center	14 days onwards	Extracellular	Hemichromes	Medium	Medium
Chronic-Rim	14 days onwards	Intracellular	Hemosiderin	Medium	Short

SWI and TOF-MRA methods are commonly used in the clinics for following ICH. SWI sequences used for stroke studies tend to be single echo GRE sequences with long TE (such as 20ms at 3T). Release of iron from hemoglobin plays a role in causing brain injury after hemorrhage [62]. QSM computed from a single echo SWI sequence offers a means to study these iron changes in the hematoma [57], [58],which can be useful for staging of hemorrhages [63] and has the potential to be useful in iron chelation therapy [60],[61].

However, standard QSM of ICH usually has some reconstruction limitations when using only one long TE. Hyperacute, acute and early subacute stages of ICH face a rapid T2* decay which may lead to low SNR regions and result in phase errors which in turn can cause severe artifacts in QSM. Hence, a separate QSM method such as the superposition method [59] is required to overcome this difficulty as described in the next section.

1.8.1 QSM for ICH

As described in the previous section, regions with strong susceptibility have rapid T2* decay, resulting in low signal in those regions. This can cause phase error which leads to artifacts in the QSM. To overcome this difficulty the superposition method was introduced [59]. In this method, QSM is reconstructed in two steps. First QSM is reconstructed on the entire brain and then in the next step, the high susceptibility region is masked out and QSM is conducted on the remaining tissue region as shown in Figure 1.7. Then the hemorrhagic region from the whole brain QSM is extracted and combined with the susceptibility map of the tissue region to produce the superposed QSM. In this thesis this method was used to compute QSM for hemorrhage. This method creates artifact free QSM for brains with hemorrhagic regions.

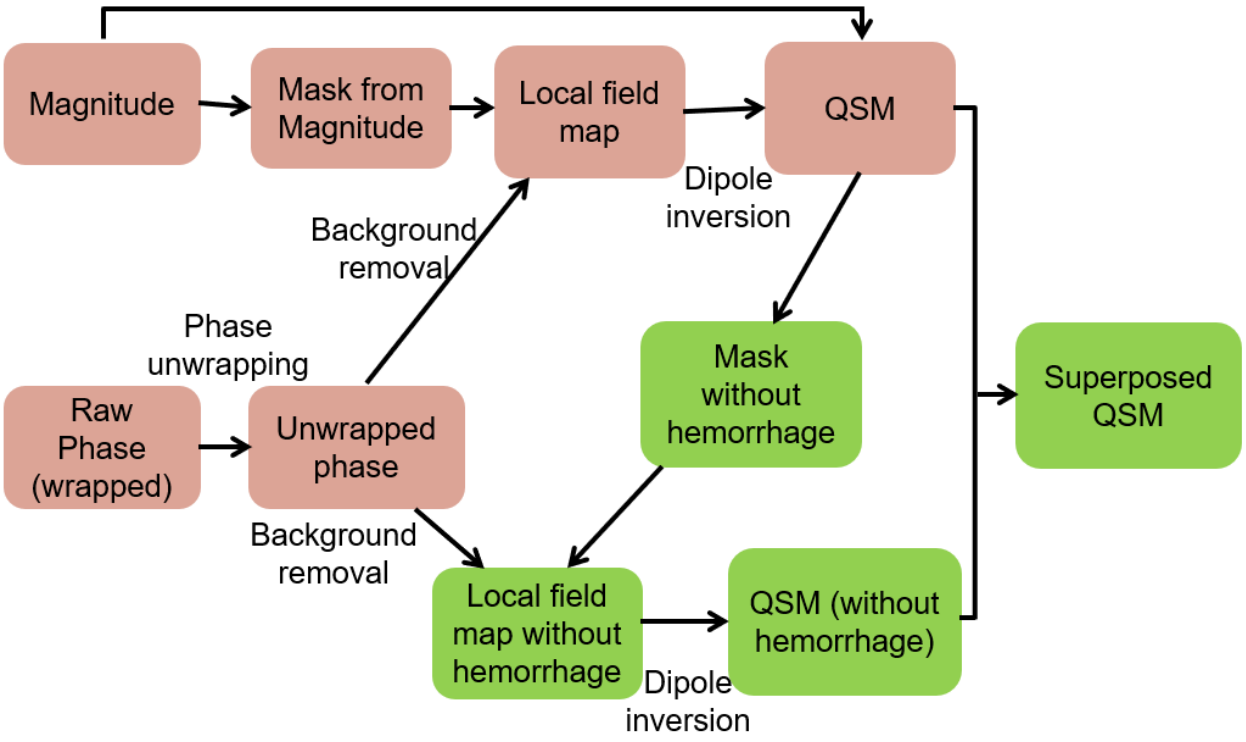

Figure 1.7: QSM reconstruction of ICH with superposition method.

1.9 Statistical Analysis

Statistical analysis [64] has been performed in this thesis to compare the datasets from various postprocessing methods. The statistical relationship, or association, between two continuous variables can be determined by using Pearson's correlation coefficient. It is based on the method of covariance and provides information about the magnitude of the association, or correlation, as well as the direction of the relationship. T-test is commonly used to compare the means of two independent groups. Similarly, a paired t-test can be used to determine whether the mean difference between two sets of observations is zero; thus, determining if there is a significant difference between the two. In a paired sample t-test, each subject or entity is measured twice i.e., once by each method, resulting in pairs of observations. Similarly, one-way analysis of variance (ANOVA)

compares the means of two or more groups in order to determine whether there is statistical evidence that the means are significantly different. If a significant ANOVA result is observed, post hoc tests can be used to further explore differences between multiple pairwise group means. These parametric tests are conducted based on the assumption that the data follows normality. The Q-Q plot and Shapiro Wilk tests can be performed to test the normality of a dataset. If a dataset doesn't follow a normality condition, non-parametric tests such as Mann-Whitney in place of t-test, Wilcoxon signed-rank test in place of paired t-test and Kruskal–Wallis test instead of one-way ANOVA can be used. Several of these tests have been chosen to compare the results in this thesis depending on the application.

1.10 Aim and Overview of Thesis

As described in the previous section, QSM is a versatile postprocessing method which helps to quantify iron content in tissues and pathological structures and hence has potential to be used in various clinical applications. This thesis discusses some of the challenges that come during application of QSM in a patient study and attempts to find solutions in order to make QSM more convenient for widespread applications. This thesis focuses on the application of QSM in stroke patients.

SWI is widely used to study hemorrhage patients and the SWI sequence can be used for QSM. The acquisition time of the SWI sequence is around 5 mins. However, EPI is a rapid sequence which can also be used to obtain images to compute QSM. Chapter 2 explores the application of the EPI sequence on hemorrhage patients and compares the susceptibility maps obtained from this sequence to the standard ones.

One of the major challenges of SWI sequence is the long acquisition time. Severely ill patients with ICH are unable to stay still or sometimes breath very heavily during the scans which can cause artifacts. Previous works have not studied the effect of these on QSM quantitatively. Hence, Chapter 3 investigates the effect of different movement and respiratory fluctuations on QSM quantitatively.

This thesis also looks at applying QSM to produce other quantitative images which may have potential for stroke studies. An example of such a method is tSWI which has the potential to overcome some of the limitations of SWI images. Previously tSWI has found its application in veins, tissues and microbleeds. In Chapter 4, the application of tSWI on hemorrhages has been studied and the parameters of tSWI computation has been investigated.

It is always preferred to get maximum information from a single acquisition. Hence, Chapter 5 introduces a multi-echo GRE sequence which can be used to acquire data in order to produce TOF, SWI, QSM and R2* map simultaneously while retaining key features of TOF-MRA.

References

[1] D. Nishimura, *Principles of Magnetic Resonance Imaging*. Lulu, 2010.

[2] E. M. Haacke, R. W. Brown, M. R. Thompson, and R. Venkatesan, *Magnetic Resonance Imaging: Physical Principles and Sequence Design*, 1st edition. New York: Wiley-Liss, 1999.

[3] Y. Wang, *Principles of Magnetic Resonance Imaging: Physics Concepts, Pulse Sequences, & Biomedical Applications*. CreateSpace Independent Publishing Platform, 2012.

[4] E. M. Haacke and J. R. Reichenbach, Eds., *Susceptibility Weighted Imaging in MRI: Basic Concepts and Clinical Applications*, 1st edition. Hoboken, N.J: Wiley-Blackwell, 2011.

[5] B. Xu, T. Liu, P. Spincemaille, M. Prince, and Y. Wang, "Flow Compensated Quantitative Susceptibility Mapping for Venous Oxygenation Imaging," *Magn. Reson. Med. Off. J. Soc. Magn. Reson. Med. Soc. Magn. Reson. Med.*, vol. 72, no. 2, pp. 438–445, Aug. 2014, doi: 10.1002/mrm.24937.

[6] P. Mansfield, "Real-time echo-planar imaging by NMR," *Br. Med. Bull.*, vol. 40, no. 2, pp. 187–190, Apr. 1984, doi: 10.1093/oxfordjournals.bmb.a071970.

[7] E. M. Haacke, S. Mittal, Z. Wu, J. Neelavalli, and Y.-C. N. Cheng, "Susceptibility-Weighted Imaging: Technical Aspects and Clinical Applications, Part 1," *Am. J. Neuroradiol.*, vol. 30, no. 1, pp. 19–30, Jan. 2009, doi: 10.3174/ajnr.A1400.

[8] H. Sun, "Quantitative Susceptibility Mapping in Human Brain: Methods Development and Applications," *ERA*, Fall 2015. https://era.library.ualberta.ca/items/9fca9424-2918-4b65-a4f6-07d30bf99e0c (accessed Mar. 23, 2022).

[9] E. G. Larsson, D. Erdogmus, R. Yan, J. C. Principe, and J. R. Fitzsimmons, "SNR-optimality of sum-of-squares reconstruction for phased-array magnetic resonance imaging," *J. Magn. Reson. San Diego Calif 1997*, vol. 163, no. 1, pp. 121–123, Jul. 2003, doi: 10.1016/s1090-7807(03)00132-0.

[10] K. E. Hammond *et al.*, "Development of a robust method for generating 7T multichannel phase images of the brain with application to normal volunteers and patients with neurological diseases," *NeuroImage*, vol. 39, no. 4, pp. 1682–1692, Feb. 2008, doi: 10.1016/j.neuroimage.2007.10.037.

[11] S. Robinson, G. Grabner, S. Witoszynskyj, and S. Trattnig, "Combining phase images from multi-channel RF coils using 3D phase offset maps derived from a dual-echo scan," *Magn. Reson. Med.*, vol. 65, no. 6, pp. 1638–1648, Jun. 2011, doi: 10.1002/mrm.22753.

[12] K. P. Pruessmann, M. Weiger, M. B. Scheidegger, and P. Boesiger, “SENSE: sensitivity encoding for fast MRI,” *Magn. Reson. Med.*, vol. 42, no. 5, pp. 952–962, Nov. 1999.

[13] P. B. Roemer, W. A. Edelstein, C. E. Hayes, S. P. Souza, and O. M. Mueller, “The NMR phased array,” *Magn. Reson. Med.*, vol. 16, no. 2, pp. 192–225, Nov. 1990, doi: 10.1002/mrm.1910160203.

[14] M. A. Bernstein, M. Grgic, T. J. Brosnan, and N. J. Pelc, “Reconstructions of phase contrast, phased array multicoil data,” *Magn. Reson. Med.*, vol. 32, no. 3, pp. 330–334, Sep. 1994, doi: 10.1002/mrm.1910320308.

[15] S. D. Robinson *et al.*, “Combining phase images from array coils using a short echo time reference scan (COMPOSER),” *Magn. Reson. Med.*, vol. 77, no. 1, pp. 318–327, 2017, doi: 10.1002/mrm.26093.

[16] B. Bilgic, J. Polimeni, L. Wald, and K. Setsompop, “Automated tissue phase and QSM estimation from multichannel data,” p. 22.

[17] M. Uecker *et al.*, “ESPIRiT—an eigenvalue approach to autocalibrating parallel MRI: Where SENSE meets GRAPPA,” *Magn. Reson. Med.*, vol. 71, no. 3, pp. 990–1001, 2014, doi: 10.1002/mrm.24751.

[18] D. O. Walsh, A. F. Gmitro, and M. W. Marcellin, “Adaptive reconstruction of phased array MR imagery,” *Magn. Reson. Med.*, vol. 43, no. 5, pp. 682–690, May 2000, doi: 10.1002/(sici)1522-2594(200005)43:5<682::aid-mrm10>3.0.co;2-g.

[19] S. M. Smith, “Fast robust automated brain extraction,” *Hum. Brain Mapp.*, vol. 17, no. 3, pp. 143–155, Nov. 2002, doi: 10.1002/hbm.10062.

[20] M. Jenkinson, “Fast, automated, N-dimensional phase-unwrapping algorithm,” *Magn. Reson. Med.*, vol. 49, no. 1, pp. 193–197, Jan. 2003, doi: 10.1002/mrm.10354.

[21] H. Bagher-Ebadian, Q. Jiang, and J. R. Ewing, "A modified Fourier-based phase unwrapping algorithm with an application to MRI venography," *J. Magn. Reson. Imaging JMRI*, vol. 27, no. 3, pp. 649–652, Mar. 2008, doi: 10.1002/jmri.21230.

[22] M. A. Schofield and Y. Zhu, "Fast phase unwrapping algorithm for interferometric applications," *Opt. Lett.*, vol. 28, no. 14, pp. 1194–1196, Jul. 2003, doi: 10.1364/OL.28.001194.

[23] H. S. Abdul-Rahman, M. A. Gdeisat, D. R. Burton, M. J. Lalor, F. Lilley, and C. J. Moore, "Fast and robust three-dimensional best path phase unwrapping algorithm," *Appl. Opt.*, vol. 46, no. 26, pp. 6623–6635, Sep. 2007, doi: 10.1364/AO.46.006623.

[24] S. Witoszynskyj, A. Rauscher, J. R. Reichenbach, and M. Barth, "Phase unwrapping of MR images using Phi UN--a fast and robust region growing algorithm," *Med. Image Anal.*, vol. 13, no. 2, pp. 257–268, Apr. 2009, doi: 10.1016/j.media.2008.10.004.

[25] W. Li, A. V. Avram, B. Wu, X. Xiao, and C. Liu, "Integrated Laplacian-based phase unwrapping and background phase removal for quantitative susceptibility mapping," *NMR Biomed.*, vol. 27, no. 2, pp. 219–227, Feb. 2014, doi: 10.1002/nbm.3056.

[26] S. Wharton, A. Schäfer, and R. Bowtell, "Susceptibility mapping in the human brain using threshold-based k-space division," *Magn. Reson. Med.*, vol. 63, no. 5, pp. 1292–1304, May 2010, doi: 10.1002/mrm.22334.

[27] T. Liu *et al.*, "A novel background field removal method for MRI using projection onto dipole fields (PDF)," *NMR Biomed.*, vol. 24, no. 9, pp. 1129–1136, Nov. 2011, doi: 10.1002/nbm.1670.

[28] L. Li and J. S. Leigh, "High-precision mapping of the magnetic field utilizing the harmonic function mean value property," *J. Magn. Reson. San Diego Calif 1997*, vol. 148, no. 2, pp.

442–448, Feb. 2001, doi: 10.1006/jmre.2000.2267.

[29] F. Schweser, A. Deistung, B. W. Lehr, and J. R. Reichenbach, "Quantitative imaging of intrinsic magnetic tissue properties using MRI signal phase: an approach to in vivo brain iron metabolism?," *NeuroImage*, vol. 54, no. 4, pp. 2789–2807, Feb. 2011, doi: 10.1016/j.neuroimage.2010.10.070.

[30] H. Sun and A. H. Wilman, "Background field removal using spherical mean value filtering and Tikhonov regularization," *Magn. Reson. Med.*, vol. 71, no. 3, pp. 1151–1157, 2014, doi: 10.1002/mrm.24765.

[31] D. Zhou, T. Liu, P. Spincemaille, and Y. Wang, "Background field removal by solving the Laplacian boundary value problem," *NMR Biomed.*, vol. 27, no. 3, pp. 312–319, Mar. 2014, doi: 10.1002/nbm.3064.

[32] R. Topfer, F. Schweser, A. Deistung, J. R. Reichenbach, and A. H. Wilman, "SHARP edges: recovering cortical phase contrast through harmonic extension," *Magn. Reson. Med.*, vol. 73, no. 2, pp. 851–856, Feb. 2015, doi: 10.1002/mrm.25148.

[33] P. S. Özbay, A. Deistung, X. Feng, D. Nanz, J. R. Reichenbach, and F. Schweser, "A comprehensive numerical analysis of background phase correction with V-SHARP," *NMR Biomed.*, vol. 30, no. 4, p. e3550, 2017, doi: 10.1002/nbm.3550.

[34] W. Li, B. Wu, and C. Liu, "Quantitative susceptibility mapping of human brain reflects spatial variation in tissue composition," *NeuroImage*, vol. 55, no. 4, pp. 1645–1656, Apr. 2011, doi: 10.1016/j.neuroimage.2010.11.088.

[35] J. Fang, L. Bao, X. Li, P. C. M. van Zijl, and Z. Chen, "Background field removal using a region adaptive kernel for quantitative susceptibility mapping of human brain," *J. Magn. Reson. San Diego Calif 1997*, vol. 281, pp. 130–140, Aug. 2017, doi:

10.1016/j.jmr.2017.05.004.

[36] B. Wu, W. Li, A. Guidon, and C. Liu, “Whole brain susceptibility mapping using compressed sensing,” *Magn. Reson. Med.*, vol. 67, no. 1, pp. 137–147, Jan. 2012, doi: 10.1002/mrm.23000.

[37] L. C. Evans, *An Introduction to Stochastic Differential Equations*. Providence, Rhode Island: American Mathematical Society, 2014.

[38] L. F. Shampine, “Numerical Recipes, The Art of Scientific Computing. By W. H. Press, B. P. Flannery, S. A. Teukolsky, and W. T. Vetterling,” *Am. Math. Mon.*, vol. 94, no. 9, pp. 889–893, Nov. 1987, doi: 10.1080/00029890.1987.12000737.

[39] B. Bilgic *et al.*, “Rapid multi-orientation quantitative susceptibility mapping,” *NeuroImage*, vol. 125, pp. 1131–1141, Jan. 2016, doi: 10.1016/j.neuroimage.2015.08.015.

[40] B. Bilgic, A. Pfefferbaum, T. Rohlfing, E. V. Sullivan, and E. Adalsteinsson, “MRI estimates of brain iron concentration in normal aging using quantitative susceptibility mapping,” *NeuroImage*, vol. 59, no. 3, pp. 2625–2635, Feb. 2012, doi: 10.1016/j.neuroimage.2011.08.077.

[41] T. Liu *et al.*, “Morphology enabled dipole inversion (MEDI) from a single-angle acquisition: comparison with COSMOS in human brain imaging,” *Magn. Reson. Med.*, vol. 66, no. 3, pp. 777–783, Sep. 2011, doi: 10.1002/mrm.22816.

[42] S. R. S. Barnes and E. M. Haacke, “Susceptibility-weighted imaging: clinical angiographic applications,” *Magn. Reson. Imaging Clin. N. Am.*, vol. 17, no. 1, pp. 47–61, Feb. 2009, doi: 10.1016/j.mric.2008.12.002.

[43] E. M. Haacke, Y. Xu, Y.-C. N. Cheng, and J. R. Reichenbach, “Susceptibility weighted imaging (SWI),” *Magn. Reson. Med.*, vol. 52, no. 3, pp. 612–618, Sep. 2004, doi:

10.1002/mrm.20198.

[44] Y. Xu and E. M. Haacke, “The role of voxel aspect ratio in determining apparent vascular phase behavior in susceptibility weighted imaging,” *Magn. Reson. Imaging*, vol. 24, no. 2, pp. 155–160, Feb. 2006, doi: 10.1016/j.mri.2005.10.030.

[45] S. Liu *et al.*, “Improved MR venography using quantitative susceptibility-weighted imaging,” *J. Magn. Reson. Imaging*, vol. 40, no. 3, pp. 698–708, 2014, doi: 10.1002/jmri.24413.

[46] J. H. Gao, S. K. Holland, and J. C. Gore, “Nuclear magnetic resonance signal from flowing nuclei in rapid imaging using gradient echoes,” *Med. Phys.*, vol. 15, no. 6, pp. 809–814, Dec. 1988, doi: 10.1118/1.596197.

[47] E. M. Haacke *et al.*, “Optimizing blood vessel contrast in fast three-dimensional MRI,” *Magn. Reson. Med.*, vol. 14, no. 2, pp. 202–221, May 1990, doi: 10.1002/mrm.1910140207.

[48] D. Atkinson, M. Brant-Zawadzki, G. Gillan, D. Purdy, and G. Laub, “Improved MR angiography: magnetization transfer suppression with variable flip angle excitation and increased resolution,” *Radiology*, vol. 190, no. 3, pp. 890–894, Mar. 1994, doi: 10.1148/radiology.190.3.8115646.

[49] A. Morotti *et al.*, “CT Angiography Spot Sign, Hematoma Expansion, and Outcome in Primary Pontine Intracerebral Hemorrhage,” *Neurocrit. Care*, vol. 25, no. 1, pp. 79–85, Aug. 2016, doi: 10.1007/s12028-016-0241-2.

[50] V. L. Feigin, C. M. M. Lawes, D. A. Bennett, S. L. Barker-Collo, and V. Parag, “Worldwide stroke incidence and early case fatality reported in 56 population-based studies: a systematic review,” *Lancet Neurol.*, vol. 8, no. 4, pp. 355–369, Apr. 2009, doi: 10.1016/S1474-4422(09)70025-0.

[51] C. J. van Asch, M. J. Luitse, G. J. Rinkel, I. van der Tweel, A. Algra, and C. J. Klijn,

"Incidence, case fatality, and functional outcome of intracerebral haemorrhage over time, according to age, sex, and ethnic origin: a systematic review and meta-analysis," *Lancet Neurol.*, vol. 9, no. 2, pp. 167–176, Feb. 2010, doi: 10.1016/S1474-4422(09)70340-0.

[52] R. F. Keep, Y. Hua, and G. Xi, "Intracerebral haemorrhage: mechanisms of injury and therapeutic targets," *Lancet Neurol.*, vol. 11, no. 8, pp. 720–731, Aug. 2012, doi: 10.1016/S1474-4422(12)70104-7.

[53] K. R. Wagner, F. R. Sharp, T. D. Ardizzone, A. Lu, and J. F. Clark, "Heme and iron metabolism: role in cerebral hemorrhage," *J. Cereb. Blood Flow Metab. Off. J. Int. Soc. Cereb. Blood Flow Metab.*, vol. 23, no. 6, pp. 629–652, Jun. 2003, doi: 10.1097/01.WCB.0000073905.87928.6D.

[54] J. C. Hemphill *et al.*, "Guidelines for the Management of Spontaneous Intracerebral Hemorrhage," *Stroke*, vol. 46, no. 7, pp. 2032–2060, Jul. 2015, doi: 10.1161/STR.0000000000000069.

[55] M. E. Fewel, B. G. Thompson, and J. T. Hoff, "Spontaneous intracerebral hemorrhage: a review," *Neurosurg. Focus*, vol. 15, no. 4, p. E1, Oct. 2003.

[56] W. G. Bradley, "MR appearance of hemorrhage in the brain," *Radiology*, vol. 189, no. 1, pp. 15–26, Oct. 1993, doi: 10.1148/radiology.189.1.8372185.

[57] T. Liu, K. Surapaneni, M. Lou, L. Cheng, P. Spincemaille, and Y. Wang, "Cerebral Microbleeds: Burden Assessment by Using Quantitative Susceptibility Mapping," *Radiology*, vol. 262, no. 1, pp. 269–278, Jan. 2012, doi: 10.1148/radiol.11110251.

[58] W. Chen *et al.*, "Intracranial calcifications and hemorrhages: characterization with quantitative susceptibility mapping," *Radiology*, vol. 270, no. 2, pp. 496–505, Feb. 2014, doi: 10.1148/radiol.13122640.

[59] H. Sun, M. Kate, L. C. Gioia, D. J. Emery, K. Butcher, and A. H. Wilman, "Quantitative susceptibility mapping using a superposed dipole inversion method: Application to intracranial hemorrhage," *Magn. Reson. Med.*, vol. 76, no. 3, pp. 781–791, Sep. 2016, doi: 10.1002/mrm.25919.

[60] M. Selim et al., "Deferoxamine mesylate in patients with intracerebral haemorrhage (i-DEF): a multicentre, randomised, placebo-controlled, double-blind phase 2 trial," *Lancet Neurol.*, vol. 18, no. 5, pp. 428–438, May 2019, doi: 10.1016/S1474-4422(19)30069-9.

[61] B. Behrouzi et al., "Action of iron chelator on intramyocardial hemorrhage and cardiac remodeling following acute myocardial infarction," *Basic Res. Cardiol*., vol. 115, no. 3, p. 24, Mar. 2020, doi: 10.1007/s00395-020-0782-6.

[62] J. Wu, Y. Hua, R. F. Keep, T. Nakamura, J. T. Hoff, and G. Xi, "Iron and Iron-Handling Proteins in the Brain After Intracerebral Hemorrhage," *Stroke*, vol. 34, no. 12, pp. 2964–2969, Dec. 2003, doi: 10.1161/01.STR.0000103140.52838.45.

[63] H. Sun *et al.*, "Quantitative Susceptibility Mapping for Following Intracranial Hemorrhage," *Radiology*, vol. 288, no. 3, pp. 830–839, Sep. 2018, doi: 10.1148/radiol.2018171918.

[64] D. S. Moore, W. I. Notz, and M. A. Fligner, The Basic Practice of Statistics. New York: W H Freeman & Co, 2015.

[65] T. Liu, P. Spincemaille, L. de Rochefort, B. Kressler, and Y. Wang, "Calculation of susceptibility through multiple orientation sampling (COSMOS): A method for conditioning the inverse problem from measured magnetic field map to susceptibility source image in MRI," Magn. Reson. Med., vol. 61, no. 1, pp. 196–204, 2009, doi: 10.1002/mrm.21828.

Chapter 2

Rapid Quantitative Susceptibility Mapping of Intracerebral Hemorrhage*

Abstract

Background: Quantitative susceptibility mapping (QSM) offers a means to track iron evolution in hemorrhage. However, standard QSM sequences have long acquisition times and are prone to motion artifacts in hemorrhagic patients. Purpose: To minimize motion artifact and acquisition time by performing rapid

*A version of this chapter has been published in JMRI: A. De, H. Sun, D. J. Emery, K. S. Butcher, and A. H. Wilman, "Rapid quantitative susceptibility mapping of intracerebral hemorrhage," J. Magn. Reson. Imaging JMRI, vol. 51, no. 3, pp. 712–718, Mar. 2020, doi: 10.1002/jmri.26850.

QSM in intracerebral hemorrhage (ICH) using single-shot Echo-planar imaging (EPI).

Population/Subjects: Forty-five hemorrhages were analyzed from 35 MRI exams obtained between February 2016 and March 2019 from 27 patients (14 male / 13 female, age: 71±12 years) with confirmed primary ICH.

Field Strength/Sequence: 3T; Susceptibility Weighted Imaging (SWI) with 4.54-minute acquisition and 2D single-shot gradient EPI with 0.45-minute acquisition.

Assessment: Susceptibility maps were constructed from both methods. Measurement of ICH area and mean magnetic susceptibility were made manually by three independent observers. Motion artifacts were quantified using the magnitude signal ratio of artifact-to-brain tissue to classify into three categories: mild or no artifact, moderate artifact, or severe artifact. The cutoff for each category was determined by four observers.

Statistical Tests: Pearson's correlation coefficient and paired t-test using $\alpha = 0.05$ were used to compare results. Inter and intraclass correlation was used to assess observer variability.

Results: Using 45 hemorrhages, the ICH regions measured on susceptibility maps obtained from EPI and SWI sequences had high correlation for area ($R^2 \geq 0.97$) and mean magnetic susceptibility ($R^2 \geq 0.93$) for all observers. The artifact-to-tissue ratio was significantly higher ($p < 0.01$) for SWI vs. EPI, and the standard deviation for the SWI method (SD = 0.05) was much larger than EPI (SD = 0.01). All observers' measurements showed high agreement.

Data Conclusion: Single-shot EPI-QSM enabled rapid measurement of ICH area and mean magnetic susceptibility, with reduced motion as compared with more standard SWI. EPI-QSM requires minimal additional acquisition time and could be incorporated into iron tracking studies in ICH.

2.1 Introduction

Intracerebral hemorrhage (ICH) is the second most common type of stroke [1]– [3]. Blood leakage into the brain parenchyma from ICH may cause toxic iron buildup that can lead to secondary inflammation and increased injury [4], [5]. In hemorrhage, the nature of the accumulated hemoglobin changes in form with time, from an initial diamagnetic state to various paramagnetic states as the lesion ages [6]. Quantitative susceptibility mapping (QSM) [7]– [9] offers a means to study these iron changes in hematoma. Susceptibility maps are produced from the phase images of a gradient echo (GRE) sequence. Previous ICH studies have proved QSM to be useful for distinguishing hemorrhage from calcification [10] and measuring hematoma volume [11]. Susceptibility studies have examined various stages of hematoma [12], including following individual subjects [13], and examining changes with therapy [14]. Susceptibility measures might also be useful for tracking the effects of potential iron chelating therapy in ICH patients [15]. Moreover, mean ICH susceptibility has shown better separation of various stages of hemorrhage as compared with conventional relaxation-weighted magnetic resonance imaging (MRI) [13]. These studies of ICH with QSM have used multi-echo GRE or single-echo susceptibility weighted imaging (SWI) [12]–[16], with the latter often included in clinical exams of suspected ICH. Both techniques usually require on the order of 5 minutes of acquisition time. However, clinical stroke studies are not always amenable to long acquisition times and may suffer from motion artifacts,

particularly in cases of severe disease, when patients may lack the capability to follow instructions. A rapid imaging alternative for QSM is single-shot 2D gradient Echo-planar imaging (EPI) [17] where whole brain susceptibility maps can be obtained in 7 seconds at 1.5T in healthy volunteers [18]. With each slice requiring less than 100 msec, typical brain motion is minimal in this short period. Other rapid QSM acquisitions have been tested on healthy subjects including 3D EPI [19], [20] and more complex variations of simultaneous excitation and acquisition techniques [21], but they are not generally available clinically and their motion sensitivity needs more study. In contrast, 2D single-shot EPI is a very common MRI sequence accessible on most systems. However, this method has not been attempted in the difficult environment of hemorrhage, where rapid signal decay may occur due to highly paramagnetic iron sources. Our purpose was to minimize motion artifact and acquisition time by performing rapid QSM in ICH using single-shot EPI and to compare its accuracy to QSM from SWI.

2.2 Materials and Methods

2.2.1 Patient Studies

Written consent was obtained from patients or substitute decision makers and the protocol was approved by the local Ethics Committee. Forty-five hemorrhages were analyzed from 35 exams obtained from 27 patients (14 male / 13 female, age: 71±12 years) with primary ICH. All patients received MRI between February 2016 and March 2019 using single-shot 2D EPI and standard SWI. MRI was acquired between day 2 and day 39 after symptom onset. Six patients underwent follow-up acquisitions. Due to rapid iron evolution of ICH during these intervals, the different timepoints were considered independently during analysis.

All patients were >18 years and had ICH confirmed by computed tomography (CT) within 24 hours of symptom onset in either lobar (8%) or deep (92%) location. The mean National Institutes of Health Stroke Scale (NIHSS) score of all patients was 9.3±7.0. The ICH was anticoagulant-associated in 15% of patients. 15% of patients had suffered a previous ICH and 11% a prior ischemic stroke. 58% of patients had a history of diagnosed hypertension. Other risk factors included ischemic heart disease (11%), dyslipidemia (42%), and diabetes (11%).

2.2.2 MRI Pulse Sequences

Standard SWI and a 2D single-shot EPI sequence were used at 3T (Siemens Prisma, Erlangen, Germany). Both sequences covered the whole cerebrum in an oblique axial plane. The SWI method used: 3D single gradient echo, first-order flow compensation, echo time (TE) 20 msec, repetition time (TR) 27 msec, voxel size 0.86 ×0.9 × 1.5 mm^3, 80 slices, in-plane field of view (FOV) = 200 × 220 mm^2, flip angle 15^0, acquisition time 4.54 mins and GRAPPA parallel imaging with acceleration factor of 2 along the primary phase-encoding direction. The 2D single-shot gradient EPI sequence used: TE 25 msec, voxel size 1.5 × 1.5 × 1.5 mm^3, 80 slices with interleaved slice ordering, in-plane FOV = 225 × 222 mm^2, flip angle 82^0, acquisition time 27 sec, Generalized Auto-calibrating Partial Parallel Acquisition (GRAPPA) parallel imaging with acceleration factor of 2, and 6/8th partial Fourier along the phase-encoding direction. The EPI acquisition used parallel imaging to maintain high resolution with appropriate TE and minimize blurring effects. However, parallel imaging required two additional TRs for a separate calibration scan and a forced dummy scan, which lengthened the acquisition time to three TRs (27 sec). A 64-channel phase-array head coil was used for signal reception.

2.2.3 Image Reconstruction

The phase information obtained from both sequences (SWI and EPI) was used to reconstruct independent susceptibility maps. To overcome unreliable phase measurements due to rapid signal loss within the ICH region, the superposed dipole inversion method was used [16], which was developed to cope with the low signal in hemorrhage regions and has been used to track hemorrhage evolution [13]. This method involves performing total-variation regularized dipole inversion [22] twice, with and then without the ICH dipole field and the results superimposed. QSM steps included extracting the brain using Brain Extraction Tool (BET) [23], unwrapping the phase using the 3D best path unwrapping technique [24], and then background removal was performed using LBV (Laplacian Boundary Value) [25] technique. Finally, the superposed dipole inversion was performed. The same reconstruction pathway was followed for both SWI and EPI data.

2.2.4 Image Analysis

ICH areas and susceptibility values were compared between the two methods. The susceptibility maps and magnitude images from EPI were registered with the SWI magnitude images using Statistical Parameter Mapping (SPM12) with rigid registration.

2D regions-of-interest (ROIs) were drawn manually by three MRI experts (A.D. with 3 years, H.S. with 9 years, and A.H.W. with 25 years of experience) on the same slices of the susceptibility maps obtained from SWI and EPI sequences. The ROIs were drawn independently for the two methods. The slices were selected by the first observer (A.D.) such that the ROI was drawn around

the largest hemorrhage area for each subject. To determine the degree of image artifacts, arising mainly from patient motion, an artifact-to-tissue ratio was defined as signal intensity from background air external to the brain divided by brain tissue. Rectangular ROIs were used in consistent locations, with area for air typically ~650 mm^2 and brain tissue from the mid posterior region typically ~800 mm^2. Based on this quantitative ratio, images from each sequence were classified as severe artifact if ratio > 0.076, moderate 0.05–0.076, and mild artifact or no artifacts less than 0.05. The threshold for each artifact-to-tissue ratio category was determined independently by the three MRI experts and a neuroradiologist (D.J.E. with 25 years' experience).

2.2.5 Statistical Analysis

Our statistical analysis was performed in Matlab R2016a (MathWorks, Natick, MA) and STATA/IC 15.1 (StataCorp, College Station, TX). The ICH areas and the susceptibility values between SWI and EPI sequences were compared using scatterplots and the computed Pearson's correlation coefficient. A Q-Q plot was used to check the normality of the data. A paired sample t-test was conducted to test if the areas and susceptibility values obtained with the two methods had any significant difference using $\alpha = 0.05$. Similar hypothesis testing was also conducted to compare the artifact-to-tissue ratios of the two methods. The intraclass and interclass variability were measured by calculating the intraclass correlation coefficients (ICC) using a two-way mixed model for absolute agreement. ICC measurements were used to assess the agreement in the area and susceptibility of the ICH and also the motion classification.

2.3 Results

2.3.1 ICH Area and Susceptibility Comparison

Examples of magnitude and susceptibility maps obtained from the SWI and EPI sequences in three ICH patients at different times from stroke onset are demonstrated in Figure 2.1. Magnitude images on EPI show pure T2* contrast without the strong T1-weighting that affects SWI. ICH regions appeared similar between methods.

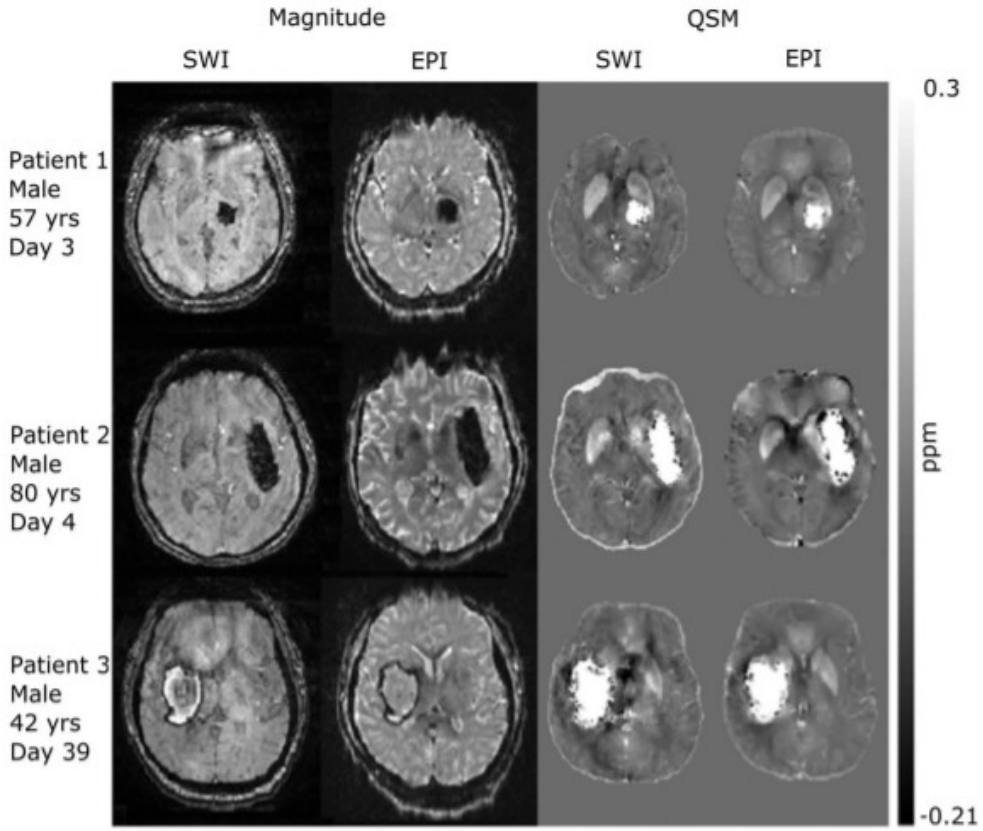

Figure 2.1: Comparison of magnitude images and susceptibility maps obtained from SWI (left) and 2D single-shot gradient EPI (right) for three patients imaged on different days after symptom onset. On QSM, the two methods have similar ICH depiction. On magnitude, SWI is both T2*- and T1-weighted, while EPI has pure T2* weighting due to the long TR.

Data comparing the ICH areas and susceptibilities between the two QSM methods are presented as boxplots (Figure 2.2) and as correlational analysis (Figure 2.3) using 45 hemorrhages from 34 of the 35 ICH exams. One exam was removed due to non-diagnostic images on SWI due to motion. From Figure 2.3, excellent correlation between SWI and EPI versions of QSM for ICH area (R^2 = 0.97, 0.99, 0.97, 0.98) and susceptibility (R^2 = 0.93, 0.93, 0.94, 0.94) were obtained for all the observations made by all the observers. No significant difference was observed between the area ($p = 0.341$) obtained from SWI and EPI sequences. However, EPI-QSM slightly underestimates the susceptibility values when considering all data ($p < 0.05$). Nevertheless, the susceptibility values showed no significant change ($p = 0.096$) between two methods for ICH susceptibility below 0.8 ppm, but EPI-QSM underestimates ($p < 0.05$) for higher susceptibility values, as evident from the fitted line in Figure 2.3.

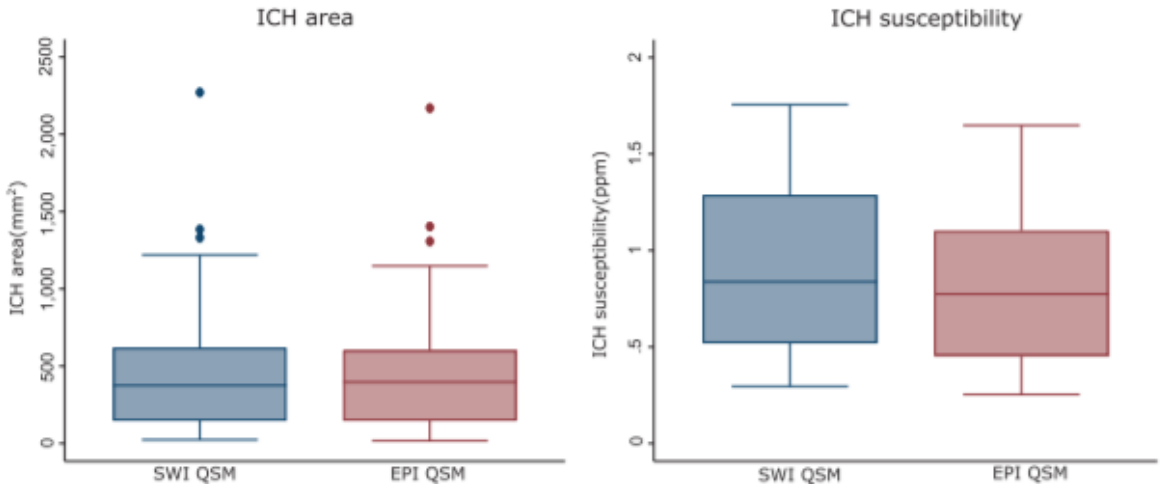

Figure 2.2: Boxplot of ICH area and susceptibility for the SWI and EPI-QSM methods. Forty-five hemorrhages were included from 34 exams. (Of the 35 exams available, one was excluded due to non-diagnostic images on SWI).

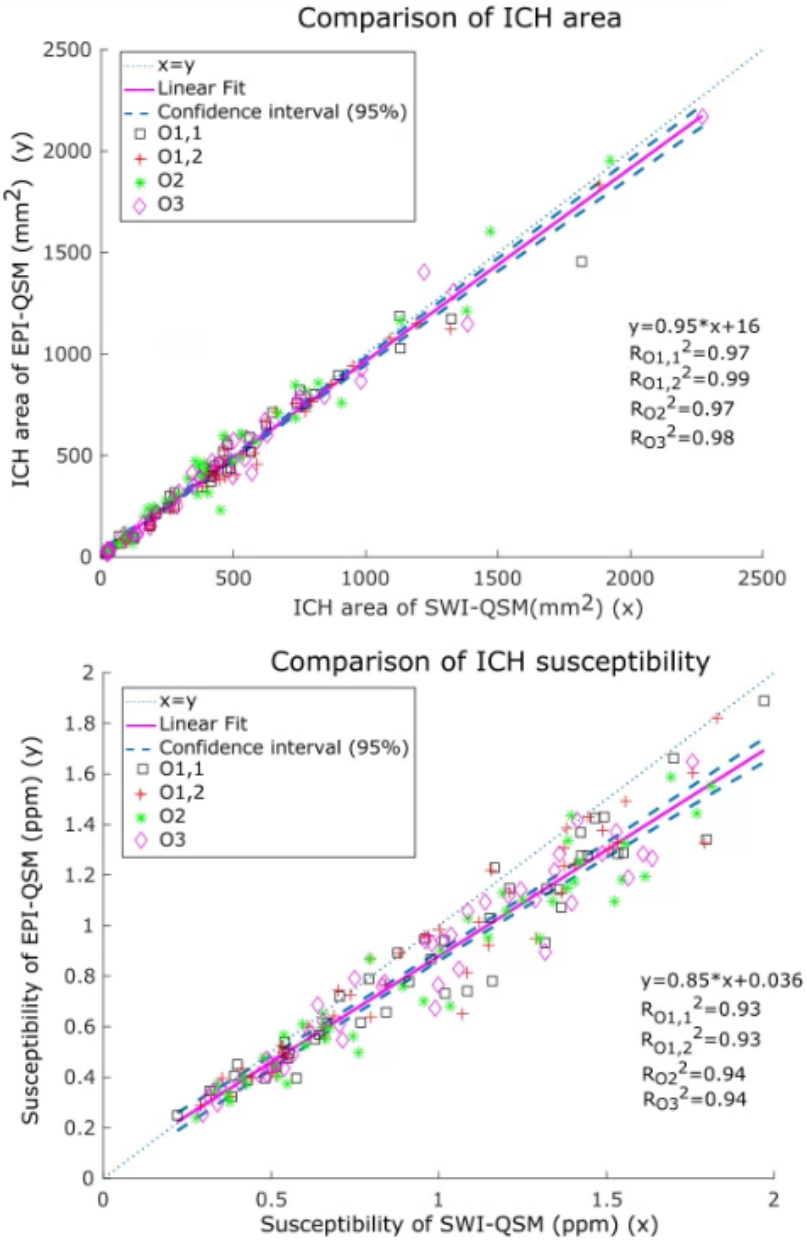

Figure 2.3: Correlation between ICH areas (top) and susceptibility (bottom) obtained from SWI-QSM (x-axis) and EPI-QSM (y-axis). Forty-five hemorrhages were included. Results are shown for three observers (O1, O2, O3), and repeat observations by the first observer (O1, 1 and O1, 2). High correlation was observed between area and susceptibility for both methods. The best-fitting line was calculated based on the average of values observed by all the observers and the correlation were calculated for individual measurements.

2.3.2 Motion Classification

Motion artifacts were observed frequently in SWI cases, for example, in Figure 2.4, where severe motion affects the SWI sequence, whereas the EPI sequence shows minimal effects.

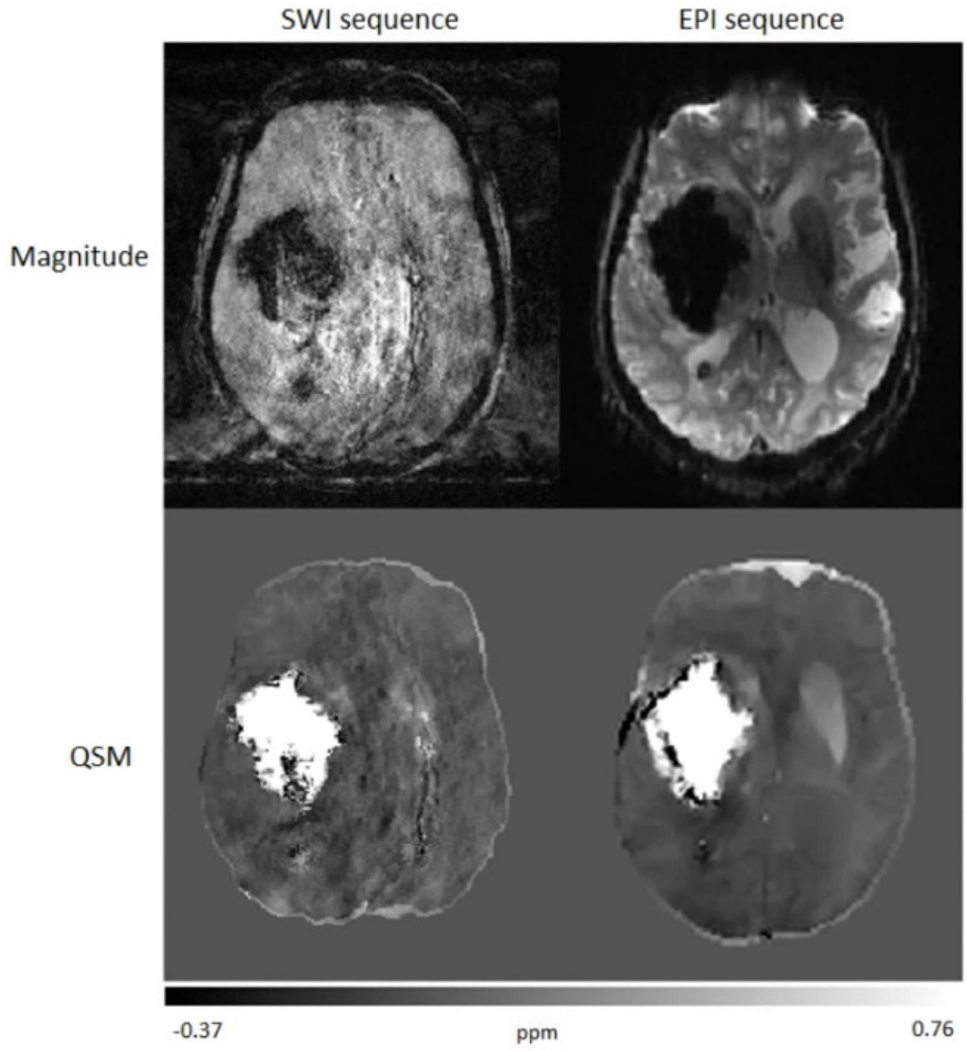

Figure 2.4: Magnitude and susceptibility maps obtained from SWI and EPI sequences for a patient (female, 81 years old) with hemorrhage imaged on day 2 after symptom onset. The SWI magnitude illustrates severe motion artifact (artifact-to-tissue ratio = 0.28), which resulted in distortion on QSM for SWI, whereas for EPI there was negligible motion (artifact-to-tissue ratio = 0.03).

Image examples of the artifact quantification ratio and classification obtained from magnitude images are demonstrated in Figure 2.5. The SWI sequence displayed higher artifacts, as evident from 11 exams with severe artifacts, 13 with moderate, and only 11 with mild or no artifacts. However, in the case of the EPI sequence, no exams had severe artifacts, only nine showed moderate artifacts, and 26 were mild or no artifacts. Further, the artifact-to-tissue ratio was significantly higher ($p < 0.01$) for SWI (mean = 0.07) vs. EPI (mean = 0.04), and the standard deviation for the SWI method (SD = 0.05) was much larger than EPI (SD = 0.01).

2.3.3 Inter- and Intra-observer Agreement

The ICCs corresponding to area and susceptibility measurement for intra- and interclass observers had high agreement, ranging from 0.881 to 0.996 (Table 2.1). The motion classification performed by the four observers also showed a high degree of agreement, with ICC ranging from 0.978 to 1.0 (complete agreement).

Table 2.1: Interclass Variability between three observers (O1, O2, O3) and Intraclass variability within observer 1 (O1) measurement for area and susceptibility.

Parameter	Interobserver variability			Intraobserver variability (ICC)
	O1 vs O2	O1 vs O3	O2 vs O3	
SWI area	0.981	0.980	0.980	0.997
EPI area	0.967	0.977	0.967	0.985
SWI susceptibility	0.920	0.974	0.919	0.996
EPI susceptibility	0.881	0.959	0.887	0.991

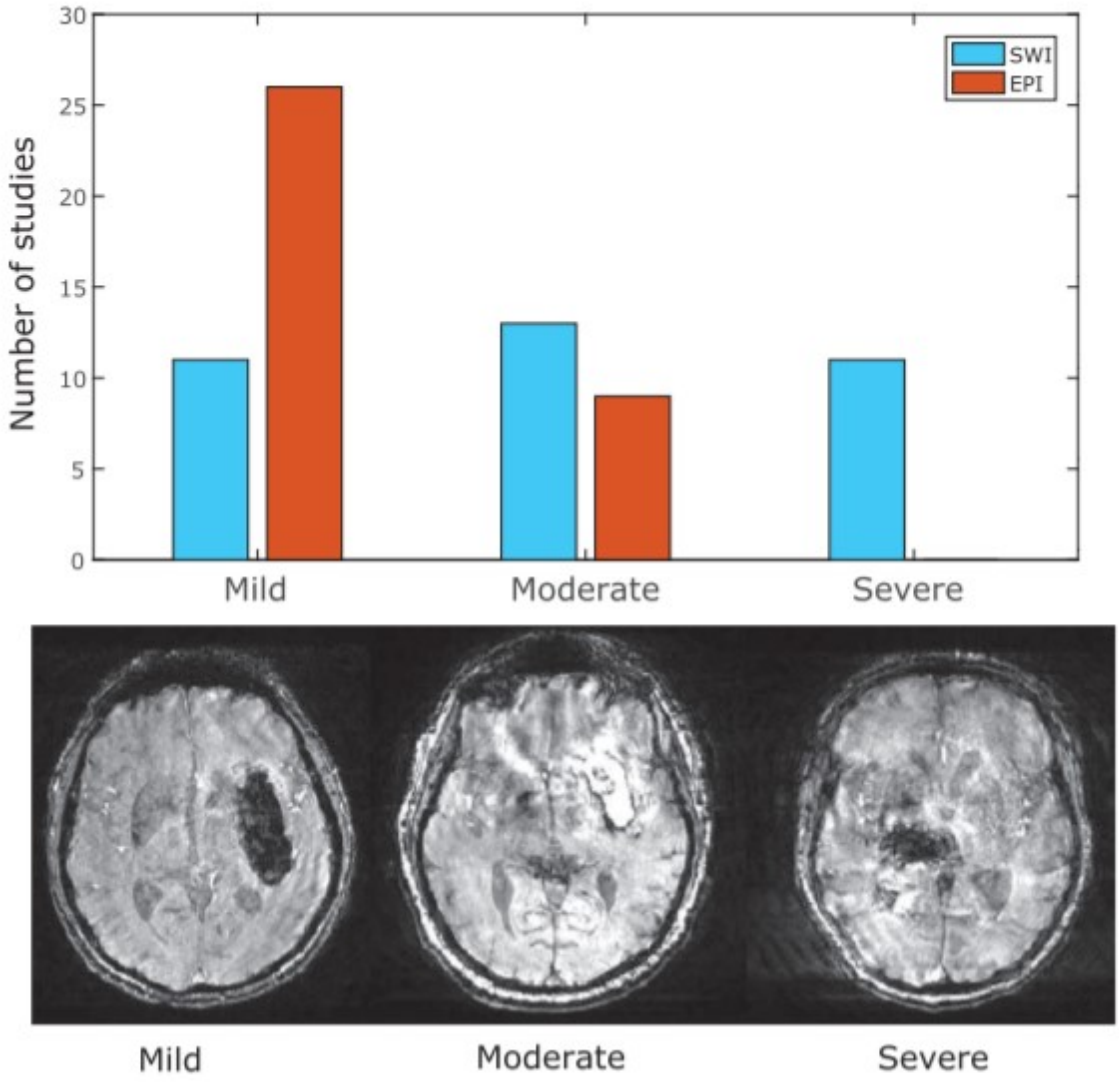

Figure 2.5: Artifact classification for all 35 scans (27 patients, 6 with multiple timepoints). The classification is based on quantitative measurement of the artifact-to-tissue ratio on magnitude images. Three examples are shown of SWI magnitude images with ratios: 0.042 (mild or no artifact), 0.071 (moderate artifact), and 0.157 (severe artifact).

2.4 Discussion

We demonstrated that single-shot 2D EPI, a fast and widely available method, enables rapid QSM of ICH for assessment of hemorrhage area and susceptibility. The standard sequences used for QSM generally take several minutes, which in ICH subjects often lead to patient motion artifacts in the resultant susceptibility maps. Here, we demonstrated that rapid QSM using single-shot EPI enabled a 10 times faster acquisition than SWI and substantially reduced motion artifacts. Hemorrhage area measurements were similar between the two methods and highly correlated. Susceptibility measures were also highly correlated between the methods; however, EPI-QSM underestimated the susceptibility when considering all data. Susceptibility values less than 0.8 ppm showed good agreement.

The reason for underestimation for the highest susceptibility may relate to the reduced spatial resolution of EPI combined with rapid signal loss in these cases. The highest ICH susceptibility values typically occur in the acute and early subacute phase [6], [13] and produce rapid signal decay, yielding extremely low magnitude on SWI or EPI. The superposed dipole inversion method can cope with the low signal areas, but the phase unwrapping process may be affected. For these cases, the lower resolution of EPI, combined with the magnitude signal loss, may lead to less precision in phase unwrapping along the rim of the ICH, leading to dark rim artifacts that produce a net underestimation of the ICH susceptibility value [18], [26], [27]. At the current resolution, EPI-QSM may also cause slight underestimation of susceptibility in small hemorrhages (<100 mm^2) due to partial volume effects.

The extended EPI readout can lead to distortions, particularly around air–tissue interfaces. Most of the hemorrhages we studied were central in the brain and none were near the anterior border of

the brain, which has a greater degree of distortion on EPI. The distortion and resolution limitations could be overcome with multi shot EPI, but this would limit the hallmark feature of single-shot EPI, which is superior suppression of motion artifact through extremely rapid imaging. This robustness to motion was found to be a critical factor for hemorrhage patients, who often had substantial motion artifacts on SWI. Thus, despite the inherent limitations of EPI, EPI-QSM was generally preferable to SWI-QSM in this patient group when motion was present. In patients receiving SWI for QSM, EPI-QSM could be a useful add-on when motion is suspected.

Study limitations included the lack of flexibility in the available product EPI sequence, which required a 27-second total acquisition. While the total EPI acquisition time remained 10-fold less than SWI, previous implementations of EPI-QSM have used less than 10 seconds of total acquisition time, by dispensing with the dummy scan and utilizing inline parallel imaging, albeit at 1.5T [18], which allows longer TE. Both SWI and EPI methods for QSM used a single moderate TE; however, multi-echo acquisitions that include additional shorter TEs could have led to more effective phase unwrapping, which could improve susceptibility maps. Nevertheless, single-echo SWI is the current clinical standard used in stroke studies and multi-echo EPI sequences would have required additional acquisition time. Rapid T2* decay in acute hemorrhages causes severe signal loss resulting in low SNR which can affect the standard phase unwrapping in some cases. Improvement can be made in unwrapping step as has been briefly explored in appendix A. A further limitation is the SWI-QSM used, as the reference standard was affected by motion artifacts that may have limited its accuracy.

In conclusion, in ICH subjects motion artifacts were common in SWI acquisitions but not in single-shot EPI. Single-shot EPI-QSM enabled rapid measurement of ICH area and susceptibility, with reduced motion artifacts compared with susceptibility maps obtained from standard SWI. EPI-

QSM requires minimal additional acquisition time and could be incorporated into iron tracking studies in ICH.

2.5 Acknowledgments

Contract grant sponsor: Canadian Institutes of Health Research.

Partial salary support for A.D. was provided by a Mitacs scholarship.

References

[1] A. Morotti *et al.*, "CT Angiography Spot Sign, Hematoma Expansion, and Outcome in Primary Pontine Intracerebral Hemorrhage," *Neurocrit. Care*, vol. 25, no. 1, pp. 79–85, Aug. 2016, doi: 10.1007/s12028-016-0241-2.

[2] V. L. Feigin, C. M. M. Lawes, D. A. Bennett, S. L. Barker-Collo, and V. Parag, "Worldwide stroke incidence and early case fatality reported in 56 population-based studies: a systematic review," *Lancet Neurol.*, vol. 8, no. 4, pp. 355–369, Apr. 2009, doi: 10.1016/S1474-4422(09)70025-0.

[3] C. J. van Asch, M. J. Luitse, G. J. Rinkel, I. van der Tweel, A. Algra, and C. J. Klijn, "Incidence, case fatality, and functional outcome of intracerebral haemorrhage over time, according to age, sex, and ethnic origin: a systematic review and meta-analysis," *Lancet Neurol.*, vol. 9, no. 2, pp. 167–176, Feb. 2010, doi: 10.1016/S1474-4422(09)70340-0.

[4] R. F. Keep, Y. Hua, and G. Xi, "Intracerebral haemorrhage: mechanisms of injury and therapeutic targets," *Lancet Neurol.*, vol. 11, no. 8, pp. 720–731, Aug. 2012, doi: 10.1016/S1474-4422(12)70104-7.

[5] K. R. Wagner, F. R. Sharp, T. D. Ardizzone, A. Lu, and J. F. Clark, "Heme and iron

metabolism: role in cerebral hemorrhage," *J. Cereb. Blood Flow Metab. Off. J. Int. Soc. Cereb. Blood Flow Metab.*, vol. 23, no. 6, pp. 629–652, Jun. 2003, doi: 10.1097/01.WCB.0000073905.87928.6D.

[6] W. G. Bradley, "MR appearance of hemorrhage in the brain," *Radiology*, vol. 189, no. 1, pp. 15–26, Oct. 1993, doi: 10.1148/radiology.189.1.8372185.

[7] T. Liu, P. Spincemaille, L. de Rochefort, B. Kressler, and Y. Wang, "Calculation of susceptibility through multiple orientation sampling (COSMOS): A method for conditioning the inverse problem from measured magnetic field map to susceptibility source image in MRI," *Magn. Reson. Med.*, vol. 61, no. 1, pp. 196–204, 2009, doi: 10.1002/mrm.21828.

[8] L. de Rochefort *et al.*, "Quantitative susceptibility map reconstruction from MR phase data using bayesian regularization: validation and application to brain imaging," *Magn. Reson. Med.*, vol. 63, no. 1, pp. 194–206, Jan. 2010, doi: 10.1002/mrm.22187.

[9] K. Shmueli, J. A. de Zwart, P. van Gelderen, T.-Q. Li, S. J. Dodd, and J. H. Duyn, "Magnetic susceptibility mapping of brain tissue in vivo using MRI phase data," *Magn. Reson. Med.*, vol. 62, no. 6, pp. 1510–1522, Dec. 2009, doi: 10.1002/mrm.22135.

[10] W. Chen *et al.*, "Intracranial calcifications and hemorrhages: characterization with quantitative susceptibility mapping," *Radiology*, vol. 270, no. 2, pp. 496–505, Feb. 2014, doi: 10.1148/radiol.13122640.

[11] S. Wang, M. Lou, T. Liu, D. Cui, X. Chen, and Y. Wang, "Hematoma volume measurement in gradient echo MRI using quantitative susceptibility mapping," *Stroke*, vol. 44, no. 8, pp. 2315–2317, Aug. 2013, doi: 10.1161/STROKEAHA.113.001638.

[12] S. Chang *et al.*, "Quantitative Susceptibility Mapping of Intracerebral Hemorrhages at Various Stages," *J. Magn. Reson. Imaging JMRI*, vol. 44, no. 2, pp. 420–425, Aug. 2016,

doi: 10.1002/jmri.25143.

[13] H. Sun *et al.*, "Quantitative Susceptibility Mapping for Following Intracranial Hemorrhage," *Radiology*, vol. 288, no. 3, pp. 830–839, Sep. 2018, doi: 10.1148/radiol.2018171918.

[14] Y. Zhang *et al.*, "Quantitative Susceptibility Mapping (QSM) As a Means to Monitor Cerebral Hematoma Treatment," *J. Magn. Reson. Imaging JMRI*, vol. 48, no. 4, pp. 907–915, Oct. 2018, doi: 10.1002/jmri.25957.

[15] S. D. Yeatts, Y. Y. Palesch, C. S. Moy, and M. Selim, "High dose deferoxamine in intracerebral hemorrhage (HI-DEF) trial: rationale, design, and methods," *Neurocrit. Care*, vol. 19, no. 2, pp. 257–266, Oct. 2013, doi: 10.1007/s12028-013-9861-y.

[16] H. Sun, M. Kate, L. C. Gioia, D. J. Emery, K. Butcher, and A. H. Wilman, "Quantitative susceptibility mapping using a superposed dipole inversion method: Application to intracranial hemorrhage," *Magn. Reson. Med.*, vol. 76, no. 3, pp. 781–791, Sep. 2016, doi: 10.1002/mrm.25919.

[17] P. Mansfield, "Real-time echo-planar imaging by NMR," *Br. Med. Bull.*, vol. 40, no. 2, pp. 187–190, Apr. 1984, doi: 10.1093/oxfordjournals.bmb.a071970.

[18] H. Sun and A. H. Wilman, "Quantitative susceptibility mapping using single-shot echo-planar imaging," *Magn. Reson. Med.*, vol. 73, no. 5, pp. 1932–1938, May 2015, doi: 10.1002/mrm.25316.

[19] C. Langkammer *et al.*, "Fast quantitative susceptibility mapping using 3D EPI and total generalized variation," *NeuroImage*, vol. 111, pp. 622–630, May 2015, doi: 10.1016/j.neuroimage.2015.02.041.

[20] I. Chatnuntawech *et al.*, "Single-step quantitative susceptibility mapping with variational penalties," *NMR Biomed.*, vol. 30, no. 4, Apr. 2017, doi: 10.1002/nbm.3570.

[21] B. Bilgic, H. Ye, L. L. Wald, and K. Setsompop, “Simultaneous Time Interleaved MultiSlice (STIMS) for Rapid Susceptibility Weighted Acquisition,” *NeuroImage*, vol. 155, pp. 577–586, Jul. 2017, doi: 10.1016/j.neuroimage.2017.04.036.

[22] B. Bilgic, A. Pfefferbaum, T. Rohlfing, E. V. Sullivan, and E. Adalsteinsson, “MRI estimates of brain iron concentration in normal aging using quantitative susceptibility mapping,” *NeuroImage*, vol. 59, no. 3, pp. 2625–2635, Feb. 2012, doi: 10.1016/j.neuroimage.2011.08.077.

[23] S. M. Smith, “Fast robust automated brain extraction,” *Hum. Brain Mapp.*, vol. 17, no. 3, pp. 143–155, Nov. 2002, doi: 10.1002/hbm.10062.

[24] H. S. Abdul-Rahman, M. A. Gdeisat, D. R. Burton, M. J. Lalor, F. Lilley, and C. J. Moore, “Fast and robust three-dimensional best path phase unwrapping algorithm,” *Appl. Opt.*, vol. 46, no. 26, pp. 6623–6635, Sep. 2007, doi: 10.1364/ao.46.006623.

[25] D. Zhou, T. Liu, P. Spincemaille, and Y. Wang, “Background field removal by solving the Laplacian boundary value problem,” *NMR Biomed.*, vol. 27, no. 3, pp. 312–319, Mar. 2014, doi: 10.1002/nbm.3064.

[26] M. J. Cronin, N. Wang, K. S. Decker, H. Wei, W.-Z. Zhu, and C. Liu, “Exploring the origins of echo-time-dependent quantitative susceptibility mapping (QSM) measurements in healthy tissue and cerebral microbleeds,” *NeuroImage*, vol. 149, pp. 98–113, Apr. 2017, doi: 10.1016/j.neuroimage.2017.01.053.

[27] D. Zhou, J. Cho, J. Zhang, P. Spincemaille, and Y. Wang, “Susceptibility underestimation in a high-susceptibility phantom: Dependence on imaging resolution, magnitude contrast, and other parameters,” *Magn. Reson. Med.*, vol. 78, no. 3, pp. 1080–1086, Sep. 2017, doi: 10.1002/mrm.26475.

Chapter 3

Effects of movement and respiratory fluctuations on susceptibility values of iron-rich deep grey matter at 3T*

Abstract

Purpose: To quantitatively investigate the effects of motion and respiratory fluctuations on QSM in the brain using simulation, volunteer, and patient scans.

Method: To study the effect of movement on QSM at 3T, 8 subjects (2 volunteers, 4 ischemic stroke patients and 2 hemorrhagic patients) were scanned with a 3D single-echo GRE sequence and simulations were performed to incorporate various

*A part of this chapter was presented in ISMRM: A. De, H. Sun, A. Elkady, P. Seres and A. H. Wilman, "Effects of Motion in Quantitative Susceptibility Mapping of Brain", ISMRM, Paris, France, 2018

motion patterns into the data. QSM was computed and compared between the original and simulated data.

In order to observe the effect of respiration, breath-hold experiments compared the susceptibility values between inhale, exhale and free-breathing states for 5 volunteers. In addition, QSM under dynamic breathing experiments was performed with navigator echo recording in another 5 volunteers. QSM computed before and after correction were compared.

Result: The incorporation of simulated movement showed statistically significant differences ($p<0.05$) in susceptibility values and magnitude signal in many brain regions. This movement caused visible artifacts in both magnitude and QSM. However, in most cases, variations on QSM were larger than on magnitude images and had more artifacts. Different breath-hold positions showed no statistically significant difference in susceptibility values and 3D navigator correction in free breathing experiments had differences of 2.2 to 12.2 ppb between susceptibility values before and after correction.

Conclusion: In general, QSM showed greater sensitivity to motion than magnitude. While respiratory fluctuations did not cause severe artifact, differences in susceptibility values in iron-rich deep grey matter were observed and correcting for respiratory fluctuations can be beneficial for susceptibility measurements.

3.1 Introduction

Quantitative Susceptibility Mapping (QSM) is an emerging post processing technique with many potential clinical applications. QSM can provide quantitative information about brain iron content and distinguish paramagnetic iron from diamagnetic myelin and calcification [1], [2]. Hence QSM finds its application in several neurological diseases such as stroke (ischemic and hemorrhagic) [3]–[8], Alzheimer's disease [9]–[11], multiple sclerosis [12]–[14] and Parkinson's disease [15]–[17].

Gradient echo (GRE) sequences with single or multiple echoes are used for QSM with T2* weighting to create sensitivity to susceptibility differences. Typical QSM acquisitions use whole brain 3D volumes and high resolution leading to scan times ~5 minutes in many cases. The relatively long scan time, coupled with long T2* decay makes the method vulnerable to patient motion and magnetic field variations due to physiological fluctuations like respiratory motion. All these variations can lead to ghosting and blurring and cause signal variations resulting in degradation of the image quality of the magnitude and phase images [18]–[21]. QSM is reconstructed utilizing these magnitude and phase images and hence the motion artifacts are translated to QSM, potentially leading to artifactual susceptibility values and image degradation. However, motion effects on susceptibility values have not been well studied.

The general area of motion tracking and correction has been widely studied, particularly for magnitude images [18], [36]. For example, respiratory fluctuations can be tracked either by MR navigator echoes [22]–[24], [37] or using external devices like NMR field probes, respiratory bellows or optical systems [25], [26], [38]. However, studies assessing motion on QSM and the effects on the susceptibility values have been minimal. Previous papers have demonstrated

distortion on QSM due to motion in studies with patient data from stroke [8] and Alzheimer's disease [20]; however, effects of motion on susceptibility values have not been quantified. A previous study has discussed the effect of prospective motion correction on QSM qualitative and quantitatively, however, it required implementation of external hardware [21]. In addition, many studies on respiratory artifact have been at 7 T [22], [25], [26] where effects are larger than more standard fields like 3T studied here.

The purpose of this work is to understand the effects of motion from both external movement and internal respiratory motion on brain QSM at 3T, and to quantify the susceptibility values. . The effect of movement was studied via volunteer scans and simulation; and the effect of respiratory fluctuations was studied using breath-hold experiments and using a MR navigator incorporated into the QSM sequence.

3.2 Methods

3.2.1 Acquisition

All data were acquired at 3T (Prisma, Siemens Healthcare, Erlangen, Germany). To study movement effects, magnitude and phase images were obtained from single echo 3D GRE sequences with the following parameters: echo time (TE) = 20ms, repetition time (TR) = 27ms, flip angle = 15^0, , in-plane field of view (FOV) = 200 x 220 mm^2, first-order flow compensation in all directions and GRAPPA parallel imaging with acceleration factor of 2 along the primary phase-encoding direction. Two versions were used with either 80 slices, resolution = 0.9 x 0.9 x 1.5mm^3, acquisition time 4.54 mins or 72 slices, 0.7x0.7x2.0 mm^3 and 3.5 mins.

To study effects of respiration, breath-hold experiments were conducted with a single-shot 2D Echo-planar Imaging (EPI) sequence with parameters: TE = 25ms, resolution = 1.5 x 1.5 x 1.5mm^3, in-plane field of view (FOV) = 225 x 222mm^2, 70 slices, flip angle = 82^0, acquisition time time=21s, GRAPPA parallel imaging with acceleration factor of 2, and 6/8th partial Fourier along the phase-encoding direction. Data was also collected under free breathing using a 3D multi-echo gradient echo (MEGE) sequence with the following parameters: TR = 42 ms, number of echoes = 7, first TE = 3.82ms, echo spacing = 5.49 ms, voxel size = 0.93 x 0.93 x 2 mm^3, in-plane field of view (FOV) = 217.5 x 240mm^2, 60 slices, flip angle = 17^0, acquisition time = 5.30 mins. The sequence was modified to make the 7th echo a navigator echo by removing its phase encode gradients.

3.2.2 Subjects

This study was approved by the institutional ethics board and all subjects gave informed consent. Motion patterns were simulated and applied to uncorrupted data in 8 subjects (2 volunteers, 4 ischemic stroke and 2 hemorrhagic stroke patients). Prospective motion experiments were performed to collect data from a volunteer while staying still, making rhythmic head movement and moving head sharply during the scan. In order to understand the effect of respiration, 5 volunteers were scanned with the EPI sequence while breathing normally or holding their breath after inhale and exhale. Five volunteers were also scanned with the 3D MEGE navigator sequence under normal breathing.

3.2.3 Simulation

All simulations were performed in MATLAB R2019a (Mathworks, Natick, MA). To evaluate motion patterns, the complex image was transformed back to k-space and simulated motion was used to corrupt the images. Patient motion [8,18,20] can be associated with ringing artifacts, blurring or distortion in the frontal part of the brain often caused due to rhythmic movement, sudden change of head position during scans or head movement from deep breathing. Simplified forms of two of these motion patterns were simulated. First, where the head was displaced by 10 voxels in every 14s implying rhythmic motion. The second simulation caused a sharp displacement of 10 voxels resulting in change of head location in the last one-third of the scan corresponding to the concept of sudden movement during scanning. QSM was then reconstructed from the distorted magnitude and phase images.

3.2.4 Reconstruction

All reconstruction steps were performed in MATLAB R2019a. The magnitude and phase images obtained from the scanner were used to construct susceptibility maps. QSM computation steps included forming a binary volume mask of brain tissues with Brain Extraction Tool (BET) [27], phase unwrapping with phase region expanding labeller for unwrapping discrete estimates (PRELUDE) [28] and background removal with Regularization Enabled Sophisticated Harmonic Artifact Reduction for Phase (RESHARP) [29] followed by total variation dipole inversion [30]. QSM from hemorrhages used the superposition method [7] with computational steps as described in detail in [8].

For the navigator sequence, data is collected in k-space and Fourier transformed to obtain magnitude and phase images in the image domain and coil combination was performed using POEM multi-channel coil combination [31].

For the navigator echo, the k-space data was Fourier transformed in readout direction to produce the projection [32]–[34] and any existing phase wraps were unwrapped. For each spatial point (x) and phase encoding step, the phase difference ($\Delta\emptyset$) was calculated as the difference between the phase of the N^{th} and the first step. This phase difference for each individual coil was then used to compensate for the respiratory fluctuations in the complex images in each of the image echoes that preceded the navigator echo in the MEGE train as [32]: $S_{corr}(x,TE) = S(x,TE).e^{-i\frac{\Delta\emptyset}{TE_{NAV}}TE}$; where $S_{corr}(x,TE)$ and $S(x,TE)$ are the signals in k-space after and before correction, respectively, TE is echo time, TE_{NAV} is the echo time of navigator echo. Finally, coil combination was performed on these corrected images and then the magnitude and phase images were used to compute QSM.

3.2.5 Image Analysis

2D regions-of-interest (ROIs) measurements on magnitude and QSM were made in iron rich brain structures including dentate nucleus, caudate, putamen, globus pallidus and neighboring white matter in the internal capsule. ROIs were drawn manually on the susceptibility maps using ImageJ then transferred to magnitude images. Statistical analysis was conducted in MATLAB R2019a and R 4.1.1. Wilcoxon signed-rank test was used to compare magnitude and susceptibility values with and without motion-corruption. It was also used to compare susceptibility values before and after

correction for respiratory fluctuations using the navigator sequence. Kruskal-Wallis test was used to compare the difference in susceptibility values between inhale, exhale and free breathing states.

3.3 Results

Figure 3.1 shows the effect of motion in a volunteer performing different movements during the scan. Figure 3.2 shows the effect of incorporating simulated movements in images. Artifacts and distortions were observed in all of the magnitude, phase, local field and QSM images for both types of motion. Table 3.1 shows the percentage difference for magnitude and susceptibility values with and without simulated motion. Including all subjects, the same motion caused a wider range of susceptibility changes (5.1 to 43.3%) than the magnitude changes (4.4 to 19.7%). Figure 3.3 shows the effect of simulated motion on magnitude and susceptibility map of a hemorrhage. Distortion in hemorrhage shapes due to incorporation of simulated motion were observed.

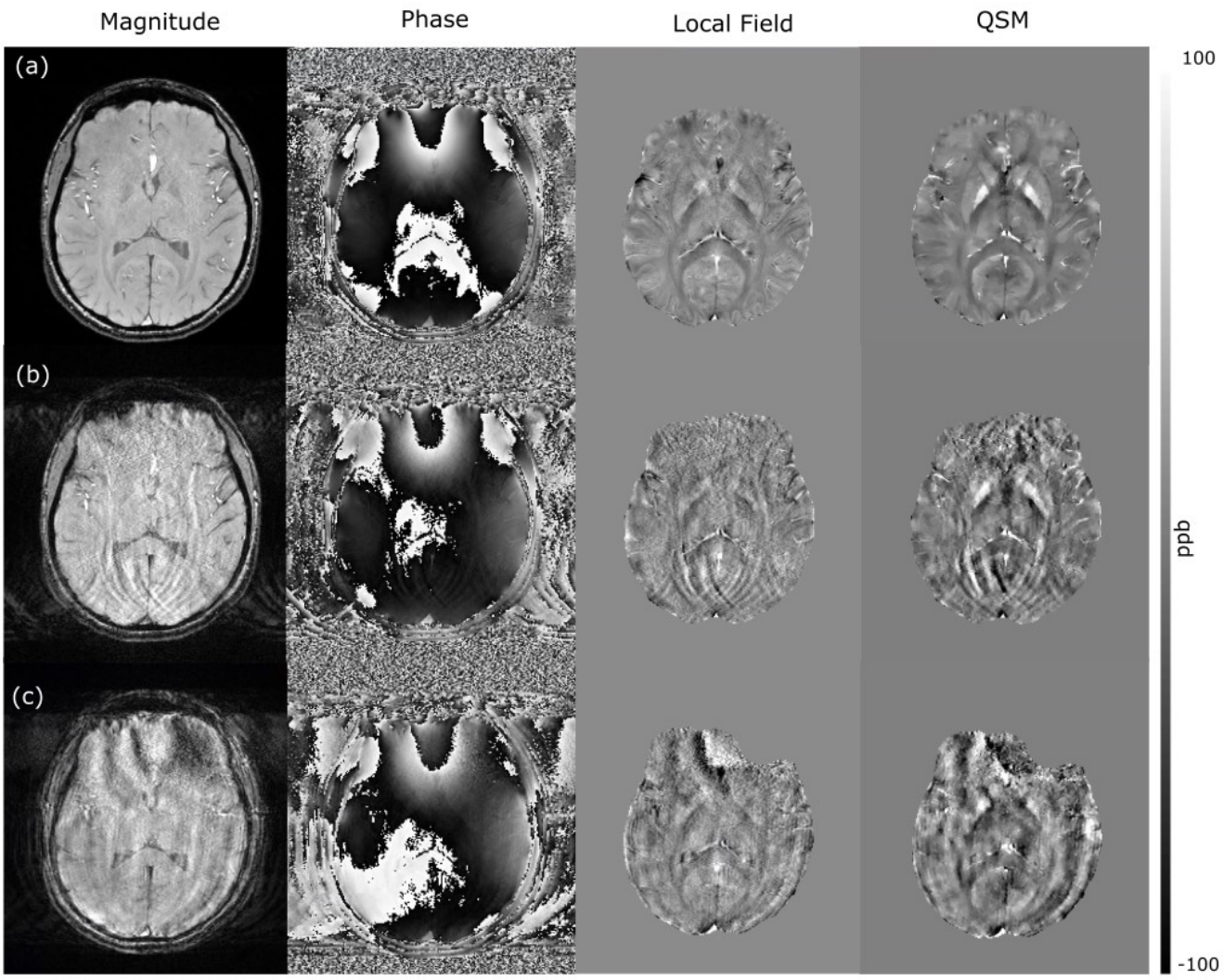

Figure 3.1: Magnitude, phase, local field and QSM of brain of a healthy volunteer (a) without motion, (b) with head movement due to rhythmic movement of head, and (c) with some sharp head motions during the scan. It is observed that both magnitude and QSM were highly distorted due to these motion artifacts.

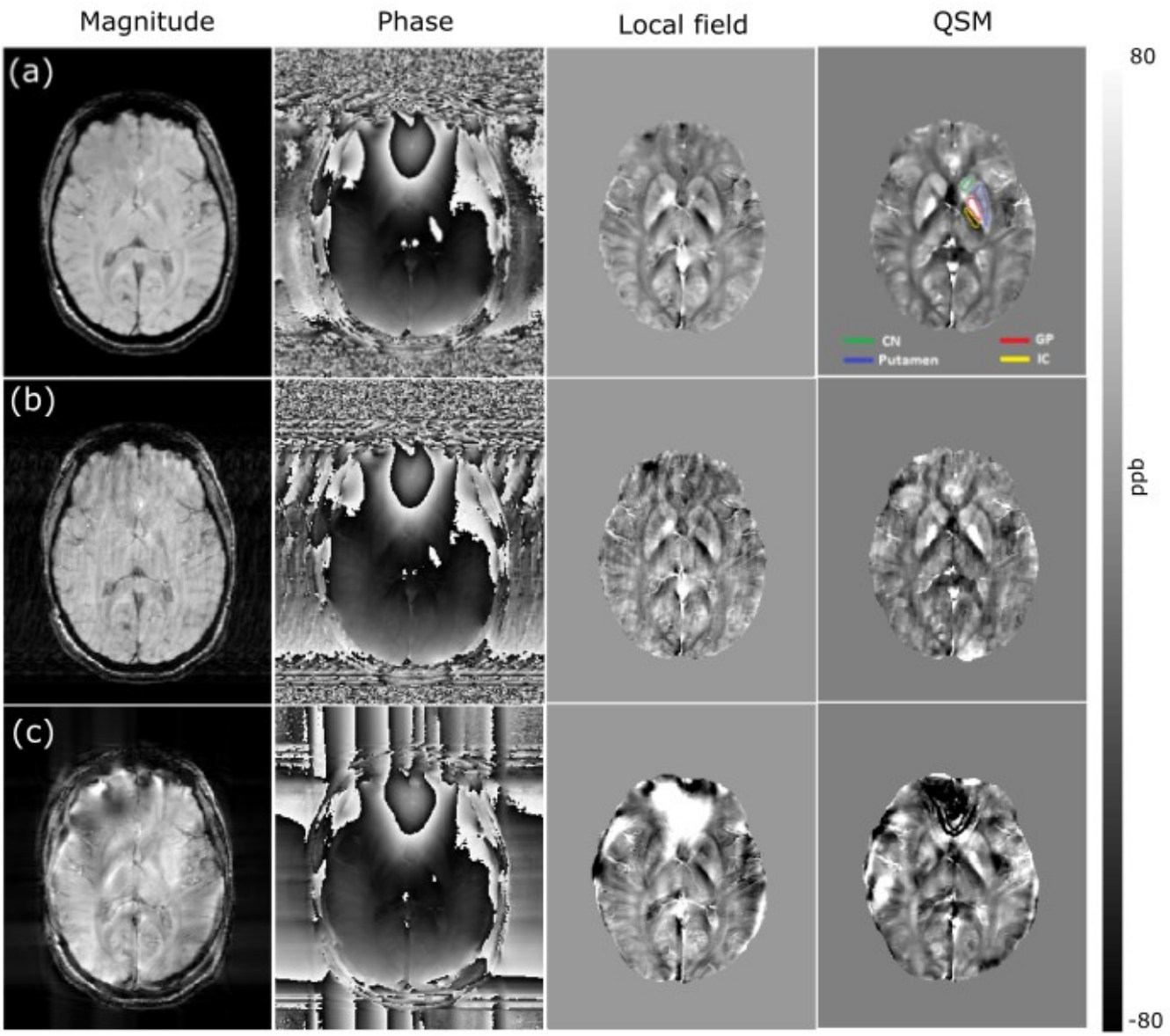

Figure 3.2: Magnitude, phase, local field and QSM on a volunteer where simulated motion was applied as (a) no motion, (b) simulated rhythmic motion (Motion 1), (c) simulated abrupt change of head location (Motion 2). ROIs of brain structures were manually segmented for quantitative analysis of mean susceptibility measurement as shown on QSM.

Table 3.1 Mean (range) of percentage difference between images with and without simulated movement.

	Globus Pallidus		Putamen		Internal Capsule		Caudate nucleus	
	QSM	Mag-nitude	QSM	Mag-nitude	QSM	Mag-nitude	QSM	Mag-nitude
Rhythmic motion (Motion 1)	5.1 [1.3-13.9]	10.7 [1.8-30.1]	30.7* [2.9-60.9]	7.4 [1.1-30.7]	8.6 [1.6-13.9]	4.4 [1.1-8.9]	21.3 [6.5-45.1]	6.1 [1.2-20.7]
Change of head position (Motion 2)	22.9* [8.0-36.8]	18.5* [3.5-31.7]	40.5* [20.0-69.1]	19.7 [14.0-34.6]	34.1* [7.1-50.0]	12.1 [6.6-35.4]	43.3* [9.3-108.9]	18.2* [3.8-39.9]

* indicates statistically significant difference between images with and without simulated motion

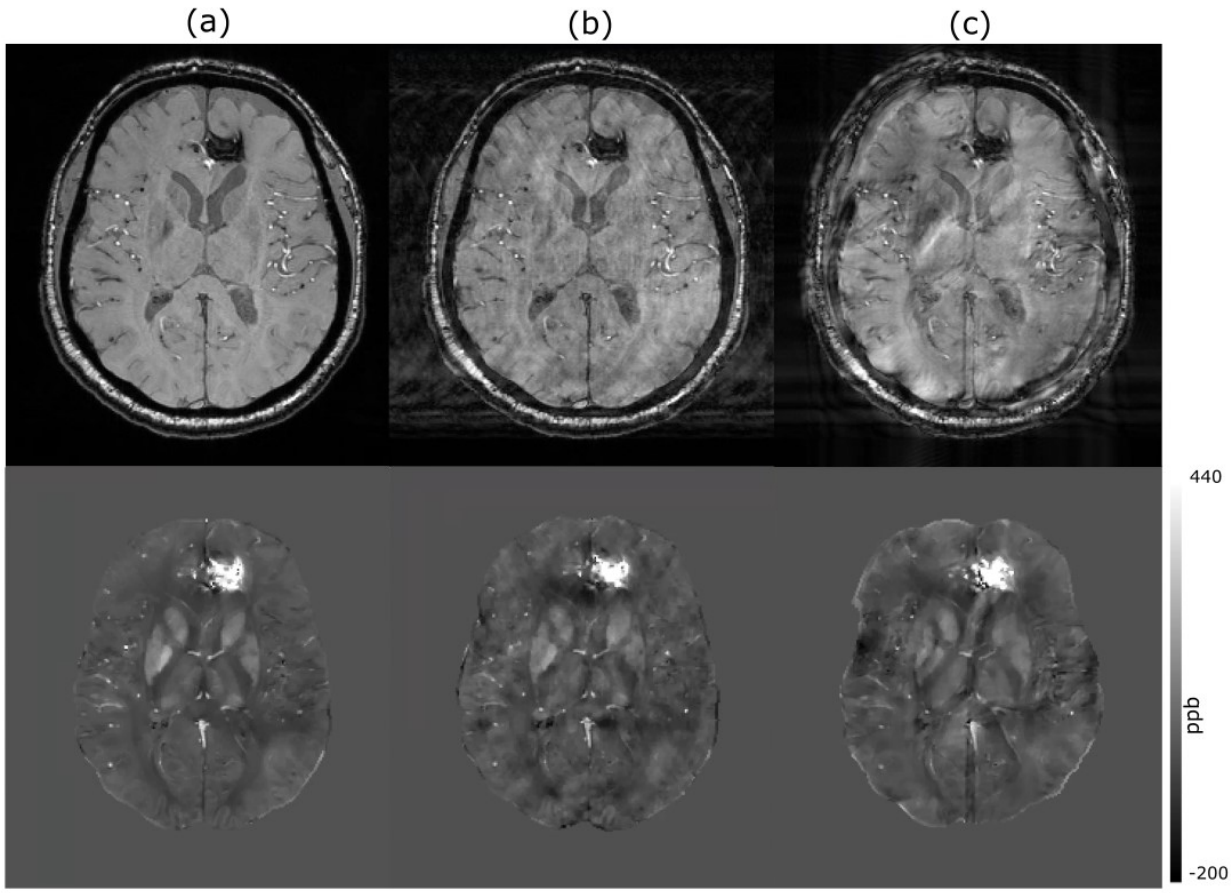

Figure 3.3: Magnitude and QSM on a hemorrhage patient where simulated motion was applied as (a) no motion, (b) simulated rhythmic motion (Motion 1), (c) simulated abrupt change of head location (Motion 2).

Table 3.2 shows the susceptibility values for inhale, exhale, and free breathing using rapid EPI acquisitions. No statistically significant difference was observed between the susceptibility values from the three different breathing conditions for any of the structures. Figure 3.4 shows the effect of correcting for respiratory fluctuation using navigator sequence. Table 3.3 shows the difference in susceptibility values between uncorrected and navigator-corrected QSM. Small differences of 2.2 to 12.2 ppb were observed between the susceptibility values before and after correcting for

respiration. No statistically significant difference was observed between the susceptibility values before and after correction.

Table 3.2. Susceptibility values (mean± s.d.) in inhale, exhale and free breathing condition. No statistically significant difference was observed between the inhale, exhale and free breathing conditions for the susceptibility value.

Susceptibility values (mean±s.d.) (ppb)	Globus Pallidus		Putamen		Internal Capsule		Dentate nucleus	
	Left	Right	Left	Right	Left	Right	Left	Right
Inhale	118.4 ±13.8	119.6 ±11.1	29.0 ±13.7	32.8 ±7.8	-56.6 ±9.4	-58.6 ±6.5	116.0 ±13.7	99.7 ±22.2
Exhale	120.0 ±15.2	114.4 ±14.6	27.8 ±14.6	31.8 ±6.6	-56.8 ±9.7	-58.8 ±8.7	108.5 ±15.9	90.0 ±22.9
Free-breathing	119.4 ±13.9	118.4 ±13.4	30.4 ±12.6	35.2 ±8.6	-56.8 ±7.9	-58.4 ±7.9	114.7 ±17.0	98.5 ±23.0

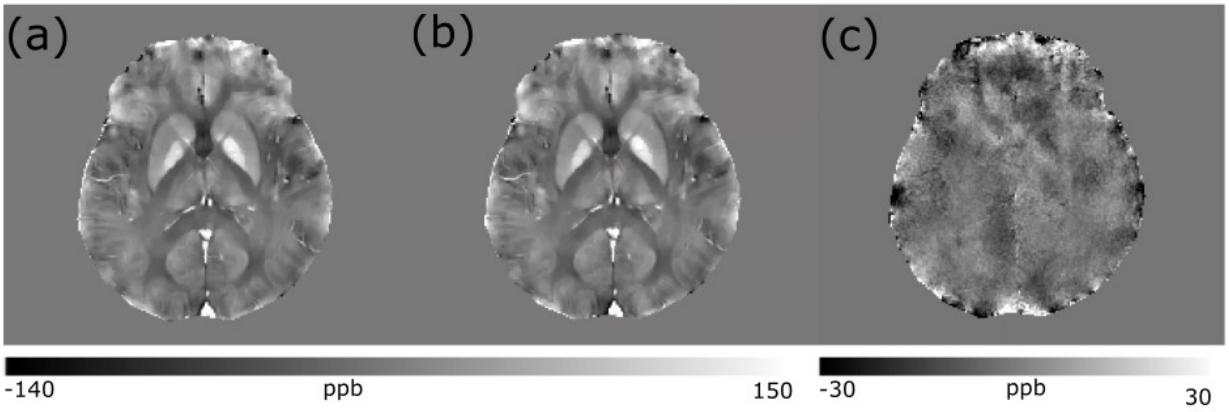

Figure 3.4: QSM on a volunteer (a) before applying navigator correction, (b) after navigator correction and (c) difference susceptibility maps before and after navigator correction.

Table 3.3. Absolute difference (ppb) between the mean susceptibility values before and after navigator correction for respiratory fluctuations. No statistically significant difference was observed between the mean susceptibility values before and after navigator correction.

Absolute susceptibility difference (ppb)	Globus Pallidus		Putamen		Internal Capsule		Dentate nucleus	
	Left	Right	Left	Right	Left	Right	Left	Right
	6.4±4.6	6.2±5.4	2.2±1.6	2.2±2.5	3.2±2.6	4.6±2.7	10.2±10.8	12.2±11.7

3.4 Discussion

This study investigated the effect of motion from translation and respiratory fluctuation on susceptibility values in iron-rich deep grey matter at 3T. Rhythmic and intermittent translation was first performed to clarify the greater sensitivity of QSM to motion compared to standard magnitude images. Rapid QSM with EPI was then performed to assess susceptibility differences between

breath-holds and free breathing and no statistical differences was found. Lastly, comparison of QSM results before and after navigator correction using a typical 3D MEGE approach indicated changes of 2.2 to 12.2 ppb. QSM is dependent on phase and respiratory fluctuation can add a phase offset causing susceptibility differences [22], [32].

These studies have two main findings. First, QSM is much more sensitive to translation than magnitude images and motion can lead to highly inaccurate susceptibility measurements. Particularly in motion-prone subjects, means to minimize subject motion are essential and may require prospective or retrospective motion corrections [18], [36] or much faster sequences [8], [39]-[42]. Second, respiratory fluctuations did not cause any severe artifact in susceptibility images; however, there were differences in susceptibility values. Respiratory effects have been noted in past studies [22], [32], but actual susceptibility differences were not reported. In our study differences between breath-hold and free breathing were not statistically significant for EPI sequences. In free breathing 3D MEGE experiments with a navigator echo correction difference of about 2.2 to 12.2 ppb were found between corrected and uncorrected results for each volunteer, however, the difference was not statistically significant between the corrected and uncorrected group. Respiratory fluctuations do not cause severe artifacts in the susceptibility maps; however, differences in susceptibility values can be observed and physiological noise correction has been shown to improve reproducibility for QSM and R2*[19]. Hence, correcting for respiratory fluctuations can be beneficial for repeatability and reproducibility [35], [43] of susceptibility measurements.

Limitations of this study include an incomplete range of motion patterns investigated, as possible patterns are somewhat limitless. Nevertheless, our results show the clear distinction between magnitude and QSM translation artifacts. Only a few regions in deep grey matter and neighboring

internal capsule were studied. Whole brain analysis could have been more insightful, but the iron-rich deep grey matter region remains a key focus for QSM. Regions nearer the brain edges would likely have much more severe changes. Finally, the subject numbers were relatively small, although sufficient to indicate the main points.

In conclusion, while QSM has an increased sensitivity to motion over magnitude images; typical respiratory fluctuations did not cause large differences in susceptibility values at 3T in iron rich deep grey matter. Particularly for motion-prone subjects, means to manage motion artifacts remain an ongoing concern particularly when long, high resolution acquisitions are required.

3.5 Acknowledgements

Research support from Canadian Institutes of Health Research.

We thank Mitacs for their Globalink Graduate Fellowship

References

[1] W. Chen *et al.*, "Intracranial calcifications and hemorrhages: characterization with quantitative susceptibility mapping," *Radiology*, vol. 270, no. 2, pp. 496–505, Feb. 2014, doi: 10.1148/radiol.13122640.

[2] A. Deistung *et al.*, "Quantitative susceptibility mapping differentiates between blood depositions and calcifications in patients with glioblastoma," *PloS One*, vol. 8, no. 3, p. e57924, 2013, doi: 10.1371/journal.pone.0057924.

[3] J. R. Reichenbach, F. Schweser, B. Serres, and A. Deistung, "Quantitative Susceptibility Mapping: Concepts and Applications," *Clin. Neuroradiol.*, vol. 25 Suppl 2, pp. 225–230, Oct. 2015, doi: 10.1007/s00062-015-0432-9.

[4] S. Wang, M. Lou, T. Liu, D. Cui, X. Chen, and Y. Wang, “Hematoma volume measurement in gradient echo MRI using quantitative susceptibility mapping,” *Stroke*, vol. 44, no. 8, pp. 2315–2317, Aug. 2013, doi: 10.1161/STROKEAHA.113.001638.

[5] S. Chang *et al.*, “Quantitative Susceptibility Mapping of Intracerebral Hemorrhages at Various Stages,” *J. Magn. Reson. Imaging JMRI*, vol. 44, no. 2, pp. 420–425, Aug. 2016, doi: 10.1002/jmri.25143.

[6] H. Sun, M. Kate, L. C. Gioia, D. J. Emery, K. Butcher, and A. H. Wilman, “Quantitative susceptibility mapping using a superposed dipole inversion method: Application to intracranial hemorrhage,” *Magn. Reson. Med.*, vol. 76, no. 3, pp. 781–791, Sep. 2016, doi: 10.1002/mrm.25919.

[7] H. Sun *et al.*, “Quantitative Susceptibility Mapping for Following Intracranial Hemorrhage,” *Radiology*, vol. 288, no. 3, pp. 830–839, Sep. 2018, doi: 10.1148/radiol.2018171918.

[8] A. De, H. Sun, D. J. Emery, K. S. Butcher, and A. H. Wilman, “Rapid quantitative susceptibility mapping of intracerebral hemorrhage,” *J. Magn. Reson. Imaging JMRI*, vol. 51, no. 3, pp. 712–718, Mar. 2020, doi: 10.1002/jmri.26850.

[9] N.-J. Gong, R. Dibb, M. Bulk, L. van der Weerd, and C. Liu, “Imaging beta amyloid aggregation and iron accumulation in Alzheimer’s disease using quantitative susceptibility mapping MRI,” *NeuroImage*, vol. 191, pp. 176–185, May 2019, doi: 10.1016/j.neuroimage.2019.02.019.

[10] H.-G. Kim *et al.*, “Quantitative susceptibility mapping to evaluate the early stage of Alzheimer’s disease,” *NeuroImage Clin.*, vol. 16, pp. 429–438, 2017, doi: 10.1016/j.nicl.2017.08.019.

[11] P. M. Cogswell *et al.*, “Associations of quantitative susceptibility mapping with Alzheimer’s

disease clinical and imaging markers," *NeuroImage*, vol. 224, p. 117433, Jan. 2021, doi: 10.1016/j.neuroimage.2020.117433.

[12] C. Langkammer *et al.*, "Quantitative susceptibility mapping in multiple sclerosis," *Radiology*, vol. 267, no. 2, pp. 551–559, May 2013, doi: 10.1148/radiol.12120707.

[13] C. Wisnieff, S. Ramanan, J. Olesik, S. Gauthier, Y. Wang, and D. Pitt, "Quantitative susceptibility mapping (QSM) of white matter multiple sclerosis lesions: Interpreting positive susceptibility and the presence of iron," *Magn. Reson. Med.*, vol. 74, no. 2, pp. 564–570, Aug. 2015, doi: 10.1002/mrm.25420.

[14] S. Eskreis-Winkler *et al.*, "Multiple sclerosis lesion geometry in quantitative susceptibility mapping (QSM) and phase imaging," *J. Magn. Reson. Imaging JMRI*, vol. 42, no. 1, pp. 224–229, Jul. 2015, doi: 10.1002/jmri.24745.

[15] B. Xiao *et al.*, "Quantitative susceptibility mapping based hybrid feature extraction for diagnosis of Parkinson's disease," *NeuroImage Clin.*, vol. 24, p. 102070, 2019, doi: 10.1016/j.nicl.2019.102070.

[16] Z. Cheng *et al.*, "Imaging the Nigrosome 1 in the substantia nigra using susceptibility weighted imaging and quantitative susceptibility mapping: An application to Parkinson's disease," *NeuroImage Clin.*, vol. 25, p. 102103, 2020, doi: 10.1016/j.nicl.2019.102103.

[17] S. Tan *et al.*, "Utility of quantitative susceptibility mapping and diffusion kurtosis imaging in the diagnosis of early Parkinson's disease," *NeuroImage Clin.*, vol. 32, p. 102831, 2021, doi: 10.1016/j.nicl.2021.102831.

[18] F. Godenschweger *et al.*, "Motion correction in MRI of the brain," *Phys. Med. Biol.*, vol. 61, no. 5, pp. R32–R56, Mar. 2016, doi: 10.1088/0031-9155/61/5/R32.

[19] J. Y. Choi, J. Lee, Y. Nam, J. Lee, and S.-H. Oh, "Improvement of reproducibility in

quantitative susceptibility mapping (QSM) and transverse relaxation rates (R2*) after physiological noise correction," *J. Magn. Reson. Imaging JMRI*, vol. 49, no. 6, pp. 1769–1776, Jun. 2019, doi: 10.1002/jmri.26522.

[20] J. Meineke *et al.*, "Motion artifacts in standard clinical setting obscure disease-specific differences in quantitative susceptibility mapping," *Phys. Med. Biol.*, vol. 63, no. 14, p. 14NT01, Jul. 2018, doi: 10.1088/1361-6560/aacc52.

[21] H. Mattern, A. Sciarra, F. Lüsebrink, J. Acosta-Cabronero, and O. Speck, "Prospective motion correction improves high-resolution quantitative susceptibility mapping at 7T," *Magn. Reson. Med.*, vol. 81, no. 3, pp. 1605–1619, Mar. 2019, doi: 10.1002/mrm.27509.

[22] S. J. Vannesjo *et al.*, "Retrospective correction of physiological field fluctuations in high-field brain MRI using concurrent field monitoring," *Magn. Reson. Med.*, vol. 73, no. 5, pp. 1833–1843, May 2015, doi: 10.1002/mrm.25303.

[23] N. F. Ramsey et al., "Phase navigator correction in 3D fMRI improves detection of brain activation: quantitative assessment with a graded motor activation procedure," NeuroImage, vol. 8, no. 3, pp. 240–248, Oct. 1998, doi: 10.1006/nimg.1998.0358.

[24] J. Meineke and T. Nielsen, "Data consistency-driven determination of -fluctuations in gradient-echo MRI," Magn. Reson. Med., vol. 81, no. 5, pp. 3046–3055, 2019, doi: 10.1002/mrm.27630.

[25] P. van Gelderen, J. A. de Zwart, P. Starewicz, R. S. Hinks, and J. H. Duyn, "Real-time shimming to compensate for respiration-induced B0 fluctuations," Magn. Reson. Med., vol. 57, no. 2, pp. 362–368, Feb. 2007, doi: 10.1002/mrm.21136.

[26] Y. Duerst et al., "Utility of real-time field control in T2 *-Weighted head MRI at 7T," Magn. Reson. Med., vol. 76, no. 2, pp. 430–439, Aug. 2016, doi: 10.1002/mrm.25838.

[27] S. M. Smith, “Fast robust automated brain extraction,” Hum. Brain Mapp., vol. 17, no. 3, pp. 143–155, Nov. 2002, doi: 10.1002/hbm.10062.

[28] M. Jenkinson, “Fast, automated, N-dimensional phase-unwrapping algorithm,” Magn. Reson. Med., vol. 49, no. 1, pp. 193–197, Jan. 2003, doi: 10.1002/mrm.10354.

[29] H. Sun and A. H. Wilman, “Background field removal using spherical mean value filtering and Tikhonov regularization,” Magn. Reson. Med., vol. 71, no. 3, pp. 1151–1157, 2014, doi: 10.1002/mrm.24765.

[30] B. Bilgic, A. Pfefferbaum, T. Rohlfing, E. V. Sullivan, and E. Adalsteinsson, “MRI estimates of brain iron concentration in normal aging using quantitative susceptibility mapping,” NeuroImage, vol. 59, no. 3, pp. 2625–2635, Feb. 2012, doi: 10.1016/j.neuroimage.2011.08.077.

[31] H. Sun et al., “Extracting more for less: multi-echo MP2RAGE for simultaneous T1 -weighted imaging, T1 mapping, R 2 ∗ mapping, SWI, and QSM from a single acquisition,” Magn. Reson. Med., vol. 83, no. 4, pp. 1178–1191, Apr. 2020, doi: 10.1002/mrm.27975.

[32] J. Wen, A. H. Cross, and D. A. Yablonskiy, “On The Role of Physiological Fluctuations in Quantitative Gradient Echo MRI – Implications for GEPCI, QSM and SWI,” *Magn. Reson. Med.*, vol. 73, no. 1, pp. 195–203, Jan. 2015, doi: 10.1002/mrm.25114.

[33] P.-F. Van de Moortele, J. Pfeuffer, G. H. Glover, K. Ugurbil, and X. Hu, “Respiration-induced B0 fluctuations and their spatial distribution in the human brain at 7 Tesla,” *Magn. Reson. Med.*, vol. 47, no. 5, pp. 888–895, May 2002, doi: 10.1002/mrm.10145.

[34] Y. Nam, D.-H. Kim, and J. Lee, “Physiological noise compensation in gradient-echo myelin water imaging,” *NeuroImage*, vol. 120, pp. 345–349, Oct. 2015, doi: 10.1016/j.neuroimage.2015.07.014.

[35] X. Feng, A. Deistung, and J. R. Reichenbach, “Quantitative susceptibility mapping (QSM) and R2* in the human brain at 3T: Evaluation of intra-scanner repeatability,” *Z. Für Med. Phys.*, vol. 28, no. 1, pp. 36–48, Feb. 2018, doi: 10.1016/j.zemedi.2017.05.003.

[36] M. Zaitsev, J. Maclaren, and M. Herbst, “Motion artifacts in MRI: A complex problem with many partial solutions,” J. Magn. Reson. Imaging JMRI, vol. 42, no. 4, pp. 887–901, Oct. 2015, doi: 10.1002/jmri.24850.

[37] R. L. Ehman and J. P. Felmlee, “Adaptive technique for high-definition MR imaging of moving structures,” Radiology, vol. 173, no. 1, pp. 255–263, Oct. 1989, doi: 10.1148/radiology.173.1.2781017.

[38] K. Gumus et al., “Comparison of optical and MR-based tracking,” Magn. Reson. Med., vol. 74, no. 3, pp. 894–902, Sep. 2015, doi: 10.1002/mrm.25472.

[39] C. Langkammer et al., “Fast quantitative susceptibility mapping using 3D EPI and total generalized variation,” NeuroImage, vol. 111, pp. 622–630, May 2015, doi: 10.1016/j.neuroimage.2015.02.041.

[40] D. Stäb, S. Bollmann, C. Langkammer, K. Bredies, and M. Barth, “Accelerated mapping of magnetic susceptibility using 3D planes-on-a-paddlewheel (POP) EPI at ultra-high field strength,” NMR Biomed., vol. 30, no. 4, Apr. 2017, doi: 10.1002/nbm.3620.

[41] B. Bilgic, H. Ye, L. L. Wald, and K. Setsompop, “Simultaneous Time Interleaved MultiSlice (STIMS) for Rapid Susceptibility Weighted Acquisition,” NeuroImage, vol. 155, pp. 577–586, Jul. 2017, doi: 10.1016/j.neuroimage.2017.04.036.

[42] H. Sun and A. H. Wilman, “Quantitative susceptibility mapping using single-shot echo-planar imaging,” Magn. Reson. Med., vol. 73, no. 5, pp. 1932–1938, May 2015, doi: 10.1002/mrm.25316.

[43] P.-Y. Lin, T.-C. Chao, and M.-L. Wu, “Quantitative susceptibility mapping of human brain at 3T: a multisite reproducibility study,” AJNR Am. J. Neuroradiol., vol. 36, no. 3, pp. 467–474, Mar. 2015, doi: 10.3174/ajnr.A4137.

Chapter 4

Quantitative susceptibility weighted imaging in presence of strong susceptibility sources: Application to hemorrhage*

Abstract

Purpose: To optimize quantitative susceptibility weighted imaging also known as true susceptibility weighted imaging (tSWI) for strong susceptibility sources like

*A version of this chapter has been accepted in MRI: A. De, H. Sun, D. J. Emery, K. S. Butcher, and A. H. Wilman," Quantitative susceptibility-weighted imaging in presence of strong susceptibility sources: Application to hemorrhage", Magn. Reson. Imaging MRI

hemorrhage and compare to standard susceptibility weighted imaging (SWI) and quantitative susceptibility mapping (QSM).

Methods: Ten patients with known intracerebral hemorrhage were scanned using a 3D SWI sequence. The magnitude and phase images were utilized to compute QSM, tSWI and SWI images. tSWI parameters including the upper threshold for creating susceptibility weighted masks and the multiplication factor were optimized for hemorrhage depiction. Combined tSWI was also computed with independent optimized parameters for both veins and hemorrhagic regions. tSWI results were compared to SWI and QSM utilizing region-of-interest measurements, Pearson's correlation and Kruskal-Wallis test.

Results: Fifteen hemorrhages were found, with mean susceptibility 0.81±0.37 ppm. Unlike SWI which utilizes a phase mask, tSWI uses a mask computed from QSM. In tSWI, the weighted mask required an extended upper threshold far beyond the standard level for more effective visualization of hemorrhage texture. The upper threshold was set to the mean maximum susceptibility in the hemorrhagic region (3.24 ppm) with a multiplication factor of 2. The blooming effect, seen in SWI, was observed to be larger in hemorrhages with higher susceptibility values ($r = 0.78$, $p<0.001$) with reduced blooming on tSWI. On SWI, 4 out of 15 hemorrhages showed phase wrap artifacts in the hemorrhagic region and all patients showed some phase wraps in the air-tissue interface near the auditory and frontal sinuses. These phase wrap artifacts were absent on tSWI. In hemorrhagic region, a higher correlation was observed between the actual susceptibility values and mean gray value for tSWI ($r = -0.93$, $p<0.001$) than SWI ($r = -0.87$, $p<0.001$).

Conclusion: In hemorrhage, tSWI minimizes both blooming effects and phase wrap artifacts observed in SWI. However, unlike SWI, tSWI requires an altered upper threshold for best hemorrhage depiction that greatly differs from the standard value. tSWI can be used as a complementary technique for visualizing hemorrhage along with SWI.

4.1 Introduction

Susceptibility weighted imaging (SWI) combines magnitude with filtered and thresholded phase images acquired from a gradient echo (GRE) sequence to improve the visibility of various paramagnetic susceptibility sources such as hemorrhage, veins and microbleeds. Currently, it has a wide range of clinical applications [1–8]. However, particularly for strong susceptibility sources, SWI images may have artifacts arising from unwrapped phase and blooming effects. In addition, phase is highly dependent on object's orientation with the main field [9]. These limitations have led to the recent introduction of quantitative SWI also known as true SWI (tSWI) [10-12] which replaces the filtered phase mask with thresholded Quantitative Susceptibility Mapping (QSM). Susceptibility maps [13] are produced from the raw phase images of a GRE sequence and also offer a means to study iron changes in hematoma quantitatively [14-18]. tSWI has been applied to brain studies showing that veins and microbleeds [10] have reduced artifacts and brain tissues have improved contrast [11]. However, unlike SWI which thresholds the phase image around the zero value, tSWI must set a minimum and maximum susceptibility threshold. In work to date, a standard

threshold has been sufficient, but cases of strong susceptibility sources have not been studied in detail.

Such a strong susceptibility source is hemorrhage, which has concentrated sources of iron from various forms of hemoglobin depending on age. Specifically, intracerebral hemorrhage (ICH) is a type of stroke where blood vessels rupture and lead to blood leakage in the brain. The leaked hemoglobin is toxic to the brain tissue and can lead to further inflammation and increased injury [19-21]. As the hemorrhage ages, the accumulated hemoglobin changes its form resulting in variations in susceptibility [17,20].

Both SWI and QSM have been applied to study iron changes in ICH evolution [17]. QSM provides reliable measurements of the hemorrhage without any blooming artifacts or phase wraps [14]. Previous studies have also shown QSM to be useful for distinguishing hemorrhage from calcification [22], measuring hematoma volume [14] and following iron changes [17]. Similarly, SWI has proven useful for hemorrhage [4,5], but can suffer from extreme blooming effects as well as phase unwrapping difficulties due to the strong susceptibility sources.

In this work, we examine the use of tSWI for strong susceptibility sources like hemorrhage by determining optimal thresholds, then compare it to both standard SWI and to QSM using quantitative measures.

4.2 Methods

4.2.1. Patient studies

Written consent was obtained from patients or substitute decision makers and the protocol was approved by the local Ethics Committee. Fifteen hemorrhages were studied from 10 patients (6 female/4 male; age: 76±12 years). The patients were diagnosed with ICH by CT and received a follow-up MRI scan from day 2 to day 30 after symptom onset. Three patients were scanned longitudinally on days 2, 7 and 30 approximately.

4.2.2. MRI Pulse Sequence

The MRI protocol was performed at 3T (Siemens Prisma, Erlangen, Germany) using an axial-oblique 3D single echo GRE sequence with the following parameters: echo time (TE) 20 ms, repetition time (TR) 27 ms, resolution 0.9X0.9X1.5mm^3, flip angle 15^0, in-plane field of view (FOV) 200×220 mm², 80 slices, acquisition time 4.54 minutes, first order gradient moment nulling and GRAPPA parallel imaging with acceleration factor of 2 along the primary phase-encoding direction.

4.2.3. Image reconstruction

The magnitude and phase images provide the starting point for all three reconstructions. Both tSWI and QSM reconstruction were performed offline, while SWI was reconstructed by the scanner computer and equivalently offline. All offline processing used MATLAB 2019a (Mathworks, Natick, MA).

SWI images were generated in the standard manner [1] by multiplying the magnitude by four times the filtered phase mask. The filtered phase mask is designed as:

$$filtered\ phase\ mask = \begin{cases} \frac{\pi-\varphi}{\pi} & for\ \varphi > 0 \\ 1 & otherwise \end{cases} \quad \text{.....(4.1)}$$

where φ is the high pass filtered phase SWI is then computed as:

$$SWI = magnitude * (filtered\ phase\ mask)^4 \quad \text{.....(4.2)}$$

The susceptibility maps were reconstructed using the superposed dipole inversion method in order to overcome unreliable phase measurements due to rapid signal decay within the hemorrhagic region [16,18]. Brain Extraction Tool (BET) [23] was utilized for brain extraction, 3D best path unwrapping technique [24] was used to unwrap the phase and background removal was done with LBV (Laplacian Boundary Value) [25], followed by total variation dipole inversion [26].

tSWI is reconstructed using the same magnitude images as used in SWI, but with a thresholded mask produced from QSM rather than from phase images. tSWI was reconstructed by the method described in [10] using a thresholded mask based on susceptibility values, W as follows:

$$W = \begin{cases} 1 & for\ \chi \leq \chi_1 \\ 1 - \frac{\chi - \chi_1}{\chi_2 - \chi_1} & for\ \chi_1 < \chi \leq \chi_2 \\ 0 & for\ \chi > \chi_2 \end{cases} \quad \text{.....(4.3)}$$

where χ is the susceptibility value obtained from QSM, $\chi_1$is the lower threshold and χ_2 is the upper threshold of the range of susceptibility values. Finally, tSWI is generated by multiplying the magnitude image with the susceptibility thresholded mask n times, similar to the usual SWI mask application:

$$tSWI = magnitude * W^n \quad \text{.....(4.4)}$$

tSWI was computed with an upper threshold of 0.45 ppm, as used in previous papers [10,11] and with an increased threshold of 3.24 ppm, the average maximum susceptibility of the hemorrhagic region over all patients in this study. Multiplication factor(n) of 1 to 6 was also studied. The lower susceptibility threshold (χ_1) was chosen to be 0 ppm which provides better contrast for low susceptibility structures and small veins as observed in previous work [10].

To manage wide variations in susceptibility values, a combined tSWI method was also computed, where the susceptibility values of the hemorrhagic and non-hemorrhagic tissue regions were thresholded separately using optimum thresholding parameters. The hemorrhagic region was segmented by setting a threshold on the full brain susceptibility map [16,18]. Regions with susceptibilities greater than 0.5 ppm were extracted as hemorrhagic region. This hemorrhagic region was masked out and an upper threshold of 0.45 ppm was used on the susceptibility map with the remaining tissue to make the thresholded mask for the tissue region. The susceptibility map with the hemorrhagic region [16,18] was used to produce the thresholded mask with upper threshold of 3.24 ppm. A combined thresholded mask was then generated by adding the

thresholded mask of hemorrhagic region with 3.24 ppm upper threshold to the thresholded mask of the tissue region with 0.45 ppm upper threshold. After this step, the combined thresholded mask was multiplied n times with the magnitude to produce the combined tSWI.

4.2.4. Image Analysis

For each imaging method (tSWI, SWI, QSM), regions-of-interest (ROIs) for volume measurement and mean signal intensity or susceptibility were manually drawn and analyzed with ITK-Snap 3.8.0. Each imaging method was considered independently, blinded to the other methods. The mean signal intensities on tSWI or SWI and susceptibility values on QSM were determined from the hemorrhage volumes and compared by using their independent ROIs. Correlations between susceptibility values and mean signal intensities from tSWI images computed with different multiplication factors were obtained. The signal variation across the hemorrhagic area was studied by plotting histograms over the hemorrhagic region. Presence of phase artifacts was also recorded.

4.2.5. Statistical Analysis

All statistical analyses were performed either using STATA/IC 12.0 or R 4.1.1. Pearson's correlation coefficients were calculated for correlating hemorrhage mean gray value from different post-processing methods with susceptibility and for the correlation of susceptibility values with mean gray values from tSWI obtained by using different multiplication factors. The Kruskal–

Wallis test was performed to compare the volumes of hemorrhagic regions between the groups of post-processing methods. The association between susceptibility values with percentage of volume difference between tSWI and SWI were also assessed using Pearson's correlation coefficient.

4.3 Results

Figure 4.1 shows images and histograms comparing the pixel intensity variation over a hemorrhagic area for magnitude, SWI, tSWI for different upper thresholds of tSWI including standard (0.45 ppm), or a higher threshold of the mean maximum hemorrhagic value (3.24 ppm). Combined tSWI with different upper thresholds for hemorrhagic and non-hemorrhagic region is also shown. The Day 26 hemorrhage is observed to have a magnitude image with dark rim with hyperintense middle and some hypointensity in the core suggesting a hemosiderin rim with extracellular methemoglobin in the middle and intracellular methemoglobin in the core. tSWI with upper threshold of 0.45 ppm has majority of hemorrhagic pixel intensities at zero as observed in the histogram which makes minimal use of the gray scale range in the hemorrhage. By increasing the upper threshold, tSWI of hemorrhage depicts the internal hemorrhagic signal variations more effectively. However, the high upper threshold also limits non-hemorrhagic tissue contrast, that is recovered by using a combined upper threshold with standard value of 0.45ppm outside of the hemorrhage region. Since it is desired to observe signal variation across the hemorrhages, the average of the maximum susceptibility of the hemorrhagic regions across all patients (3.24 ppm), was chosen as the upper threshold for all further images.

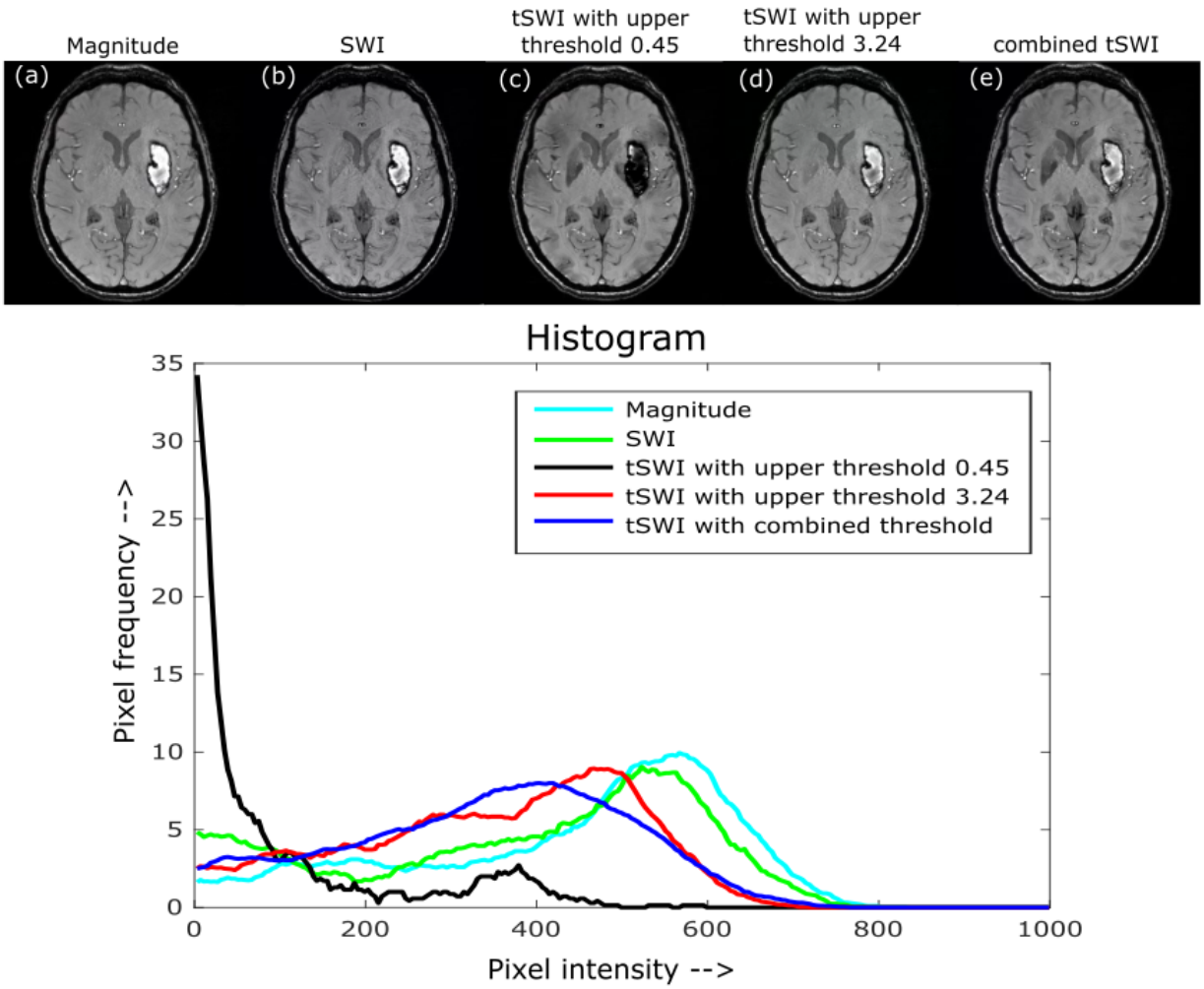

Figure 4.1: Magnitude, SWI and tSWI images with different parameters on a patient with Day 26 hemorrhage. The histograms of the hemorrhagic region from magnitude(a), SWI(b), tSWI with standard upper threshold (0.45 ppm) (c), tSWI with an increased threshold to the level of the mean maximum susceptibility (3.24 ppm) (d) and tSWI with a combined threshold using standard values of 0.45 ppm for non-hemorrhagic and 3.24 for hemorrhagic regions (e) is also shown. tSWI used a multiplicative factor of n = 2.

To determine the optimal multiplication factor, a correlation of susceptibility values was computed with mean signal intensity of tSWI images with multiplication factors of n = 1 to 6. The correlations were observed to be very similar (r = -0.74 to -0.76, $p<0.05$) and hence n = 2 was chosen as used in previous tSWI work [7,8]. Figure 4.2 shows tSWI computed using different multiplication factors for a Day 7 hemorrhage patient along with the correlation plot of susceptibility values with mean intensity of tSWI with multiplication factor of 2. In this study, all further images of tSWI of hemorrhages were constructed with parameters of upper threshold (χ_2) of 3.24ppm, lower threshold (χ_1) of 0 ppm and multiplication factor, n of 2.

Figure 4.3 demonstrates an acute hemorrhage on Day 2 with hypointense magnitude suggesting presence of intracellular deoxyhemoglobin. The blooming effect observed in SWI images of hemorrhage is shown with a red arrow.

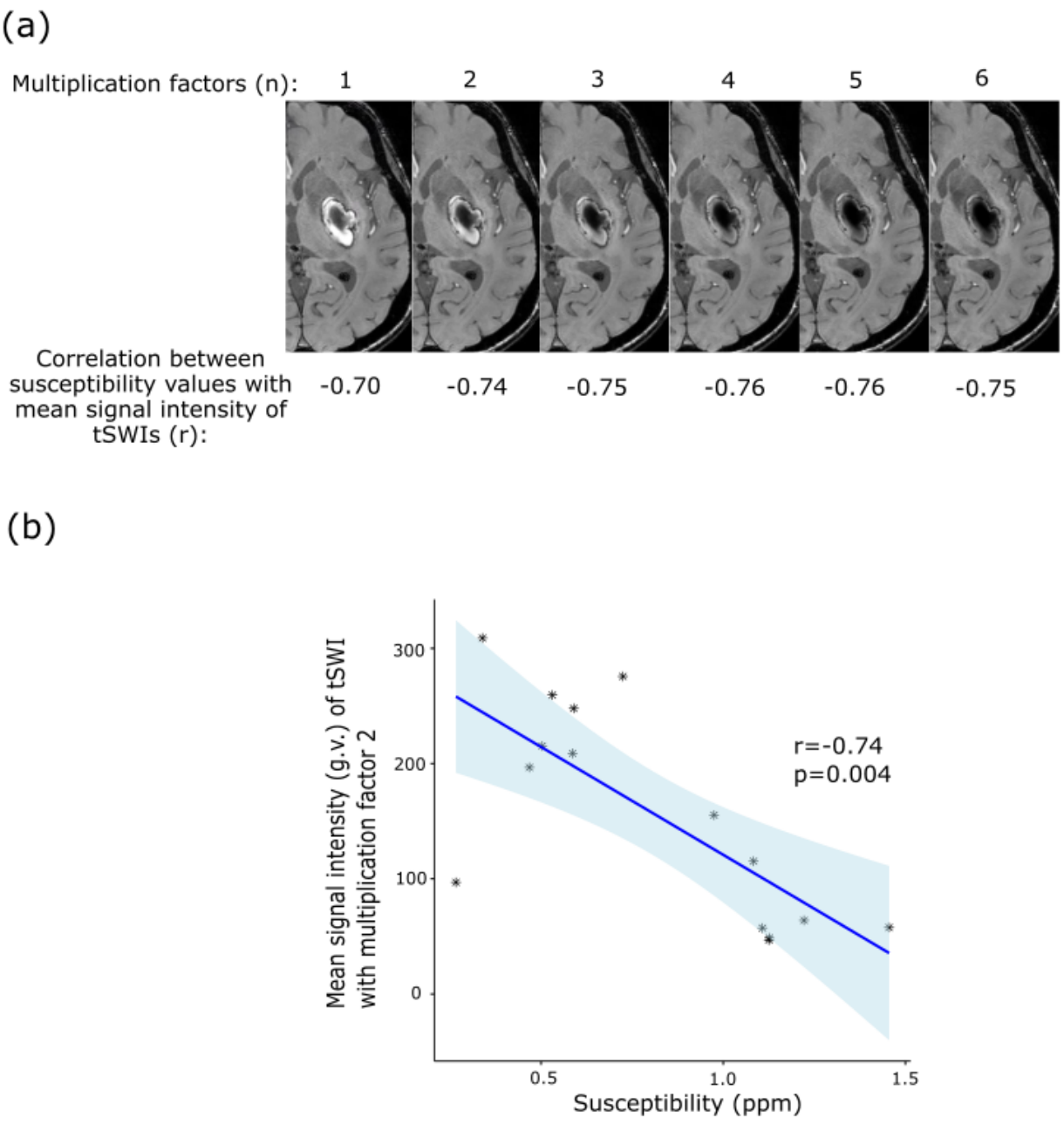

Figure 4.2: (a) The effect of multiplication factor (n) of 1 to 6 on tSWI in a patient with Day 7 hemorrhage. Correlation values for all subjects and n values are shown below each image. (b) The correlation between hemorrhage signal on tSWI with n = 2 and susceptibility for all subjects.

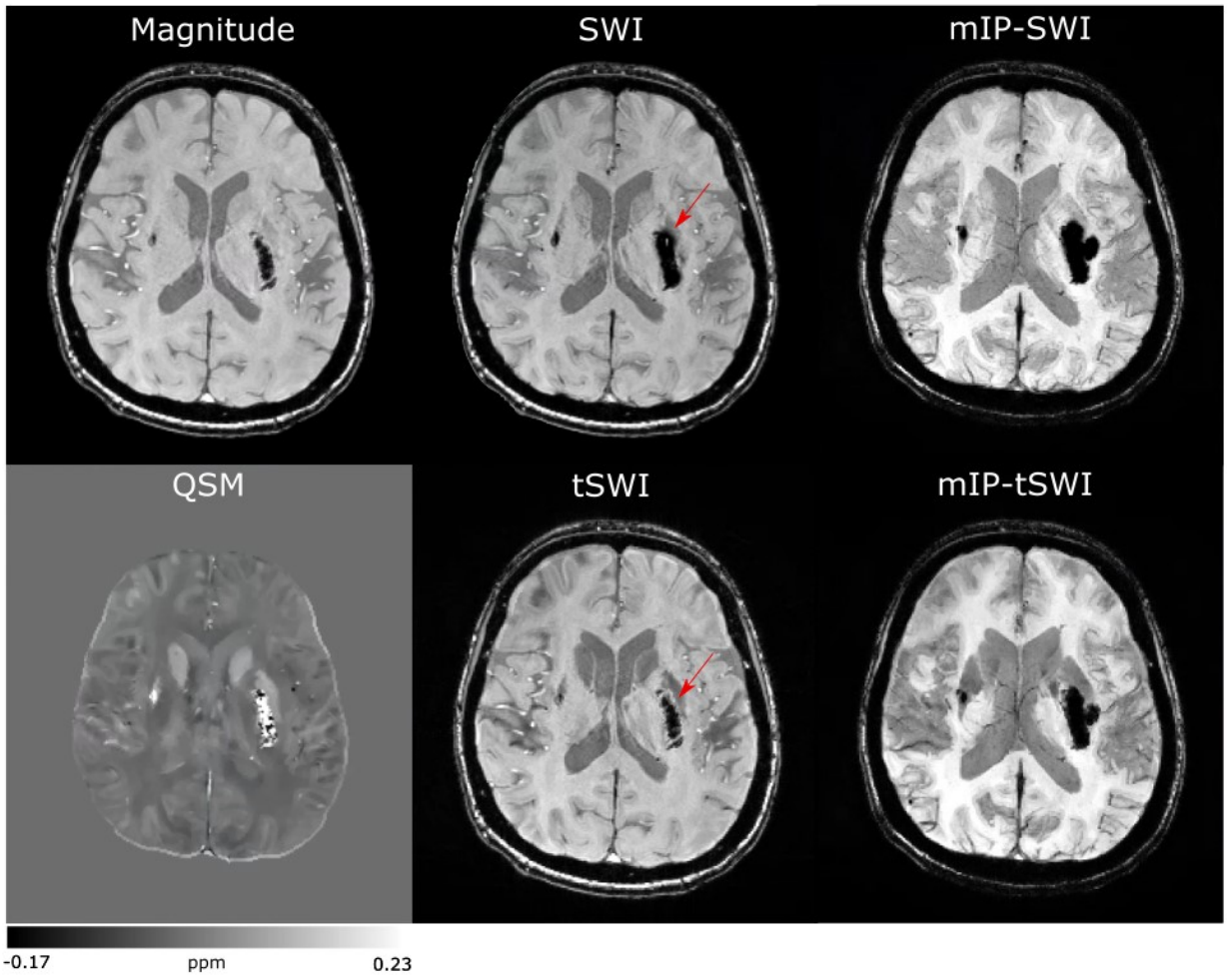

Figure 4.3: Magnitude, SWI, QSM, tSWI and mIP through 7 slices from SWI and tSWI in a patient with an acute Day 2 hemorrhage. It demonstrates the blooming effect in SWI of hemorrhage that is reduced in tSWI as shown by the red arrow.

Figure 4.4(a) shows a boxplot of volumes for all the hemorrhages. No statistically significant difference ($p = 0.66$) was observed among the hemorrhagic volumes obtained from the different post processing methods (QSM, SWI and tSWI). However, the mean volume of the tSWI (14.9 cm^3) and QSM (14.3cm^3) were lower than SWI (17.1 cm^3). Figure 4.4(b) compares the

hemorrhagic volume on QSM with that on SWI(R^2 = 0.96, p<0.001) and tSWI(R^2 = 0.098, p<0.001). The slope of the linear plots showed that blooming effect was higher on SWI than tSWI. Figure 4.4(c) shows the SWI blooming effect of hemorrhage, computed as the percentage difference between the volumes on SWI and tSWI had a strong positive association with susceptibility values (r = 0.78, p<0.001).

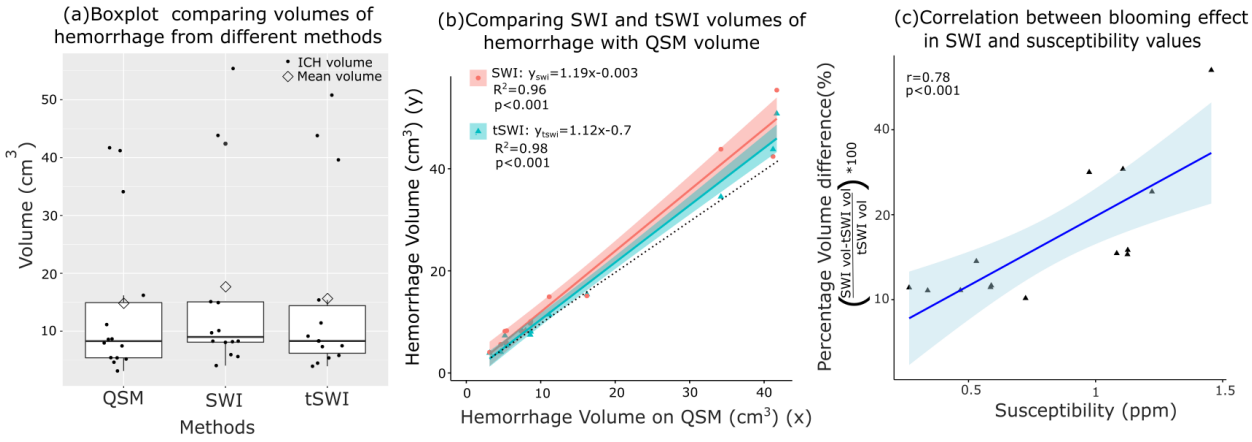

Figure 4.4: (a) Boxplot comparing the volume of QSM, SWI and tSWI. (b) Linear relation of hemorrhage volume of QSM with SWI and tSWI (c) Correlation between blooming effect of SWI with susceptibility values.

The phase, filtered phase, SWI, unwrapped phase, QSM and tSWI of a Day 12 hemorrhage patient in Figure 4.5 demonstrate the artifacts from phase wrap that are observed inside the hemorrhage in the SWI image. Four out of 15 hemorrhages showed these phase wrap artifacts in the hemorrhagic region and all patients showed some phase wraps in the air-tissue interface near the auditory and frontal sinuses.

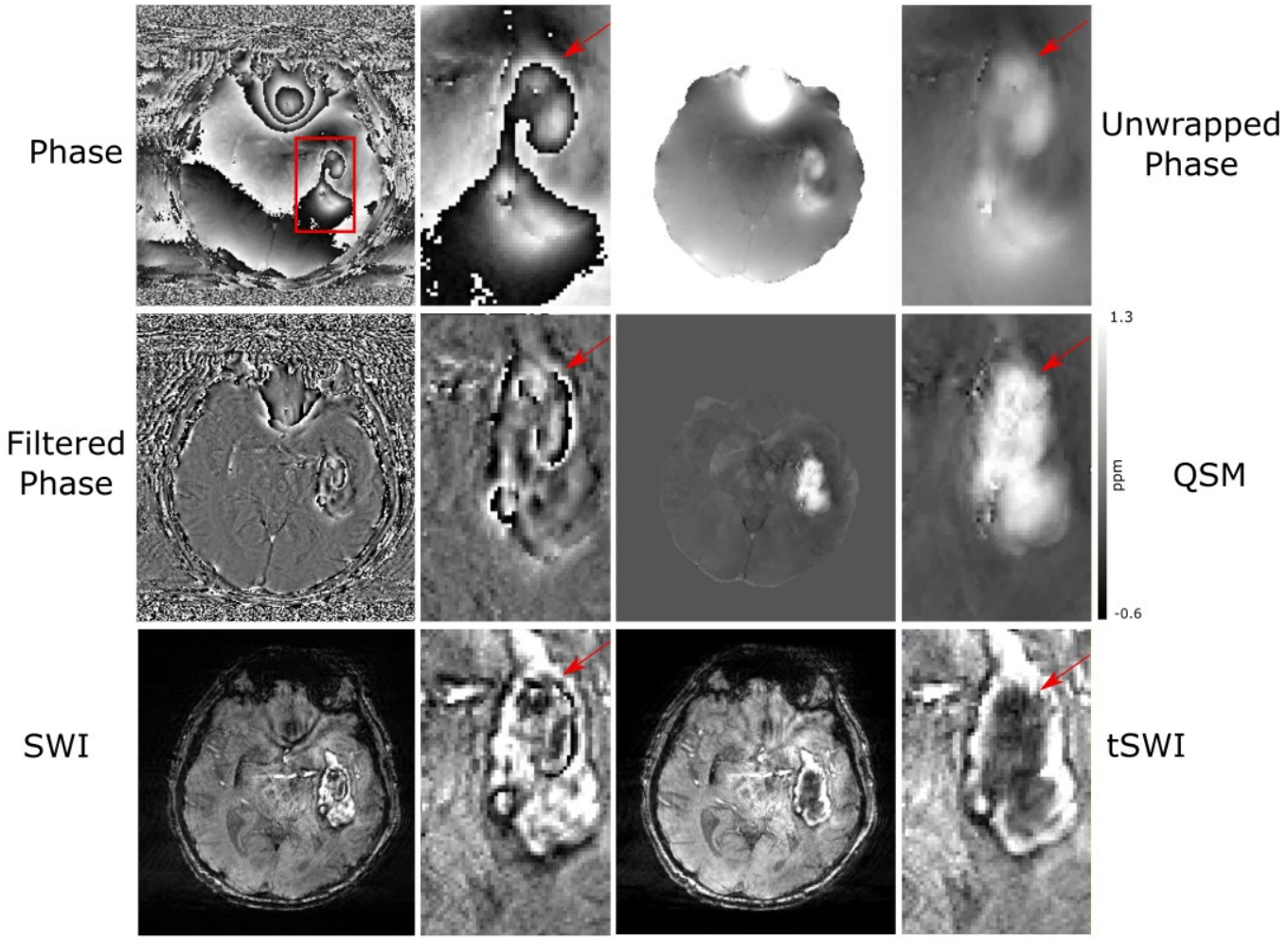

Figure 4.5: A comparison between phase, filtered phase, SWI, unwrapped phase, QSM and tSWI in a patient with Day 12 hemorrhage to show phase wrap artifacts are present in SWI for large hemorrhage which is removed in tSWI as shown by the red arrow.

Figure 4.6 shows a comparison of the signal intensity variations among SWI, tSWI and QSM of a hemorrhage patient. Mean signal intensity of tSWI ($r = -0.93$, $p<0.001$) in the hemorrhagic region shows a higher negative correlation with susceptibility values as compared to SWI ($r = -0.87$, $p<0.001$).

Figure 4.7 illustrates the time evolution of hemorrhage showing texture variation in phase, SWI and tSWI from day 4 to day 29 after symptom onset. Day 4 is hypointense in both methods with a blooming effect in SWI which was overcome in tSWI. On Day 12, a difference in texture is observed between the two methods due to phase wrap artifacts in SWI. Day 29 shows the tSWI and SWI as the hemorrhage further changed in nature and the difference in the images arises from the usage of susceptibility map and filtered phase to produce the weighted masks.

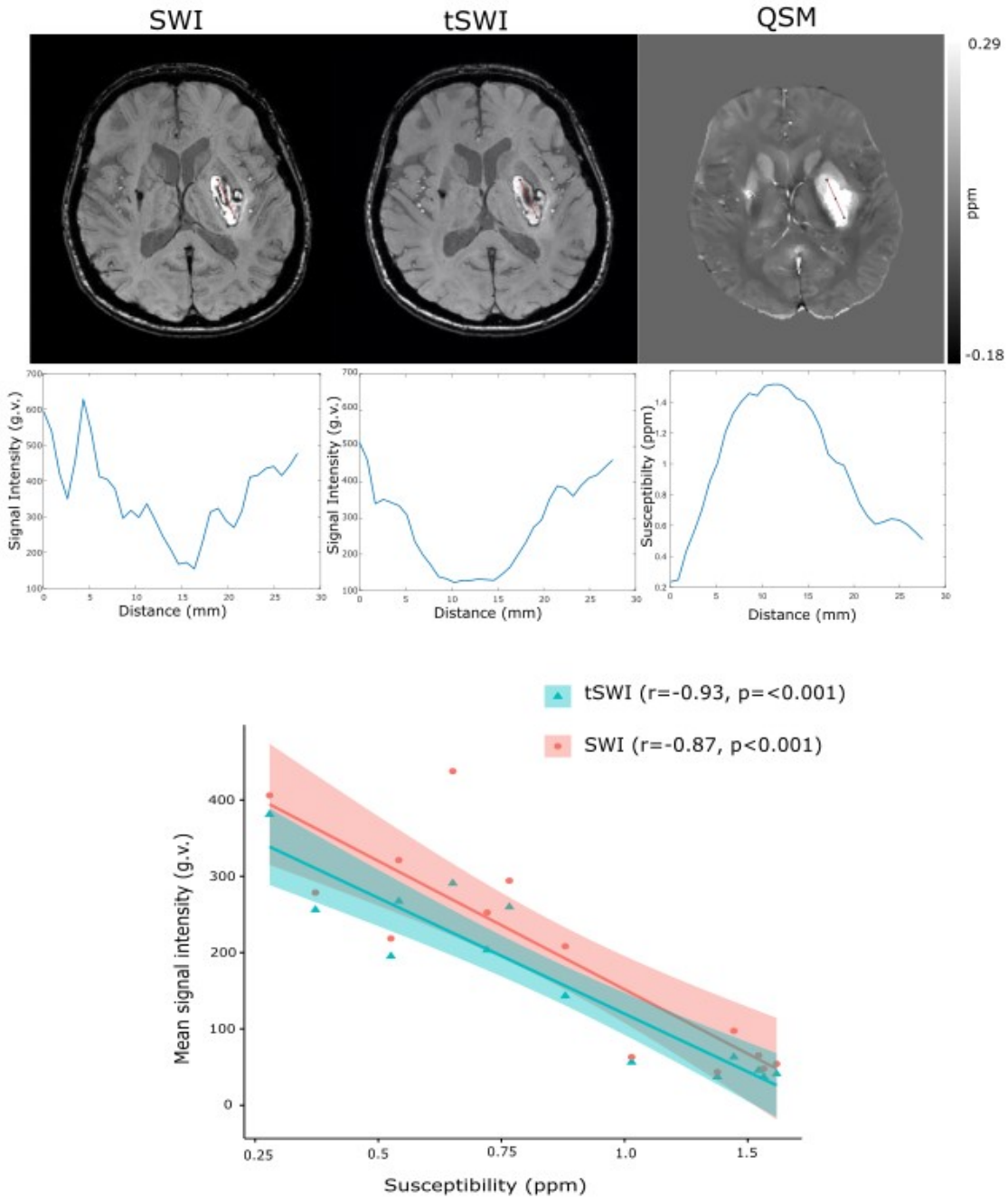

Figure 4.6: SWI, tSWI and QSM of a patient with Day 7 hemorrhage to compare the signal variation across the hemorrhage. Also shows the correlation of the mean signal intensities over the hemorrhagic region for all the patients from tSWI and SWI with susceptibility from QSM .

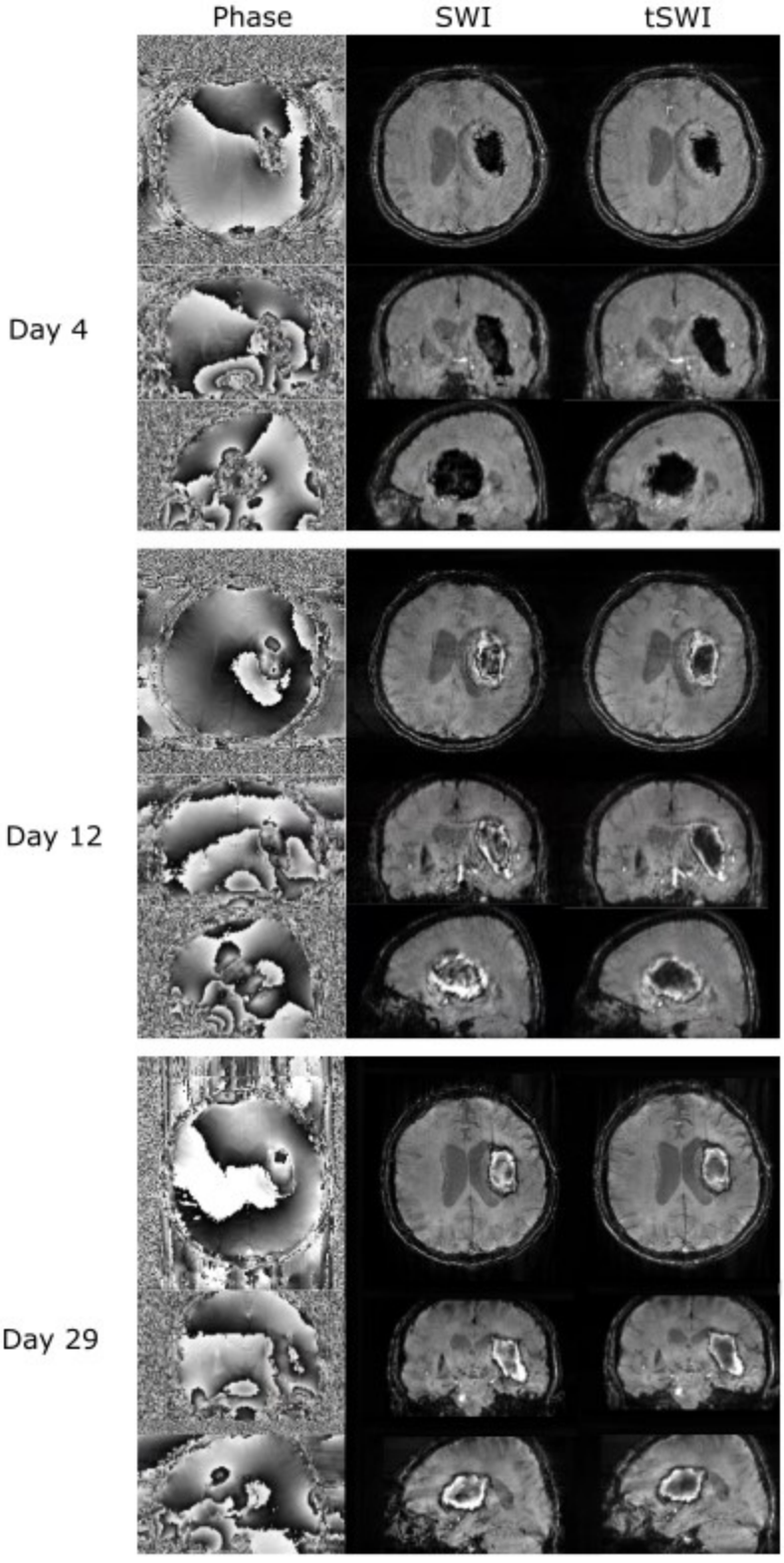
Phase
SWI
tSWI
Day 4
Day 12
Day 29

Figure 4.7: Time evolution of hemorrhage showing texture variation in Phase, SWI and tSWI from day 4 to day 29 after symptom onset. Day 4 is hypointense in both with increased area on SWI from blooming effect. As time elapses to Day 12, with change in the nature of the hemorrhage, the rim starts to turn hyperintense with the hypointense core showing variation between in SWI and tSWI due to phase artifacts affecting SWI. Day 29 also shows differences arising from use of different thresholded source images (filtered phase and true susceptibility).

4.4 Discussion

tSWI utilizes susceptibility maps to produce the thresholded mask, rather than the filtered phase images as used in SWI. Phase images come with well-known artifacts that manifest themselves more strongly in large susceptibility sources like hemorrhage that might suffer from blooming artifacts and incomplete phase unwrapping. Thus, conventional SWI may sometimes lead to unreliable shape, size and contrast for these strong susceptibility sources due to blooming as well as residual phase wraps which alter phase and gray values. As shown here, tSWI offers a complementary hemorrhage depiction compared to SWI by minimizing blooming and phase artifacts by using the actual susceptibility maps in the thresholding process.

The contrast in tSWI images takes advantage of features in both magnitude and susceptibility maps. While QSM can provide both quantitative measures and a qualitative depiction, tSWI uses a magnitude base enabling a more standard whole head qualitative depiction as well as enhanced

paramagnetic contrast from multiplication with a thresholded mask computed from QSM. It is well recognized that QSM is a powerful method to study iron-rich territories, but in anisotropic white matter, results can be somewhat artifactual, as well as difficulties in accuracy near brain edges. Thus, tSWI has the benefit of enhancing paramagnetic regions (veins, iron-rich territories like hemorrhage) while not affecting diamagnetic white matter. The result is a whole head image that is similar to images radiologists are used to viewing and yet enables improved contrast of paramagnetic regions without the added blooming from SWI. Thus, we recommend tSWI for qualitative depiction of hemorrhage, as well as QSM for quantitative susceptibility measurements of hemorrhage.

In terms of magnitude images versus tSWI, magnitude images can depict the boundary of hemorrhage sources. However, the value of tSWI is including an additional paramagnetic susceptibility contrast to the magnitude which enables both the depiction of other iron-containing structures (deep grey matter and veins) as well as addition of an accurate susceptibility contrast to the hemorrhagic region, without the added blooming artifacts from standard SWI. For example, the value of tSWI for depiction of other iron containing structures was recently shown for consistent visualization of Nigrosome 1,a region of substantia nigra [11] .

A major difference between using filtered phase and susceptibility maps to produce the masks is that the phase images are bound between 2π whereas the susceptibility values can rise to considerably higher values in the hemorrhagic region compared to healthy tissue. Hence, different thresholding parameters are required for these high susceptibility regions in tSWI.

The thresholds for tSWI were chosen to obtain wider use of the gray scale within hemorrhage and hence more effective texture visualization of the hemorrhages which have higher mean

susceptibility as compared to veins. If the upper threshold (χ_2) is selected to be 0.45 ppm as selected in previous work for non-hemorrhagic subjects [10,11], higher susceptibility values will have a weight of zero and hence observing any texture in the hemorrhage will not be possible. However, for visualization of hemorrhage texture, especially in the subacute and chronic stages, a variation in the pixel intensities corresponding to the susceptibility value of the hemorrhage is desirable. Hence, the upper threshold for this study was chosen to be 3.24 ppm which was the average maximum susceptibility of the hemorrhagic region for this study group.

SWI and tSWI also have a multiplicative factor for the thresholded image. The mean signal intensity in SWI and tSWI is expected to be negatively correlated with susceptibility due to T2* decay in substances with higher susceptibility. The correlation between mean susceptibility values and mean signal intensity in tSWI with different n values were observed to be similar and hence in this study n = 2 was used as in previous tSWI papers [10,11]. However, as a result of the higher susceptibility threshold of 3.24ppm instead of 0.45ppm, the optimal threshold for veins [10], some of the small veins with much lower susceptibility may not receive optimum enhancement. A larger n is optimal for veins when a higher threshold is chosen [10]. Thus, there are different requirements of hemorrhagic and non-hemorrhagic regions, requiring different upper thresholds. A combined tSWI was introduced using the standard upper threshold of 0.45 ppm for non-hemorrhagic regions and the increased threshold of 3.24 ppm in hemorrhagic regions. However, applying different thresholds within a single image can give rise to ambiguity in the diagnostic process, hence a means to supply tSWI at various upper thresholds would be helpful. Our recommendation would be two thresholds: the standard threshold (0.45 ppm) and an enhanced value on the order of 3 ppm, here 3.24 ppm was used since it was the mean maximum value found in our study. Alternatively,

a real-time manual control of the tSWI upper threshold could be implemented into the tSWI image display, enabling visualization with varying degrees of true susceptibility weighting.

Limitations of this study include difficulties at the edge of the brain with QSM reconstruction, which is an area of ongoing research [27,28]. Moreover, more complex tSWI reconstruction is required to produce artifact free QSM with high susceptibility sources. Also, a lack of gold standard makes the comparison and evaluation of tSWI difficult.

4.5 Conclusion

In hemorrhage, tSWI minimizes blooming effects and phase wrap artifacts observed in SWI. However, unlike SWI, tSWI requires an altered upper threshold for best hemorrhage depiction that differs from the standard value. tSWI can be used as a complementary technique for visualizing hemorrhages along with SWI.

4.6 Acknowledgement

Funding: This work was supported by the Canadian Institutes of Health Research (CIHR)[Grant number:PS 159568]

References:

[1] Haacke EM, Xu Y, Cheng Y-CN, Reichenbach JR. Susceptibility weighted imaging (SWI). Magn Reson Med 2004;52:612–8. https://doi.org/10.1002/mrm.20198.

[2] Liu S, Buch S, Chen Y, Choi H-S, Dai Y, Habib C, et al. Susceptibility-weighted imaging: current status and future directions. NMR Biomed 2017;30. https://doi.org/10.1002/nbm.3552.

[3] Barnes SRS, Haacke EM. Susceptibility-weighted imaging: clinical angiographic applications. Magn Reson Imaging Clin N Am 2009;17:47–61. https://doi.org/10.1016/j.mric.2008.12.002.

[4] Wang M, Dai Y, Han Y, Haacke EM, Dai J, Shi D. Susceptibility weighted imaging in detecting hemorrhage in acute cervical spinal cord injury. Magn Reson Imaging 2011;29:365–73. https://doi.org/10.1016/j.mri.2010.10.016.

[5] Haacke EM, Mittal S, Wu Z, Neelavalli J, Cheng Y-CN. Susceptibility-weighted imaging: technical aspects and clinical applications, part 1. AJNR Am J Neuroradiol 2009;30:19–30. https://doi.org/10.3174/ajnr.A1400.

[6] Rauscher A, Sedlacik J, Deistung A, Mentzel H-J, Reichenbach JR. Susceptibility weighted imaging: data acquisition, image reconstruction and clinical applications. Z Med Phys 2006;16:240–50. https://doi.org/10.1078/0939-3889-00322.

[7] Kullnig PE, Rauscher A, Witoszynskyj S, Deistung A, Kentouche K, Reichenbach JR, et al. Detection of multiple intracranial hemorrhages in a child with acute lymphocytic leukemia (ALL) by susceptibility weighted imaging (SWI). Radiol Case Rep 2007;2:135. https://doi.org/10.2484/rcr.v2i4.135.

[8] Liu C, Li W, Tong KA, Yeom KW, Kuzminski S. Susceptibility-weighted imaging and

quantitative susceptibility mapping in the brain. J Magn Reson Imaging 2015;42:23–41. https://doi.org/10.1002/jmri.24768.

[9] Xu Y, Haacke EM. The role of voxel aspect ratio in determining apparent vascular phase behavior in susceptibility weighted imaging. Magn Reson Imaging 2006;24:155–60. https://doi.org/10.1016/j.mri.2005.10.030.

[10] Liu S, Mok K, Neelavalli J, Cheng Y-CN, Tang J, Ye Y, et al. Improved MR venography using quantitative susceptibility-weighted imaging. J Magn Reson Imaging JMRI 2014;40:698–708. https://doi.org/10.1002/jmri.24413.

[11] Cheng Z, He N, Huang P, Li Y, Tang R, Sethi SK, et al. Imaging the Nigrosome 1 in the substantia nigra using susceptibility weighted imaging and quantitative susceptibility mapping: An application to Parkinson's disease. NeuroImage Clin 2020;25:102103. https://doi.org/10.1016/j.nicl.2019.102103.

[12] He N, Sethi SK, Zhang C, Li Y, Chen Y, Sun B, et al. Visualizing the lateral habenula using susceptibility weighted imaging and quantitative susceptibility mapping. Magn Reson Imaging 2020;65:55–61. https://doi.org/10.1016/j.mri.2019.09.005.

[13] Reichenbach JR, Schweser F, Serres B, Deistung A. Quantitative Susceptibility Mapping: Concepts and Applications. Clin Neuroradiol 2015;25 Suppl 2:225–30. https://doi.org/10.1007/s00062-015-0432-9.

[14] Wang S, Lou M, Liu T, Cui D, Chen X, Wang Y. Hematoma volume measurement in gradient echo MRI using quantitative susceptibility mapping. Stroke 2013;44:2315–7. https://doi.org/10.1161/STROKEAHA.113.001638.

[15] Chang S, Zhang J, Liu T, Tsiouris AJ, Shou J, Nguyen T, et al. Quantitative Susceptibility Mapping of Intracerebral Hemorrhages at Various Stages. J Magn Reson Imaging JMRI

2016;44:420–5. https://doi.org/10.1002/jmri.25143.

[16] Sun H, Kate M, Gioia LC, Emery DJ, Butcher K, Wilman AH. Quantitative susceptibility mapping using a superposed dipole inversion method: Application to intracranial hemorrhage. Magn Reson Med 2016;76:781–91. https://doi.org/10.1002/mrm.25919.

[17] Sun H, Klahr AC, Kate M, Gioia LC, Emery DJ, Butcher KS, et al. Quantitative Susceptibility Mapping for Following Intracranial Hemorrhage. Radiology 2018;288:830–9. https://doi.org/10.1148/radiol.2018171918.

[18] De A, Sun H, Emery DJ, Butcher KS, Wilman AH. Rapid quantitative susceptibility mapping of intracerebral hemorrhage. J Magn Reson Imaging JMRI 2020;51:712–8. https://doi.org/10.1002/jmri.26850.

[19] Keep RF, Hua Y, Xi G. Intracerebral haemorrhage: mechanisms of injury and therapeutic targets. Lancet Neurol 2012;11:720–31. https://doi.org/10.1016/S1474-4422(12)70104-7.

[20] Bradley WG. MR appearance of hemorrhage in the brain. Radiology 1993;189:15–26. https://doi.org/10.1148/radiology.189.1.8372185.

[21] Wagner KR, Sharp FR, Ardizzone TD, Lu A, Clark JF. Heme and iron metabolism: role in cerebral hemorrhage. J Cereb Blood Flow Metab Off J Int Soc Cereb Blood Flow Metab 2003;23:629–52. https://doi.org/10.1097/01.WCB.0000073905.87928.6D.

[22] Chen W, Zhu W, Kovanlikaya I, Kovanlikaya A, Liu T, Wang S, et al. Intracranial calcifications and hemorrhages: characterization with quantitative susceptibility mapping. Radiology 2014;270:496–505. https://doi.org/10.1148/radiol.13122640.

[23] Smith SM. Fast robust automated brain extraction. Hum Brain Mapp 2002;17:143–55. https://doi.org/10.1002/hbm.10062.

[24] Abdul-Rahman HS, Gdeisat MA, Burton DR, Lalor MJ, Lilley F, Moore CJ. Fast and robust

three-dimensional best path phase unwrapping algorithm. Appl Opt 2007;46:6623–35. https://doi.org/10.1364/ao.46.006623.

[25] Zhou D, Liu T, Spincemaille P, Wang Y. Background field removal by solving the Laplacian boundary value problem. NMR Biomed 2014;27:312–9. https://doi.org/10.1002/nbm.3064.

[26] Bilgic B, Pfefferbaum A, Rohlfing T, Sullivan EV, Adalsteinsson E. MRI estimates of brain iron concentration in normal aging using quantitative susceptibility mapping. NeuroImage 2012;59:2625–35. https://doi.org/10.1016/j.neuroimage.2011.08.077.

[27] Wei H, Cao S, Zhang Y, Guan X, Yan F, Yeom KW, et al. Learning-based single-step quantitative susceptibility mapping reconstruction without brain extraction. NeuroImage 2019;202:116064. https://doi.org/10.1016/j.neuroimage.2019.116064.

[28] Sun H, Ma Y, MacDonald ME, Pike GB. Whole head quantitative susceptibility mapping using a least-norm direct dipole inversion method. NeuroImage 2018;179:166–75. https://doi.org/10.1016/j.neuroimage.2018.06.036.

Chapter 5

Simultaneous Time-of-Flight (TOF) MR Angiography and Quantitative Susceptibility Mapping (QSM) without compromising TOF features*

Abstract

Purpose: To develop a TOF-QSM sequence with key features of modern 3D TOF acquisitions.

*A version of this chapter is under review in MRM: A. De, J. Grenier and A. H. Wilman, "Simultaneous Time-of-Flight (TOF) MR Angiography and Quantitative Susceptibility Mapping (QSM) without compromising TOF features", Magn. Reson. Med.

Methods: A triple-echo 3D TOF-QSM sequence was developed and implemented at 3T. The sequence maintained key TOF features, then included additional echoes for susceptibility weighted imaging, QSM and R2* mapping. The effects of ramped RF, resolution, flip angle, venous saturation and multiple overlapping thin slab acquisition (MOTSA) were studied on QSM. Six volunteers were scanned with the developed sequence, conventional TOF-MRA and conventional SWI. Quantitative comparison of the CNRs of the arteries and veins, and susceptibility values was performed.

Results: The ramped RF created an inherent phase variation in the raw phase. A generic correction factor was computed to remove the phase variation to obtain QSM without artifacts. Maintaining standard TOF features led to compromises in SNR for QSM and SWI, arising from the use of MOTSA rather than one large 3D slab, as well as higher TOF spatial resolution, increased TOF background suppression due to larger flip angles and reduced venous signal from venous saturation. Nevertheless, maintaining the TOF features enabled high quality TOF combined with SWI and QSM. Moreover, no statistically significant difference was observed between the developed and standard independent TOF and QSM methods for brain susceptibility values, arterial CNR on TOF-MRA and venous CNR on SWI. R2* was also produced from the sequence.

Conclusion: QSM may be performed from a multi-echo sequence that maintains key TOF features thus enabling simultaneous TOF-MRA, SWI, QSM and R2* map computation.

5.1 Introduction

Time-of-Flight (TOF) MR angiography (MRA) provides a means to examine arterial lumen without contrast agents [1]–[3]. Susceptibility Weighted Imaging (SWI) offers means to study veins, lesions, hematoma, and brain iron changes [4]–[8]. SWI has a wide range of clinical applications [9]–[12]. Quantitative Susceptibility Mapping (QSM) and transverse relaxation rate (R2*) mapping are quantitative MRI methods that are sensitive to brain iron and myelin changes [13]–[15]. In particular, these methods facilitate quantitative study of iron changes in healthy subjects, stroke, and various neurodegenerative diseases [6], [16]–[20]. QSM can be computed from the same sequence as SWI.

Thus TOF-MRA as well as SWI, R2* and QSM are methods clinically useful to study neurological diseases. All of these methods typically use a 3D gradient-recalled echo (GRE) sequence with single or multiple echoes. TOF-MRA is usually acquired from a separate 3D GRE scan than SWI and R2*/QSM, owing to the fact that it requires unique parameter settings. Since these three protocols are commonly used and clinically provide different information, it would be beneficial to obtain all the information simultaneously from a single sequence. This can ideally reduce total scan time and artifacts caused by misregistration between sequences.

Previous works have examined combining TOF with an SWI or QSM sequence but either some of the TOF features have been compromised or QSM has not been computed. Some previous papers combining TOF and SWI as dual echo did not compute QSM [21]. Whereas one work that computed QSM did not examine the effect of suboptimal TOF parameters [22]. Dual echo sequences with k-space reordering schemes have also demonstrated MRA and SWI [23]–[26].

Other works have examined a multi-echo T2* weighted sequence for MRA [27], [28] and some have demonstrated the possibility of studying arteries and veins simultaneously using multi-echo sequences by combining angiography and T2* weighted imaging [26], [29]–[32] without incorporating typical TOF-MRA sequence parameters. Along with studying arteries and veins, a previous paper has also examined cerebral microbleeds with TOF-MRA and combined SWI from a multi-echo GRE sequence [33]. Thus, none of these works have studied the effect of the TOF parameters on both phase and QSM.

More specifically, modern implementations of 3D TOF-MRA in the brain use a series of parameters very different from SWI/QSM requirements beyond just the echo time choice. First, in order to suppress static background signals, TOF-MRA requires a higher flip angle than that used in SWI/QSM [34]. Second, the RF excitation in 3D TOF is typically a ramped RF pulse to maximize vessel contrast, particularly for slower flowing vessels [35], [36], as opposed to a flat RF profile used in SWI/QSM. Third, to further improve inflow, 3D TOF is typically performed with multiple overlapping thin slab acquisitions (MOTSA), while SWI/QSM methods tend to use one large slab. The number of per slab also strongly affects the available SNR, since SNR depends on $\sqrt{number\ of\ slices}$ for static tissues. This can also cause misregistration of position and inhomogeneity in signal intensity between adjacent slabs. Fourth, and finally, 3D TOF utilizes venous saturation for unambiguous arterial depiction, while SWI/QSM avoid this feature to maintain venous signal.

This study develops a 3D TOF-QSM sequence with the core features of modern 3D TOF acquisitions such as venous saturation, ramped RF and MOTSA. The effects of these TOF parameters on phase and QSM are examined and then compromises are considered between ideal

TOF parameters and the requirements of SWI/QSM. Through testing in healthy subjects in brain, a combined TOF, SWI, QSM and R2* approach is determined without sacrificing TOF quality.

5.2 Methods

5.2.1 Data acquisition

Figure 5.1 demonstrates the triple-echo 3D GRE sequence used for TOF-QSM that was implemented at 3T (Prisma, Siemens Healthcare, Erlangen, Germany) using the vendor specific development environment IDEA (version VE11C, Siemens Healthcare). Key TOF features include ramped RF excitation preceded by a venous saturation pulse and MOTSA.

To study the effect of flip angle and resolution, whole brain acquisitions used three variations of the developed sequence either varying the ramped RF excitation angle or the spatial resolution:

(I) Acquired resolution: 0.52X0.52X0.75mm^3 without interpolation; ramped profile RF excitation with flip angle 18^0 (14.8^0 and 21.2^0); acquisition time 8.43 min.

(II) Same resolution as (I) with flip angle 25^0 (20.6^0 to 29.4^0); acquisition time 8.43min.

(III) Same flip angle as (I) at a lower acquired resolution 0.76X0.76X0.80mm^3 without interpolation; ; acquisition time 5.33min.

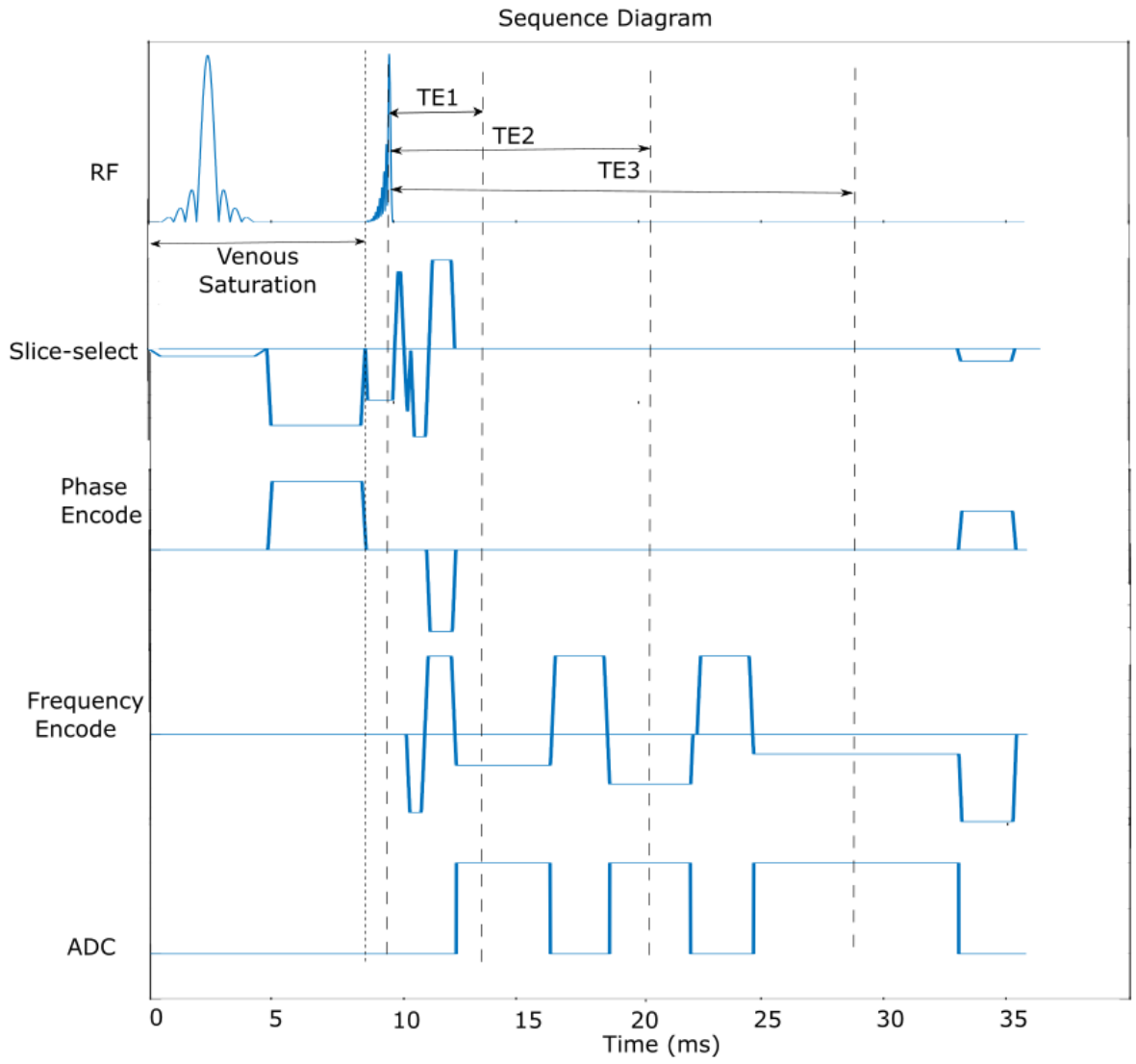

Figure 5.1: The sequence diagram of the developed TOF-QSM sequence. To minimize the first echo time for TOF imaging, the first echo is asymmetric, and the sequence is flow compensated in readout and slice-select direction for the first echo.

Constant parameters for all sequences were TE1/TE2/TE3/TR 3.9/10.6/19.0/36.0 ms; 5 slabs (30 slices each) with 20% overlap for MOTSA; superior venous saturation with gradient spoiling; and flow compensated in readout and slice-select direction for the first echo with GRAPPA parallel imaging with acceleration factor of 2 along the primary phase-encoding direction. In-plane two-fold interpolation was also reconstructed for the first echo for TOF-MRA.

In addition, one volunteer was scanned with and without the venous saturation using parameters from protocol (I).

The standard TOF sequence had the following parameters: TE/TR = 3.43ms/21ms; acquired resolution: 0.52x0.52x0.75 mm^3; flip angle 18^0 (14.8^0 to 21.2^0); 5 slabs (30 slices each) with 20% overlapping for MOTSA; venous saturation; acquisition time of 5.21min; first order gradient moment nulling and GRAPPA with acceleration factor of 2 along the primary phase-encoding direction. In-plane two-fold interpolation was performed to obtain the TOF-MRA.

The standard SWI sequence had the following parameters: TE/TR = 20/27 ms; resolution 0.9x0.9x1.5mm^3; flip angle 15^0, 80 slices; acquisition time 4.54 minutes; first order gradient moment nulling and GRAPPA with acceleration factor of 2 along the primary phase-encoding direction.

Six volunteers were studied with standard TOF, standard SWI and the proposed TOF-QSM sequence with protocol (I) covering the whole brain in a 3D axial-oblique acquisition. All volunteer data was acquired with a 64-channel head receive coil. This study was approved by the institutional ethics board and all subjects gave informed consent.

5.2.2 Image Reconstruction

Beginning with the raw phase and magnitude images, all further processing steps were performed in MATLAB R2019a (Mathworks, Natick, MA). The overlapped MOTSA slabs were concatenated by removing three slices in the overlap region of each slab. SWI and QSM were reconstructed from the third echo (TE 19ms) without any interpolation as done in the standard methods. SWI images were generated by the standard method [4] of multiplying the magnitude by four times of the filtered phase as follows: $SWI = Magnitude * Filtered\ Phase\ Mask^4$

The ramped RF creates an inherent phase variation across the slab which can be observed in the raw phase used for QSM reconstruction. To correct for this, phase variation across the slab at the center of the slices was computed using a uniform phantom by subtracting from the unwrapped phases with and without the ramped RF pulse. This phase variation was then filtered using a moving average filter to reduce the variation from the noise and produce a generic correction factor which was applied to all the phase datasets.

QSM computation steps included forming a binary volume brain mask with Brain Extraction Tool (BET) [37], phase unwrapping with phase region expanding labeller for unwrapping discrete estimates (PRELUDE) [38], phase correction to remove the ramp RF phase variation and background removal with VSHARP [39], [40] followed by dipole inversion using MEDI [41].

5.2.3 Image Analysis

Using rigid registration, all the MRA, SWI and QSM images were registered using SPM-12(Statistical Parametric Mapping; The Wellcome Centre for Human Neuroimaging, London, UK) software package running under MATLAB R2019a. For quantitative analysis, ROIs were drawn using ImageJ. For quantitative analysis of the MR angiograms, contrast to noise ratio (CNR) between artery and background tissue was measured in three different positions in the FOV. Signal intensities were measured on source images from blood vessels, adjacent tissue, and background air outside the brain. The three locations were: the internal carotid artery (Region 1A), the middle cerebral artery (Region 2A) and a side branch of the anterior cerebral artery(Region 3A) about 30 mm from the second region. For quantitative analysis of SWI, similar CNRs were computed from three venous regions: the straight sinus (Region 2V), a venous region 15mm inferior on a vein branching from the straight sinus (Region 1V), and about 15mm superior to the straight sinus region , in a cortical vein (Region 3V). All measures were repeated twice with the mean CNR computed. For QSM, susceptibility values from brain structures were compared.

Statistical analysis was conducted in R (version 4.1.1, 64 bit). Wilcoxon signed-rank test was used to compare the CNRs, and susceptibility values obtained from the proposed and standard sequences.

5.3 Results

Figure 5.2(a) shows the phase variation pattern caused by the ramped RF. This phase offset computed from phantom was used as the correction factor. Figure 5.2(b) shows the effect of ramped RF on QSM reconstruction, including the variation on unwrapped phase and local field that is removed after correcting for the phase variation induced by the ramped RF pulse.

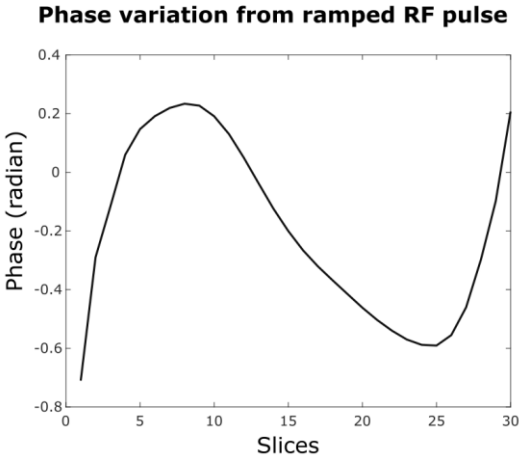

Figure 5.2 (a): The variable phase offset caused across the slab due to the ramped RF. This was used as the correction factor for generating unwrapped phase without the phase variation from the ramped RF.

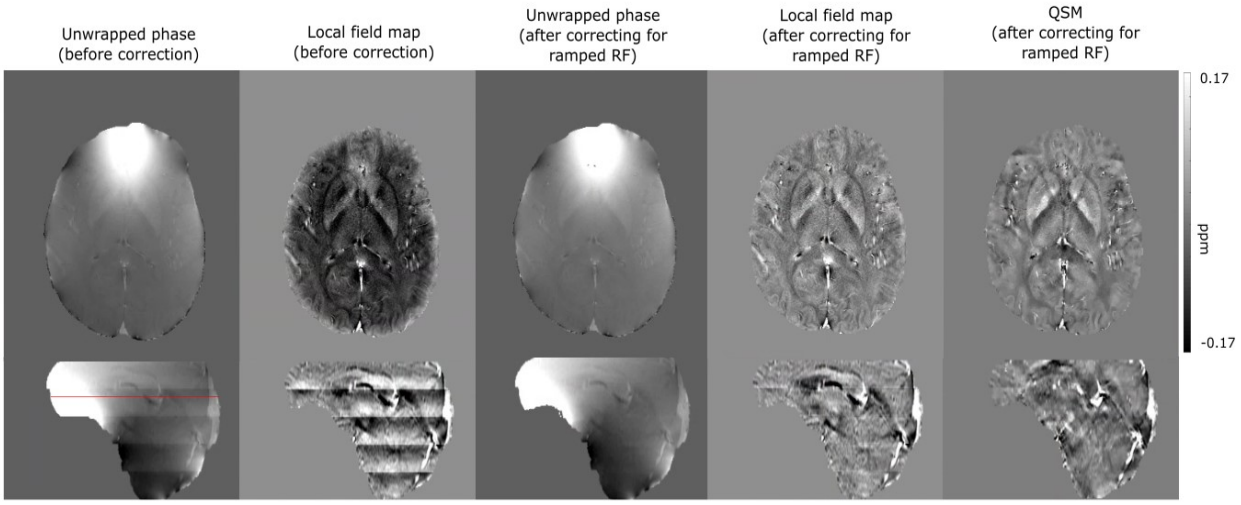

Figure 5.2 (b): The effect of ramped profile RF excitation on unwrapped phase and local field and then the corrected unwrapped phase which results in corrected local field and QSM (The red line on the sagittal represents the position of the axial slice).

Figure 5.3 shows the effect of flip angle and resolution on TOF-MRA from the first echo. Figure 5.4 demonstrates the effect of flip angle, resolution and resulting SNR on SWI and QSM from the third echo. The triple-echo sequence has a longer TR than standard TOF-MRA hence both the standard TOF flip angle of 18^0 (using protocol I) as shown in Figure 5.3(A) and Figure 5.4(B) and an increased flip angle of 25^0 (using protocol II) as shown in Figure 5.3(B) and Figure 5.4(B) were tested. In Figure 5.3, the increase in flip angle further suppresses the background signal to levels similar to standard TOF; however, this causes background tissue SNR to decrease which leads to artifacts in QSM in Figure 5.4(B). Reducing the resolution (using protocol III), reduces the visibility of small vessels in TOF-MRA as shown in Figure 5.3(C); however, the SWI and QSM quality improved due to higher SNR as shown in Figure 5.4(C). The TOF-QSM sequence (using protocol I) with resolution similar to standard TOF had similar depiction of the smaller arteries as

the standard TOF, and the QSM from the third echo, though noisier than the low resolution version, was of acceptable quality (Figure 5.3(A),5.4(A)). Hence, the TOF-QSM sequence with a flip angle of 18^0 and resolution of $0.52\times0.52\times0.75mm^3$ (protocol I) was used for quantitative comparison with standard methods.

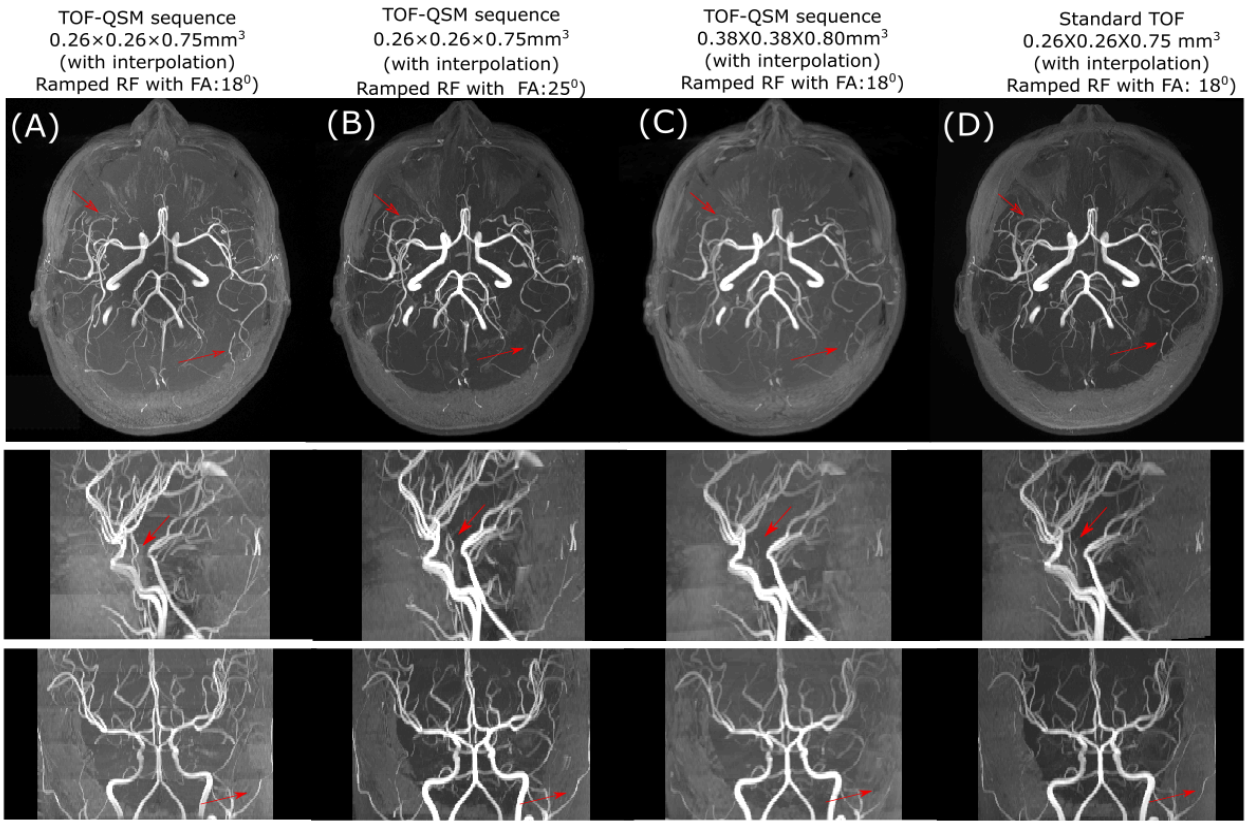

Figure 5.3: Maximum Intensity Projections (MIP) from the first echo of (A)TOF-QSM sequence with resolution 0.26X0.26X0.75mm³ and flip angle 18⁰ (protocol I), (B) TOF-QSM sequence with resolution 0.26X0.26X0.75mm³ and flip angle 25⁰ (protocol II), (C) TOF-QSM sequence with resolution 0.38X0.38X0.80mm³ and flip angle 18⁰ (protocol III) and (D) standard TOF sequence. The red arrows demonstrate small arteries that are not clearly visible with lower resolution parameters.

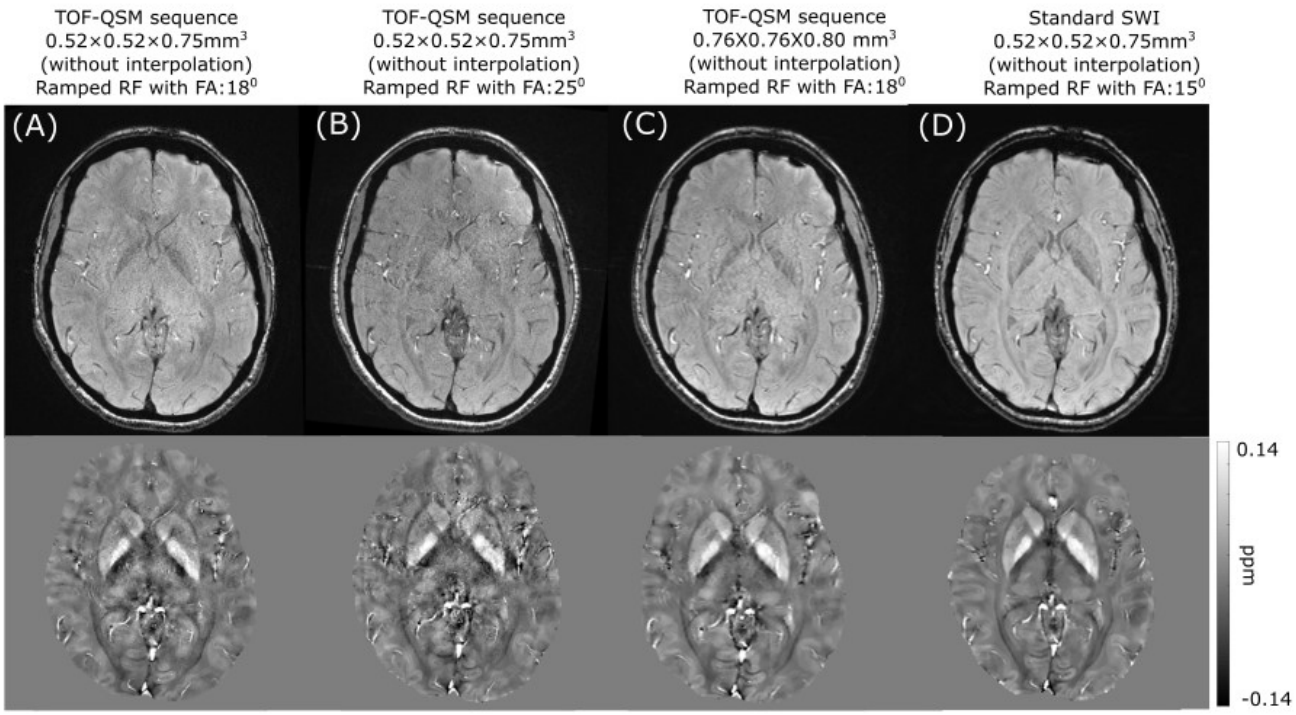

Figure 5.4: SWI and QSM from (A) TOF-QSM sequence with resolution 0.52X0.52X0.75mm³ and flip angle 18⁰ (protocol I), (B) TOF-QSM sequence with resolution 0.52X0.52X0.75mm³ and flip angle 25⁰ (protocol II), (C)TOF-QSM sequence with resolution 0.76X0.76X0.80mm³ and flip angle 18⁰ (protocol III) and (D) standard SWI sequence.

Table 5.1 shows the mean and standard deviations of the CNR of the arteries and veins from all subjects. No statistically significant difference was observed between CNRs of the standard and the proposed methods. Table 5.2 shows the mean and standard deviations of the susceptibility values of different brain structures which show similar results between methods.

Table 5.1. CNR values measured at three different slice locations on MRA and MRV acquired from standard single echo TOF, SWI and TOF-QSM sequence.

	Region 1A		Region 2A		Region 3A	
Artery to tissue	Standard TOF	TOF-QSM	Standard TOF	TOF-QSM	Standard TOF	TOF-QSM
CNR	456 ±145	408 ± 111	521± 68	507 ± 87	279 ± 108	282 ± 99
	Region 1V		Region 2V		Region 3V	
Vein to tissue	Standard SWI	TOF-QSM	Standard SWI	TOF-QSM	Standard SWI	TOF-QSM
CNR	105 ± 29	92 ± 17	160±52	105 ± 10	119 ± 40	89 ± 26

Table 5.2. Comparison of susceptibility values (mean± standard deviation) between standard single echo SWI and TOF-QSM sequence.

Brain structures	Standard sequence (ppm)	TOF-QSM sequence (ppm)[a]

Globus Pallidus (left)	0.134 ±0.025	0.131± 0.024
Globus Pallidus(right)	0.130± 0.015	0.133±0.021
Putamen (left)	0.035± 0.006	0.032± 0.011
Putamen (right)	0.022± 0.015	0.025± 0.013
Caudate Nucleus (left)	0.036± 0.014	0.038± 0.011
Caudate Nucleus (right)	0.040± 0.014	0.049± 0.012
Internal Capsule (left)	-0.057± 0.016	-0.065± 0.018
Internal Capsule(right)	-0.061± 0.015	-0.066± 0.016
Dentate Nucleus(left)	0.111± 0.024	0.107± 0.022
Dentate Nucleus(right)	0.109± 0.037	0.100± 0.026

[a] Volunteers scanned using protocol I

Figure 5.5 shows the effect of venous saturation on TOF-MRA and Figure 5.6 on SWI and QSM. Without venous saturation, the veins can be observed in the MIP of TOF-MRA along with the arteries. With venous saturation, the veins are suppressed on magnitude images, but adequate phase signal remains to observe the sagittal sinus on QSM.

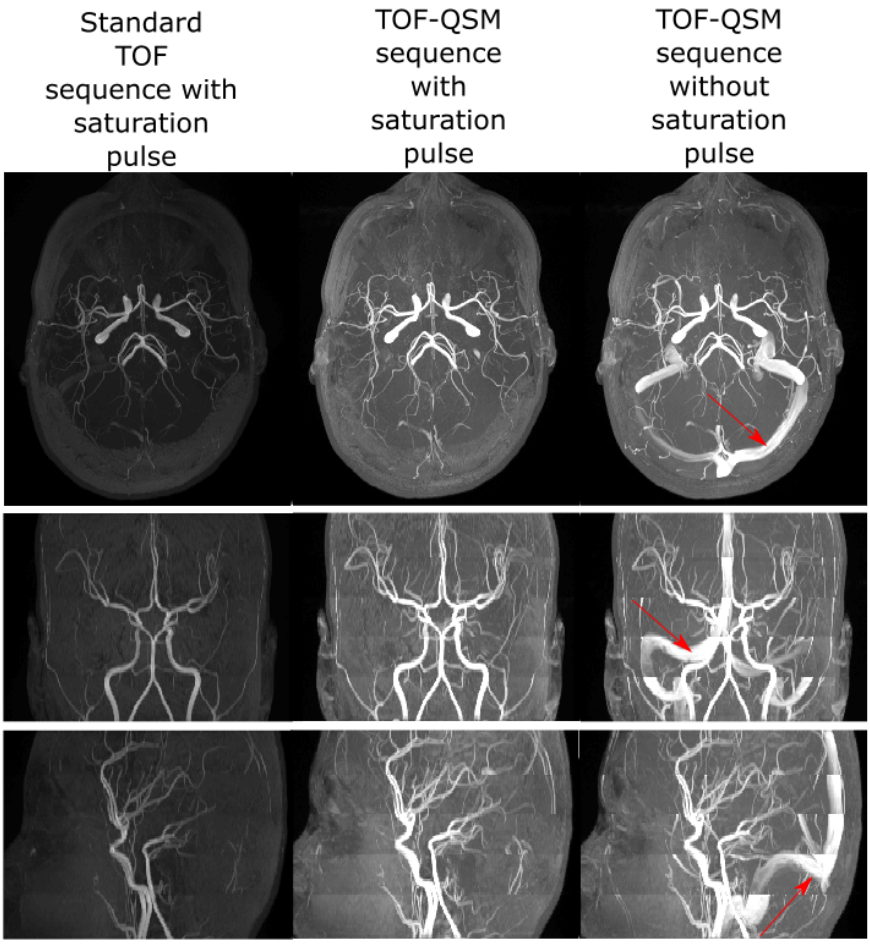

Figure 5.5: The effect of venous saturation pulse on MRA. Visible veins without the saturation pulse are shown with red arrows.

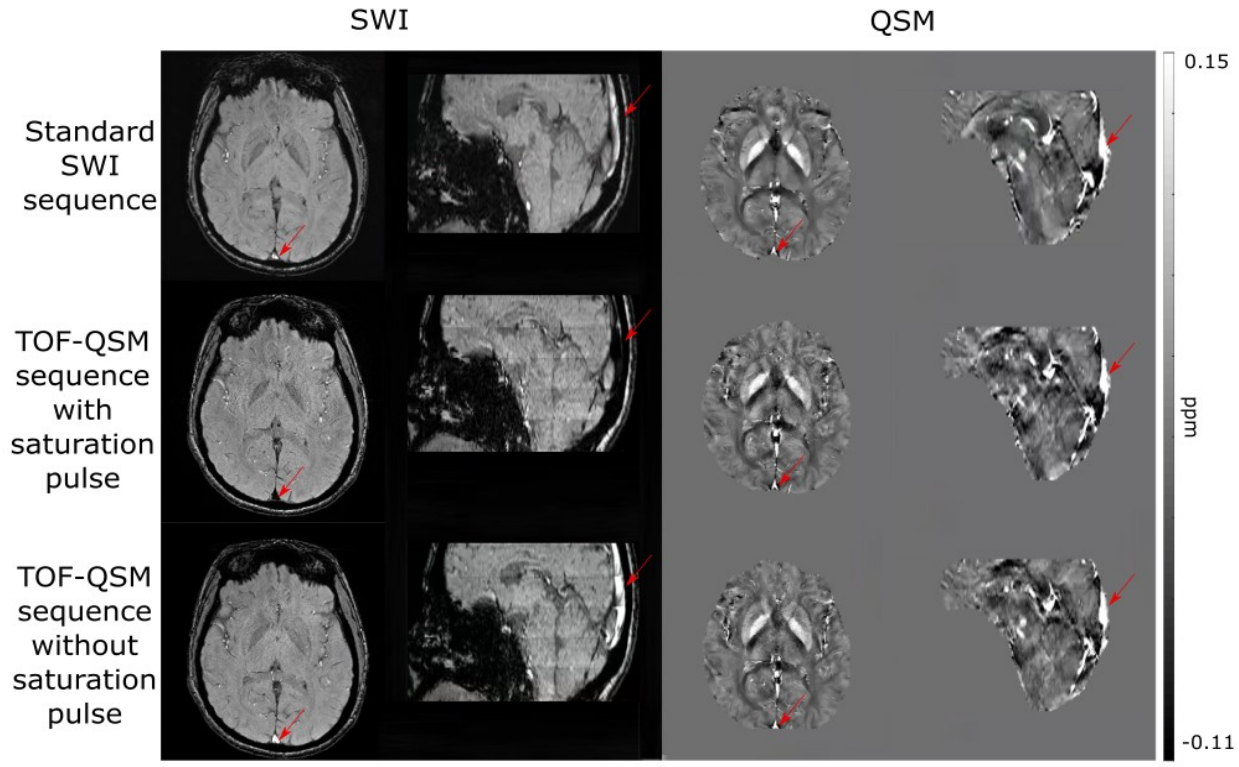

Figure 5.6: The effect of venous saturation pulse on veins in SWI and QSM. The sagittal sinus is shown with red arrows where reduction in signal intensity is observed in SWI due to addition of venous saturation pulse.

Figure 5.7 shows MRA, SWI, mIP from SWI, QSM and R2* from the triple-echo sequence for a volunteer. The MRA is computed from the first echo; SWI and QSM are computed from the third echo and R2* is computed by curve fitting across the three echoes.

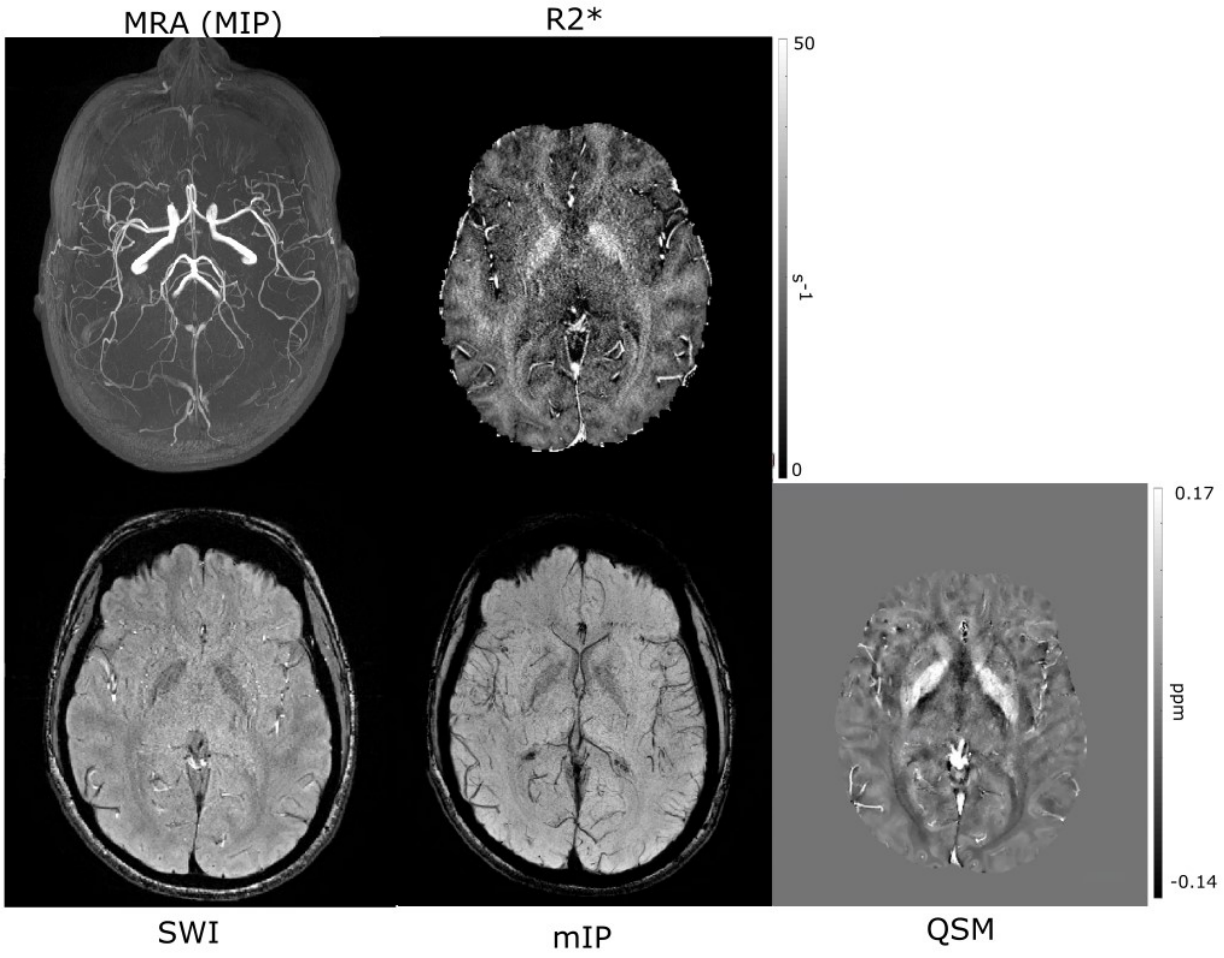

Figure 5.7: Images from the triple echo TOF-QSM sequence from one volunteer: TOF-MRA (MIP from first echo through 126 slices), R2* (from all echoes), SWI, minimum intensity projection (mIP) through 14 slices, and QSM (from third echo).

5.4 Discussion

A modified triple-echo sequence has been introduced to allow TOF-MRA, SWI, R2* and QSM while maintaining key TOF features of ramped RF excitation, venous saturation and MOTSA acquisition. This acquisition prioritizes TOF-MRA but comes at some SNR cost to SWI/QSM and requires an extra phase correction step for the ramped RF pulse.

In the TOF sequence, the ramped RF excitation is known to provide a better depiction of arteries [35], [36] but causes a phase variation across the slab. The filtered phase in SWI reduces this phase variation and hence no extra step is required in SWI computation. QSM utilizes information from the raw phase and hence this phase variation from the ramped RF pulse was corrected after the phase unwrapping step of the QSM computation to enable correct computation of the local field and susceptibility map.

There is a compromise between ideal TOF background suppression and ideal signal background level for SWI and QSM. A flip angle of 25^0 with TR of 36 ms, provided a higher artery-tissue contrast as compared to the standard TOF sequence; however, this led to reduced SNR for SWI and QSM. More typically QSM (and SWI) choose a flip angle near the Ernst angle to provide adequate tissue signal intensity. The flip angle was chosen to be 18^0 which is slightly larger than the Ernst angle of brain tissue (Ernst angle of GM: 13.3^0 and WM: 16.7^0 for TR = 36ms) to achieve both an appropriate CNR for the arteries in the TOF-MRA and adequate tissue SNR for SWI/QSM. Thus, while all features of TOF-MRA remain, the TOF background suppression is reduced slightly to improve SWI and QSM. However, there was no impact on the visibility of smaller arteries and

no significant difference was observed between the standard and proposed methods for arterial CNR.

TOF-MRA requires high resolution to depict small arteries; however, this small voxel size can lead to reduction in SNR for SWI and QSM. Moreover, implementation of MOTSA further decreases the tissue SNR of the proposed sequence by using 5 thin slabs, rather than one large slab as used in QSM, thus losing out on slice SNR averaging effects, proportional to . In addition, MOTSA also tends to reduce the vessel continuity at slab boundaries due to venetian blind artifacts or motion [42]–[44].

Limitations of this study include the sequence not having flow compensation in the phase-encode direction and flow compensation gradient being present before the first echo which caused some flow artifacts in SWI and QSM. However, it is possible to overcome these artifacts by including flow compensation gradients before the third echo [21]. Secondly, multi-echo sequences are more sensitive to motion; thus, has increased noise. Further the high resolution and MOTSA decreases SNR of the brain. Also, venous saturation decreases SNR in veins which can cause streaking artifacts on QSM. Using optimized QSM algorithms with better performance for veins and low SNR [45], [46] can overcome these reconstruction limitations.

5.5 Conclusion

The proposed sequence with the TOF features provided TOF-MRA and SWI with similar CNRs to standard methods. The susceptibility values between the proposed and standard methods had no

significant susceptibility variation as well. Thus, this sequence is able to provide similar TOF-MRA to standard TOF methods while enabling additions of SWI, R2* and QSM.

5.6 Acknowledgement

We thank Peter Seres for assistance with data collection. This work was supported by the Canadian Institutes of Health Research (CIHR).

References

[1] M. J. Graves, "Magnetic resonance angiography," Br. J. Radiol., vol. 70, pp. 6–28, Jan. 1997, doi: 10.1259/bjr.70.829.9059290.

[2] F. W. Wehrli, A. Shimakawa, G. T. Gullberg, and J. R. MacFall, "Time-of-flight MR flow imaging: selective saturation recovery with gradient refocusing," Radiology, vol. 160, no. 3, pp. 781–785, Sep. 1986, doi: 10.1148/radiology.160.3.3526407.

[3] C. Lévy et al., "Carotid and vertebral artery dissections: three-dimensional time-of-flight MR angiography and MR imaging versus conventional angiography," Radiology, vol. 190, no. 1, pp. 97–103, Jan. 1994, doi: 10.1148/radiology.190.1.8259436.

[4] E. M. Haacke, Y. Xu, Y.-C. N. Cheng, and J. R. Reichenbach, "Susceptibility weighted imaging (SWI)," Magn. Reson. Med., vol. 52, no. 3, pp. 612–618, Sep. 2004, doi: 10.1002/mrm.20198.

[5] S. Liu et al., "Susceptibility-weighted imaging: current status and future directions," NMR Biomed., vol. 30, no. 4, Apr. 2017, doi: 10.1002/nbm.3552.

[6] S. Wang, M. Lou, T. Liu, D. Cui, X. Chen, and Y. Wang, “Hematoma volume measurement in gradient echo MRI using quantitative susceptibility mapping,” Stroke, vol. 44, no. 8, pp. 2315–2317, Aug. 2013, doi: 10.1161/STROKEAHA.113.001638.

[7] A. M. Halefoglu and D. M. Yousem, “Susceptibility weighted imaging: Clinical applications and future directions,” World J. Radiol., vol. 10, no. 4, pp. 30–45, Apr. 2018, doi: 10.4329/wjr.v10.i4.30.

[8] C. Liu, H. Wei, N.-J. Gong, M. Cronin, R. Dibb, and K. Decker, “Quantitative Susceptibility Mapping: Contrast Mechanisms and Clinical Applications,” Tomogr. Ann Arbor Mich, vol. 1, no. 1, pp. 3–17, Sep. 2015, doi: 10.18383/j.tom.2015.00136.

[9] Z. Cheng et al., “Imaging the Nigrosome 1 in the substantia nigra using susceptibility weighted imaging and quantitative susceptibility mapping: An application to Parkinson’s disease,” NeuroImage Clin., vol. 25, p. 102103, 2020, doi: 10.1016/j.nicl.2019.102103.

[10] S. Haller, E. M. Haacke, M. M. Thurnher, and F. Barkhof, “Susceptibility-weighted Imaging: Technical Essentials and Clinical Neurologic Applications,” Radiology, vol. 299, no. 1, pp. 3–26, Apr. 2021, doi: 10.1148/radiol.2021203071.

[11] S. R. S. Barnes and E. M. Haacke, “Susceptibility-Weighted Imaging: Clinical Angiographic Applications,” Magn. Reson. Imaging Clin. N. Am., vol. 17, no. 1, pp. 47–61, Feb. 2009, doi: 10.1016/j.mric.2008.12.002.

[12] L. Yang and S. Luo, “Clinical application of susceptibility-weighted imaging in the evaluation of leptomeningeal collateralization,” Medicine (Baltimore), vol. 97, no. 51, p. e13345, Dec. 2018, doi: 10.1097/MD.0000000000013345.

[13] E. M. Haacke et al., “Imaging iron stores in the brain using magnetic resonance imaging,” Magn. Reson. Imaging, vol. 23, no. 1, pp. 1–25, Jan. 2005, doi: 10.1016/j.mri.2004.10.001.

[14] J. F. Schenck and E. A. Zimmerman, “High-field magnetic resonance imaging of brain iron: birth of a biomarker?,” NMR Biomed., vol. 17, no. 7, pp. 433–445, Nov. 2004, doi: 10.1002/nbm.922.

[15] Y. Wang and T. Liu, “Quantitative susceptibility mapping (QSM): Decoding MRI data for a tissue magnetic biomarker,” Magn. Reson. Med., vol. 73, no. 1, pp. 82–101, Jan. 2015, doi: 10.1002/mrm.25358.

[16] B. Larsen et al., “Longitudinal development of brain iron is linked to cognition in youth,” J. Neurosci., vol. 40, no. 9, pp. 1810–1818, 2020, doi: 10.1523/JNEUROSCI.2434-19.2020.

[17] J. L. Hect, A. M. Daugherty, K. M. Hermez, and M. E. Thomason, “‘Developmental variation in regional brain iron and its relation to cognitive functions in childhood’: Erratum,” Dev. Cogn. Neurosci., vol. 45, p. No Pagination Specified-No Pagination Specified, 2020.

[18] S. Chang et al., “Quantitative Susceptibility Mapping of Intracerebral Hemorrhages at Various Stages,” J. Magn. Reson. Imaging JMRI, vol. 44, no. 2, pp. 420–425, Aug. 2016, doi: 10.1002/jmri.25143.

[19] H. Sun et al., “Quantitative Susceptibility Mapping for Following Intracranial Hemorrhage,” Radiology, vol. 288, no. 3, pp. 830–839, Sep. 2018, doi: 10.1148/radiol.2018171918.

[20] Y. Wang et al., “Clinical Quantitative Susceptibility Mapping (QSM) – Biometal Imaging and its Emerging Roles in Patient Care,” J. Magn. Reson. Imaging JMRI, vol. 46, no. 4, pp. 951–971, Oct. 2017, doi: 10.1002/jmri.25693.

[21] A. Deistung, E. Dittrich, J. Sedlacik, A. Rauscher, and J. R. Reichenbach, “ToF-SWI: simultaneous time of flight and fully flow compensated susceptibility weighted imaging,” J. Magn. Reson. Imaging JMRI, vol. 29, no. 6, pp. 1478–1484, Jun. 2009, doi: 10.1002/jmri.21673.

[22] Y. Chen, S. Liu, S. Buch, J. Hu, Y. Kang, and E. M. Haacke, “An interleaved sequence for simultaneous magnetic resonance angiography (MRA), susceptibility weighted imaging (SWI) and quantitative susceptibility mapping (QSM),” Magn. Reson. Imaging, vol. 47, pp. 1–6, Apr. 2018, doi: 10.1016/j.mri.2017.11.005.

[23] S.-H. Park, C.-H. Moon, and K. T. Bae, “Compatible dual-echo arteriovenography (CODEA) using an echo-specific K-space reordering scheme,” Magn. Reson. Med., vol. 61, no. 4, pp. 767–774, Apr. 2009, doi: 10.1002/mrm.21935.

[24] S.-H. Park, H. Shim, C.-H. Moon, J.-H. Kim, and K. T. Bae, “Quantitative evaluation of k-space reordering schemes for compatible dual-echo arteriovenography (CODEA),” Magn. Reson. Med., vol. 63, no. 5, pp. 1404–1410, May 2010, doi: 10.1002/mrm.22304.

[25] K. T. Bae, S.-H. Park, C.-H. Moon, J.-H. Kim, D. Kaya, and T. Zhao, “Dual-Echo Arteriovenography Imaging with 7 Tesla MR,” J. Magn. Reson. Imaging JMRI, vol. 31, no. 1, pp. 255–261, Jan. 2010, doi: 10.1002/jmri.22019.

[26] W.-J. Do, S. H. Choi, and S.-H. Park, “Simultaneous Variable-Slab Dual-Echo TOF MR Angiography and Susceptibility-Weighted Imaging,” IEEE Trans. Med. Imaging, vol. 37, no. 7, pp. 1632–1640, Jul. 2018, doi: 10.1109/TMI.2018.2789923.

[27] T. Boeckh-Behrens et al., “Susceptibility-weighted angiography (SWAN) of cerebral veins and arteries compared to TOF-MRA,” Eur. J. Radiol., vol. 81, no. 6, pp. 1238–1245, Jun. 2012, doi: 10.1016/j.ejrad.2011.02.057.

[28] L. Chen et al., “Enhanced susceptibility-weighted angiography (ESWAN) of cerebral arteries and veins at 1.5 Tesla,” Br. J. Radiol., vol. 87, no. 1039, p. 20130486, Jul. 2014, doi: 10.1259/bjr.20130486.

[29] Y. Ye, J. Hu, D. Wu, and E. M. Haacke, “Noncontrast-enhanced magnetic resonance angiography and venography imaging with enhanced angiography,” J. Magn. Reson. Imaging JMRI, vol. 38, no. 6, pp. 1539–1548, Dec. 2013, doi: 10.1002/jmri.24128.

[30] Y. P. Du, Z. Jin, Y. Hu, and J. Tanabe, “Multi-echo acquisition of MR angiography and venography of the brain at 3 Tesla,” J. Magn. Reson. Imaging JMRI, vol. 30, no. 2, pp. 449–454, Aug. 2009, doi: 10.1002/jmri.21833.

[31] W. Li et al., “Whole-Brain Arteriography and Venography Using Improved Velocity-Selective Saturation Pulse Trains,” Magn. Reson. Med., vol. 79, no. 4, pp. 2014–2023, Apr. 2018, doi: 10.1002/mrm.26864.

[32] Y. Ye, J. Lyu, Y. Hu, Z. Zhang, J. Xu, and W. Zhang, “MULTI-parametric MR imaging with fLEXible design (MULTIPLEX),” Magn. Reson. Med., vol. 87, no. 2, pp. 658–673, Feb. 2022, doi: 10.1002/mrm.28999.

[33] W. Bian et al., “Simultaneous imaging of radiation-induced cerebral microbleeds, arteries and veins, using a multiple gradient echo sequence at 7 Tesla,” J. Magn. Reson. Imaging JMRI, vol. 42, no. 2, pp. 269–279, Aug. 2015, doi: 10.1002/jmri.24802.

[34] E. M. Haacke, R. W. Brown, M. R. Thompson, and R. Venkatesan, Magnetic Resonance Imaging: Physical Principles and Sequence Design, 1st edition. New York: Wiley-Liss, 1999.

[35] T. Nägele, U. Klose, W. Grodd, D. Petersen, and J. Tintera, “The effects of linearly increasing flip angles on 3D inflow MR angiography,” Magn. Reson. Med., vol. 31, no. 5, pp. 561–566, May 1994, doi: 10.1002/mrm.1910310515.

[36] A. M. Eissa and A. H. Wilman, “Effects of RF inhomogeneity at 3.0T on ramped RF excitation: Application to 3D time-of-flight MR angiography of the intracranial arteries,” J. Magn. Reson. Imaging, vol. 25, no. 3, pp. 466–472, 2007, doi: 10.1002/jmri.20832.

[37] S. M. Smith, “Fast robust automated brain extraction,” Hum. Brain Mapp., vol. 17, no. 3, pp. 143–155, Nov. 2002, doi: 10.1002/hbm.10062.

[38] M. Jenkinson, “Fast, automated, N-dimensional phase-unwrapping algorithm,” Magn. Reson. Med., vol. 49, no. 1, pp. 193–197, Jan. 2003, doi: 10.1002/mrm.10354.

[39] P. S. Özbay, A. Deistung, X. Feng, D. Nanz, J. R. Reichenbach, and F. Schweser, “A comprehensive numerical analysis of background phase correction with V-SHARP,” NMR Biomed., vol. 30, no. 4, p. e3550, 2017, doi: 10.1002/nbm.3550.

[40] W. Li, B. Wu, and C. Liu, “Quantitative susceptibility mapping of human brain reflects spatial variation in tissue composition,” NeuroImage, vol. 55, no. 4, pp. 1645–1656, Apr. 2011, doi: 10.1016/j.neuroimage.2010.11.088.

[41] T. Liu et al., “Morphology enabled dipole inversion (MEDI) from a single-angle acquisition: comparison with COSMOS in human brain imaging,” Magn. Reson. Med., vol. 66, no. 3, pp. 777–783, Sep. 2011, doi: 10.1002/mrm.22816.

[42] D. D. Blatter, D. L. Parker, and R. O. Robison, “Cerebral MR angiography with multiple overlapping thin slab acquisition. Part I. Quantitative analysis of vessel visibility.,” Radiology, vol. 179, no. 3, pp. 805–811, Jun. 1991, doi: 10.1148/radiology.179.3.2027996.

[43] W. L. Davis, S. H. Warnock, H. R. Harnsberger, D. L. Parker, and C. X. Chen, “Intracranial MRA: single volume vs. multiple thin slab 3D time-of-flight acquisition,” J. Comput. Assist. Tomogr., vol. 17, no. 1, pp. 15–21, Feb. 1993.

[44] G. Mihai, O. P. Simonetti, and P. Thavendiranathan, “Noncontrast MRA for the Diagnosis of Vascular Diseases,” Cardiol. Clin., vol. 29, no. 3, pp. 341–350, Aug. 2011, doi: 10.1016/j.ccl.2011.04.006.

[45] N. Yaghmaie et al., “QSMART: Quantitative susceptibility mapping artifact reduction technique,” NeuroImage, vol. 231, p. 117701, May 2021, doi: 10.1016/j.neuroimage.2020.117701.

[46] N.-K. Chen and P.-H. Wu, “The use of Fourier-domain analyses for unwrapping phase images of low SNR,” Magn. Reson. Med., vol. 82, no. 1, pp. 356–366, Jul. 2019, doi: 10.1002/mrm.27719.

Chapter 6

Concluding Remarks and Future Directions

6.1 Summary and discussion

This thesis focused on advancement of QSM in order to make this technique more versatile in clinical applications. Hence the limitations of QSM have been studied and solutions have been proposed along with finding new applications.

QSM can be computed from multi-echo as well as single echo gradient echo data. In clinics, SWI is performed for diagnosis of microbleeds and hemorrhage and QSM can be computed from those single echo sequences [1]– [3]. However, standard SWI sequences require about 5 mins acquisition time which is often too long for patients to remain still. Hence motion artifacts may be observed in the data and in extreme cases, the data becomes unusable. This limitation can be overcome by

using a fast sequence. In **Chapter 2**, a rapid EPI sequence was applied to hemorrhage patients and QSM was reconstructed. The results showed that single-shot EPI-QSM enabled rapid measurement of ICH area and mean susceptibility, with reduced motion as compared with standard SWI. EPI-QSM requires minimal additional acquisition time and could be incorporated into iron tracking studies in ICH.

To further understand the effect of movement on QSM during scanning, quantification is needed. Previous studies have discussed effects of movement in patient studies, effects of respiratory motion and also classified movement patterns [4]–[7]. In **Chapter 3**, the effects of both movement and respiration on QSM were investigated quantitatively. It was found that even though statistically significant quantitative difference is observed in susceptibility values for artifacts caused by translational movement, respiratory fluctuations did not cause statistically significant variation in the actual susceptibility values. However, respiratory variation is still a contributing factor for variation in susceptibility values and hence should be considered and corrected for when possible.

SWI is commonly used in clinics for diagnosis and follow-up of microbleeds and hemorrhages. However, SWI has limitations such as blooming effects, and phase wrap artifacts. QSM eliminates blooming effects and provides the susceptibility values of tissues. In order to limit artifacts in SWI, a method tSWI was introduced which is similar to SWI but utilizes susceptibility maps in place of phase images [10]. **Chapter 4** studies the application of this novel tSWI method in ICH patients. In hemorrhage, tSWI was able to overcome the phase wrapping artifacts and blooming effects as observed in SWI. However, unlike SWI, tSWI required an altered upper threshold for best hemorrhage depiction that differs from the standard value. tSWI can be used as a complementary technique for visualizing hemorrhages along with SWI.

Another way of making QSM more adaptable is if a sequence designed for other application can provide QSM in addition. For example, planned TOF-MRA acquisitions could be combined with QSM, provided the TOF-MRA acquisition was not compromised. Previous studies have been conducted to combine short echo angiography and long echo venography methods; however, either TOF features were not included or QSM was not reconstructed [11]–[16]. In **Chapter 5**, a new sequence was developed to compute TOF, QSM, SWI and R2* simultaneously. The sequence was developed keeping the key features of TOF-MRA and the effect of those features were studied on QSM, indicating that the method can provide acceptable QSM while retaining the key TOF-MRA features.

Overall, this thesis has examined a number of possible steps to forward the field of QSM.

6.2 Limitations

The studies conducted have widened the possibility of application for QSM; however, there are several limitations in these studies. QSM involves several image processing steps including brain extraction, phase unwrapping, background removal, and dipole inversion. In the phase unwrapping step, the accuracy and SNR level of phase measurements can influence the unwrapping results. Regions with fast decaying signal intensities have low SNR and conventional phase unwrapping steps can be affected, resulting in some remnant wraps in the unwrapped phase which can lead to artifacts in QSM in some cases. QSM computation steps typically include a skull stripping or brain extraction step which is frequently performed using BET from FSL. This method usually works well; however, could be a bit problematic in some cases such as in images with motion. The susceptibility maps generated typically do not provide reliable susceptibility values at the edge of the brain as the background field removal methods either require edge erosion of the brain tissue

or produce local field maps that are not accurate at the brain edge. There are some papers [17], [18] that have studied whole brain QSM reconstruction, but it is still an area of ongoing research. As it stands, QSM remains somewhat unreliable at the edge of the brain which limits some applications in the cortical layers adjacent to the skull.

Most of the QSM methods conducted in this thesis used single echo QSM computed from a long single echo time (20 ms at 3T) derived from a standard SWI sequence, which is the current clinical protocol for clinical studies at our institution. Multi-echo acquisitions would be preferred for QSM since this would eliminate many of the low SNR results found with long TE times in short T2* regions. In the future, it is likely that multi-echo gradient echo [19] will be more common in clinical settings.

In Chapter 4, tSWI was compared to standard SWI; while the findings clearly indicate the differences between the methods, the lack of a gold standard makes the comparison and evaluation of tSWI method difficult. Future studies for hemorrhage could benefit from use of a same-day CT scan for example as a reference standard for comparison of volume; however, CT will not depict all details found on MRI.

In Chapter 5, the TOF-QSM sequence developed did not have full flow compensation. This resulted in small flow artifacts in the SWI and QSM images computed from the third echo. Flow compensation gradients can be inserted in the middle after the first echo in place of the second echo. For the goals of this project, the lack of flow compensation in the second echo did not affect the main findings which addressed how various TOF features affect QSM reconstruction.

6.3 Future Directions

QSM is not yet widely used in standard clinical applications and one of the reasons is the absence of a gold standard processing approach. There are many algorithms which lead to different results and further standardization is necessary. The QSM pipeline involves fairly complex, computationally rigorous steps which often need careful optimization for specific applications. Hence, more studies are required to compare and standardize the QSM reconstruction pipeline.

QSM computation involves several mathematical steps, and every step can be performed by several methods. However, most of these methods have limitations for low SNR regions. The acute hemorrhagic regions often have a faster T2* decay causing signal loss and low SNR. Currently the superposition method used requires extra steps and hence is more complex and time consuming. Development of faster and more efficient methods for QSM computation for low SNR and high susceptibility regions is a future scope.

This thesis has focused on QSM applications in the brain. However, QSM can be applied to other regions in the body like the abdomen or heart. Vascular imaging in other body parts can also be done with QSM. However, imaging in other body regions would involve higher motion challenges from both movement and respiration, as well as increased chemical shift effects from fat. Hence, future studies are needed to understand and correct the effect of various fluctuations that affect QSM and susceptibility values for quantitative comparisons.

Currently, deep learning approaches [20] are showing promise and have been able to overcome a few of the limitations in conventional methods and in some cases have drastically improved the processing speed. However, there are several new challenges that have risen from the deep learning approach which need more research. These methods find their application in many regions of the

body, including brain, neck, liver for example. Hence there is a future opportunity for research and studies to improve deep learning models and in turn QSM reconstruction pipelines with these deep learning models.

In this thesis, patient studies were limited to hemorrhage studies. In that area, previous works have shown that QSM can be used for following hemorrhages over time [3]. Future studies could attempt to understand the exact time course of QSM changes in hemorrhage and relate it to clinical management. More generally, QSM has a wide range of patient applications that should be pursued. In essence, any disease with known effects from iron could be followed with QSM. Diseases under study include multiple sclerosis, Alzheimer's disease, and Parkinson's disease amongst others [21]–[26]. Future advances will undoubtedly make QSM faster, more robust and a common clinical tool.

References

[1] E. M. Haacke, Y. Xu, Y.-C. N. Cheng, and J. R. Reichenbach, "Susceptibility weighted imaging (SWI)," Magn. Reson. Med., vol. 52, no. 3, pp. 612–618, Sep. 2004, doi: 10.1002/mrm.20198.

[2] S. Liu et al., "Susceptibility-weighted imaging: current status and future directions," NMR Biomed., vol. 30, no. 4, Apr. 2017, doi: 10.1002/nbm.3552.

[3] H. Sun et al., "Quantitative Susceptibility Mapping for Following Intracranial Hemorrhage," Radiology, vol. 288, no. 3, pp. 830–839, Sep. 2018, doi: 10.1148/radiol.2018171918.

[4] F. Godenschweger et al., "Motion correction in MRI of the brain," Phys. Med. Biol., vol. 61, no. 5, pp. R32–R56, Mar. 2016, doi: 10.1088/0031-9155/61/5/R32.

[5] J. Meineke et al., "Motion artifacts in standard clinical setting obscure disease-specific

differences in quantitative susceptibility mapping," Phys. Med. Biol., vol. 63, no. 14, p. 14NT01, Jul. 2018, doi: 10.1088/1361-6560/aacc52.

[6] H. Mattern, A. Sciarra, F. Lüsebrink, J. Acosta-Cabronero, and O. Speck, "Prospective motion correction improves high-resolution quantitative susceptibility mapping at 7T," Magn. Reson. Med., vol. 81, no. 3, pp. 1605–1619, Mar. 2019, doi: 10.1002/mrm.27509.

[7] J. Y. Choi, J. Lee, Y. Nam, J. Lee, and S.-H. Oh, "Improvement of reproducibility in quantitative susceptibility mapping (QSM) and transverse relaxation rates ($R2^*$) after physiological noise correction," J. Magn. Reson. Imaging JMRI, vol. 49, no. 6, pp. 1769–1776, Jun. 2019, doi: 10.1002/jmri.26522.

[8] H. Sun, M. Kate, L. C. Gioia, D. J. Emery, K. Butcher, and A. H. Wilman, "Quantitative susceptibility mapping using a superposed dipole inversion method: Application to intracranial hemorrhage," Magn. Reson. Med., vol. 76, no. 3, pp. 781–791, Sep. 2016, doi: 10.1002/mrm.25919.

[9] N.-K. Chen and P.-H. Wu, "The use of Fourier-domain analyses for unwrapping phase images of low SNR," Magn. Reson. Med., vol. 82, no. 1, pp. 356–366, Jul. 2019, doi: 10.1002/mrm.27719.

[10] S. Liu et al., "Improved MR venography using quantitative susceptibility-weighted imaging," J. Magn. Reson. Imaging JMRI, vol. 40, no. 3, pp. 698–708, Sep. 2014, doi: 10.1002/jmri.24413.

[11] Y. Chen, S. Liu, S. Buch, J. Hu, Y. Kang, and E. M. Haacke, "An interleaved sequence for simultaneous magnetic resonance angiography (MRA), susceptibility weighted imaging (SWI) and quantitative susceptibility mapping (QSM)," Magn. Reson. Imaging, vol. 47, pp. 1–6, Apr. 2018, doi: 10.1016/j.mri.2017.11.005.

[12] S.-H. Park, C.-H. Moon, and K. T. Bae, “Compatible dual-echo arteriovenography (CODEA) using an echo-specific K-space reordering scheme,” Magn. Reson. Med., vol. 61, no. 4, pp. 767–774, Apr. 2009, doi: 10.1002/mrm.21935.

[13] S.-H. Park, H. Shim, C.-H. Moon, J.-H. Kim, and K. T. Bae, “Quantitative evaluation of k-space reordering schemes for compatible dual-echo arteriovenography (CODEA),” Magn. Reson. Med., vol. 63, no. 5, pp. 1404–1410, May 2010, doi: 10.1002/mrm.22304.

[14] K. T. Bae, S.-H. Park, C.-H. Moon, J.-H. Kim, D. Kaya, and T. Zhao, “Dual-Echo Arteriovenography Imaging with 7 Tesla MR,” J. Magn. Reson. Imaging JMRI, vol. 31, no. 1, pp. 255–261, Jan. 2010, doi: 10.1002/jmri.22019.

[15] T. Boeckh-Behrens et al., “Susceptibility-weighted angiography (SWAN) of cerebral veins and arteries compared to TOF-MRA,” Eur. J. Radiol., vol. 81, no. 6, pp. 1238–1245, Jun. 2012, doi: 10.1016/j.ejrad.2011.02.057.

[16] L. Chen et al., “Enhanced susceptibility-weighted angiography (ESWAN) of cerebral arteries and veins at 1.5 Tesla,” Br. J. Radiol., vol. 87, no. 1039, p. 20130486, Jul. 2014, doi: 10.1259/bjr.20130486.

[17] H. Wei et al., “Learning-based single-step quantitative susceptibility mapping reconstruction without brain extraction,” NeuroImage, vol. 202, p. 116064, Nov. 2019, doi: 10.1016/j.neuroimage.2019.116064.

[18] H. Sun, Y. Ma, M. E. MacDonald, and G. B. Pike, “Whole head quantitative susceptibility mapping using a least-norm direct dipole inversion method,” NeuroImage, vol. 179, pp. 166–175, Oct. 2018, doi: 10.1016/j.neuroimage.2018.06.036.

[19] K. Eckstein et al., “Improved susceptibility weighted imaging at ultra-high field using bipolar multi-echo acquisition and optimized image processing: CLEAR-SWI,” NeuroImage, vol.

237, p. 118175, Aug. 2021, doi: 10.1016/j.neuroimage.2021.118175.

[20] W. Jung, S. Bollmann, and J. Lee, “Overview of quantitative susceptibility mapping using deep learning: Current status, challenges and opportunities,” NMR Biomed., vol. 35, no. 4, p. e4292, 2022, doi: 10.1002/nbm.4292.

[21] S. Eskreis-Winkler et al., “Multiple sclerosis lesion geometry in quantitative susceptibility mapping (QSM) and phase imaging,” J. Magn. Reson. Imaging JMRI, vol. 42, no. 1, pp. 224–229, Jul. 2015, doi: 10.1002/jmri.24745.

[22] C. Langkammer et al., “Quantitative susceptibility mapping in multiple sclerosis,” Radiology, vol. 267, no. 2, pp. 551–559, May 2013, doi: 10.1148/radiol.12120707.

[23] P. M. Cogswell et al., “Associations of quantitative susceptibility mapping with Alzheimer’s disease clinical and imaging markers,” NeuroImage, vol. 224, p. 117433, Jan. 2021, doi: 10.1016/j.neuroimage.2020.117433.

[24] H.-G. Kim et al., “Quantitative susceptibility mapping to evaluate the early stage of Alzheimer’s disease,” NeuroImage Clin., vol. 16, pp. 429–438, 2017, doi: 10.1016/j.nicl.2017.08.019.

[25] Z. Cheng et al., “Imaging the Nigrosome 1 in the substantia nigra using susceptibility weighted imaging and quantitative susceptibility mapping: An application to Parkinson’s disease,” NeuroImage Clin., vol. 25, p. 102103, 2020, doi: 10.1016/j.nicl.2019.102103.

[26] S. Tan et al., “Utility of quantitative susceptibility mapping and diffusion kurtosis imaging in the diagnosis of early Parkinson’s disease,” NeuroImage Clin., vol. 32, p. 102831, 2021, doi: 10.1016/j.nicl.2021.102831.

Appendix A

Application of Fourier-domain Analysis Based Unwrapping Technique in Quantitative Susceptibility Mapping (QSM) of Intracerebral Hemorrhage*

*A version of the appendix was presented in ISMRM: A. De, H. Sun, K. S. Butcher, and A. H. Wilman, "Application of Fourier-domain Analysis Based Unwrapping Technique in Quantitative Susceptibility Mapping (QSM) of Intracerebral Hemorrhage", ISMRM Virtual, 2020

Abstract

QSM offers a means to measure iron content changes in hemorrhage. However, the rapid T2* decay in hemorrhage causes a severe signal loss resulting in low SNR which can affect the accuracy of standard phase unwrapping in certain cases. Fourier-domain analysis based unwrapping technique may be useful to produce susceptibility maps of hemorrhages having low SNR. This method removes residual phase wraps resulting in artifact-free QSM with boundaries of the hemorrhage area more distinct to facilitate area measurement. Thus, this method can provide more precise susceptibility maps in cases where conventional unwrapping methods fail.

A.1 Introduction

Intracerebral hemorrhage (ICH) causes approximately 15% of all strokes and leads to blood leakage into the brain parenchyma [1], [2]. Changes in the form or location of the released blood may be tracked using Quantitative Susceptibility Mapping (QSM). QSM studies in ICH have used multiple echo gradient echo, single echo standard Susceptibility Weighted Imaging (SWI), or very fast sequences like single-shot Echo-planar Imaging (EPI) [3]–[5]. However, particularly in acute and subacute stages, hemorrhages have a rapid T2* decay resulting in severe signal loss when using the longer echo times required in SWI and single-shot EPI. The resulting low SNR sometimes causes phase unwrapping algorithms to fail, leading to artifacts on QSM which obscure the ICH boundaries and alter the susceptibility value. In a previous paper, a post processing method, integrating image domain and Fourier-domain based analysis, was introduced to improve the accuracy of phase unwrapping for MRI images with low SNR. QSM utilizes unwrapped phase

to produce susceptibility maps and hence application of this unwrapping method may be useful to produce susceptibility maps of hemorrhages having low SNR.

The purpose of this study is to investigate the value of unwrapping phase images with Fourier-domain analysis for obtaining EPI-QSM and SWI-QSM in hemorrhage patients.

A.2 Methods

A.2.1 Sequences

Ten patients (5male/ 5 female, age:74 ± 10 yrs.) received MRI scans at 3T with a 3D SWI sequence (TE = 20ms, TR = 27ms, resolution = 0.85x0.85x1.5mm^3, acquisition time = 5 min) and a 2D single-shot gradient EPI sequence (TE = 25ms, resolution = 1.5x1.5x1.5mm^3, acquisition time = 27s) described in our previous paper [5].

A.2.2 Analysis

All post-processing used MATLAB 2019a (Mathworks, Natick, MA). The QSM images were reconstructed using the superposed dipole inversion method for ICH-QSM [4], [5] with best path [6] as the conventional unwrapping technique.

For the Fourier-domain analysis based unwrapping method [8], the complex image (size:N_xxN_y) was multiplied by a NxN mask to zerofill the region outside that domain. Here, a 3x3 mask was used. The Fourier-domain energy peak was identified, and its coordinates (in terms of distance from the center of the Fourier- domain matrix along x and y directions) were recorded after a 2D Fourier transformation. This process was repeated for all NxN locations in the FOV to produce

Fourier-space energy displacement maps (Δk_x, Δk_y) along x and y directions. These were then converted to phase-gradient maps ($\Delta\theta_x$ and $\Delta\theta_y$) using:

$\Delta\theta_x (x,y) = \Delta k_x(x,y)*2\pi/N_x$

$\Delta\theta_y (x,y) = \Delta k_y (x,y)*2\pi/N_y$

The phase-gradient maps thus obtained were used to improve the accuracy of the phase unwrapping in the critical ROIs in hemorrhage regions where conventional unwrapping methods failed. These ROIs were visually identified from the phase images unwrapped by best path and outlined manually. The phase gradient maps were used to calculate corrected phase values and combined using 2D numerical integration [8] with boundary conditions from successfully unwrapped phase values of the conventional unwrapping method. After phase unwrapping step, QSM was computed following similar pipeline as described in [5]

A.3 Results

Figure A.1 shows an example of the magnitude and unwrapped phase by both the conventional path-based and the Fourier-domain analysis based unwrapping methods from the EPI sequence. The residual phase wraps observed in the best path unwrapping method were reduced in the Fourier-domain analysis based unwrapping methods. Figure A.2 and Figure A.3 show a comparison of standard best path and Fourier-domain analysis based unwrapping methods for EPI and SWI sequences in 1 patient. Figure A.4 shows a comparison of the variations in susceptibility values across the hemorrhage for QSM obtained by using both unwrapping methods for EPI and SWI sequences. It is observed that the variations are smoother for the Fourier-domain analysis based unwrapping methods. Figure A.5 shows a side-by-side box plot demonstrating comparison

of mean susceptibility and area for 10 patients using EPI and SWI sequence for QSM with or without the addition of unwrapping using Fourier-domain analysis.

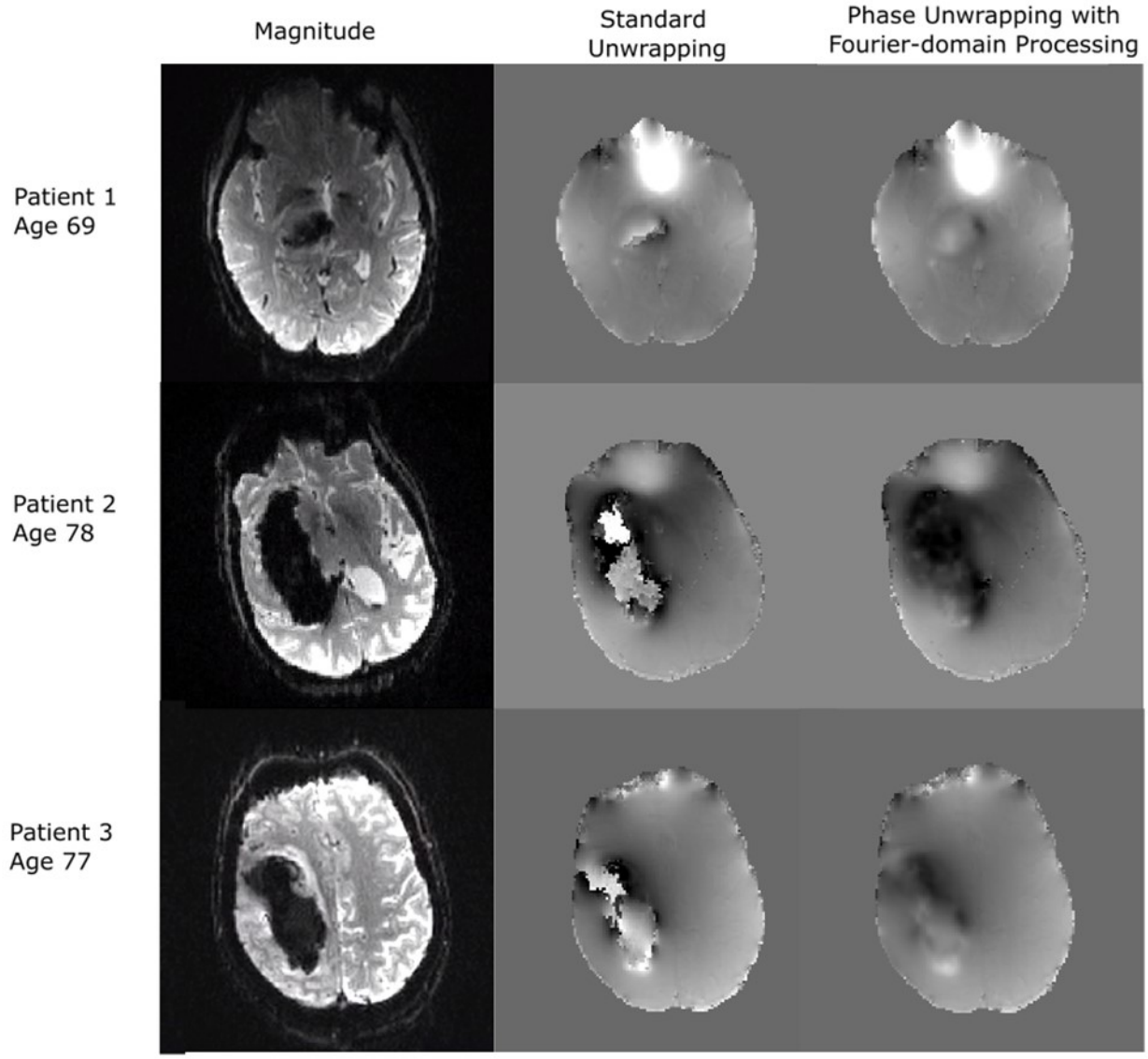

Figure A.1: A comparison of the unwrapped phase by standard (middle) and Fourier-domain analysis based unwrapping techniques (right) along with the magnitude (left) for 3 patients scanned with EPI sequence. In each case, residual wraps are observed in the conventional method which are reduced when the Fourier-domain analysis based unwrapping is applied.

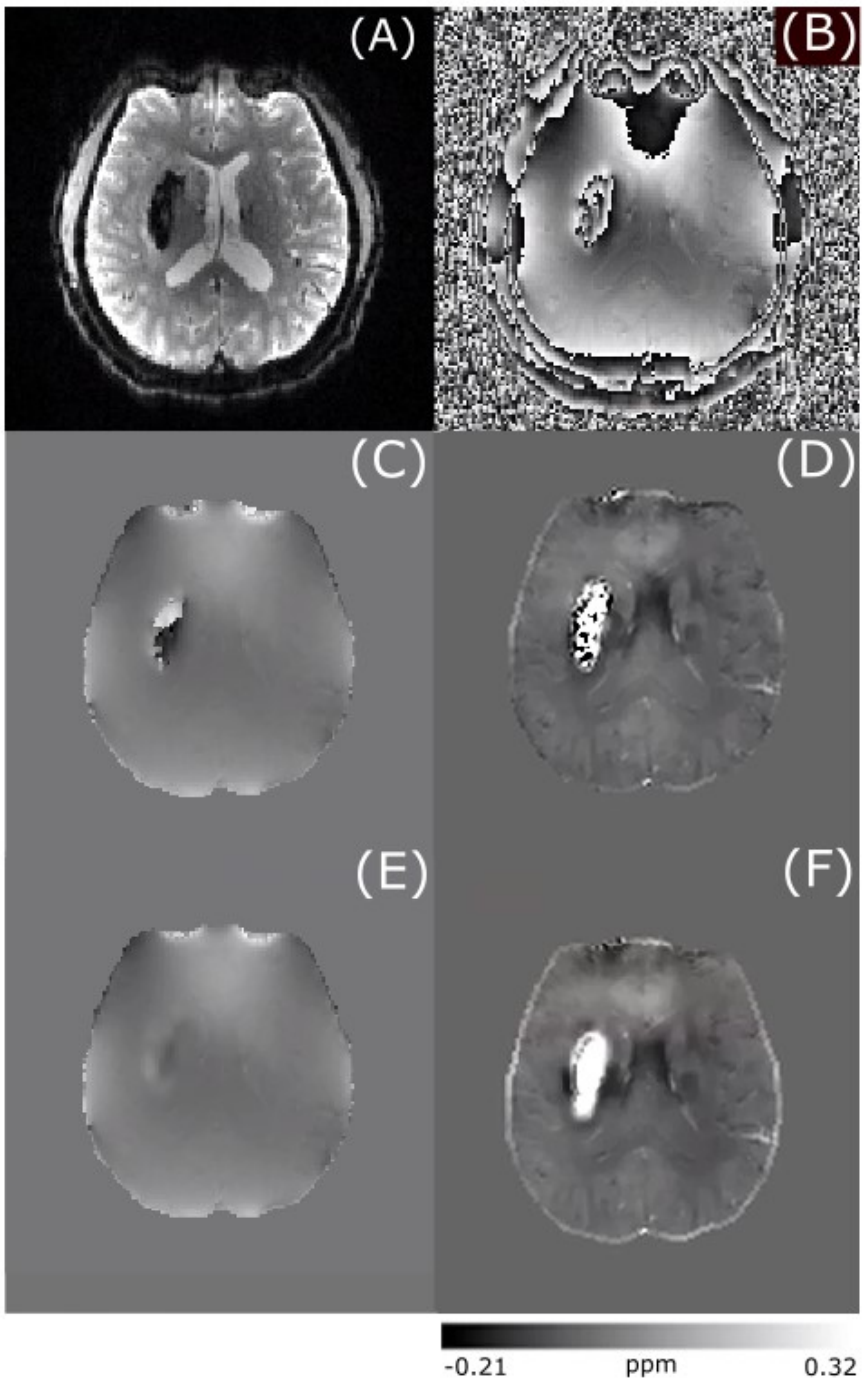

Figure A.2: Images from one patient with magnitude (A) and raw phase (B). The unwrapping methods are compared between standard unwrapped phase (C) and corresponding QSM (D), and the Fourier-domain analysis based unwrapped phase (E) and corresponding QSM (F) for EPI sequence.

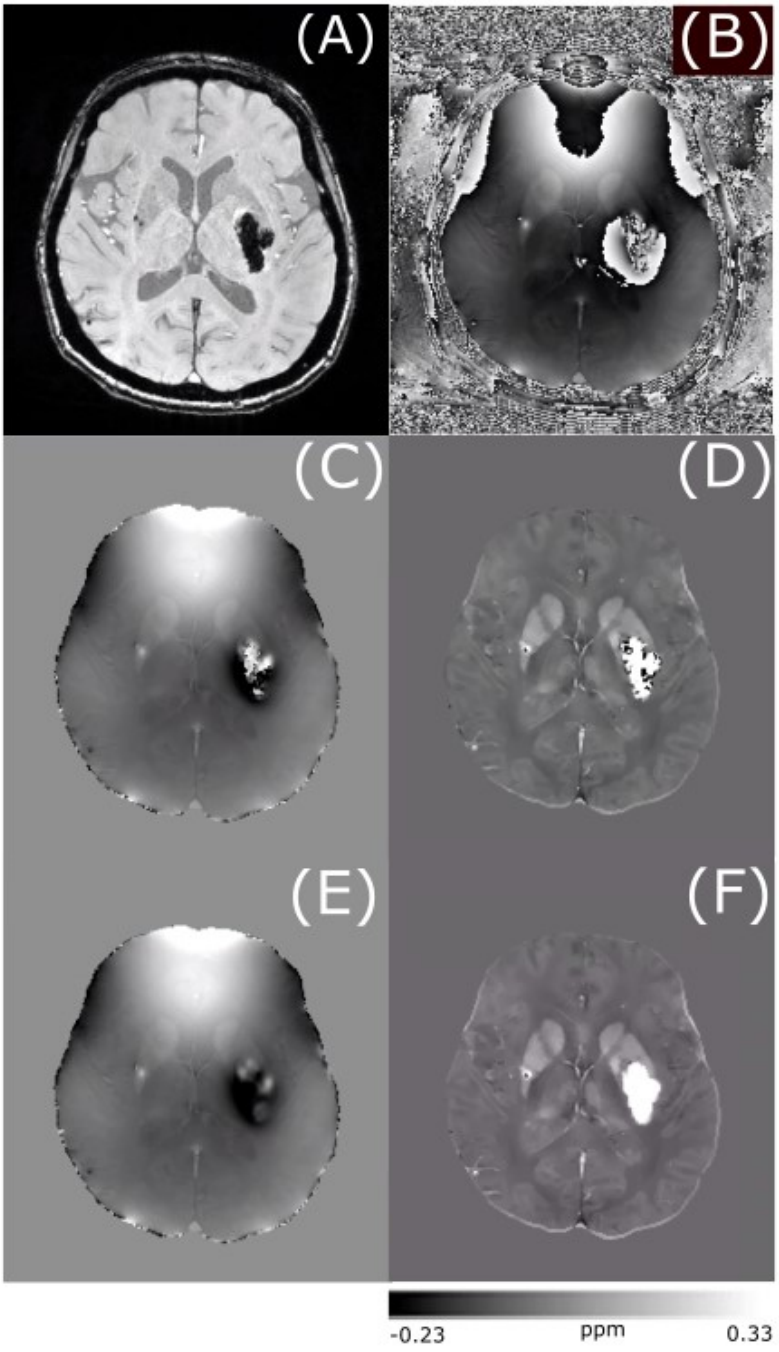

Figure A.3: Images from one subject with magnitude (A) and raw phase (B). The unwrapping methods are compared between standard unwrapped phase (C) and corresponding QSM (D), and the Fourier-domain analysis based unwrapped phase (E) and corresponding QSM (F) for SWI sequence.

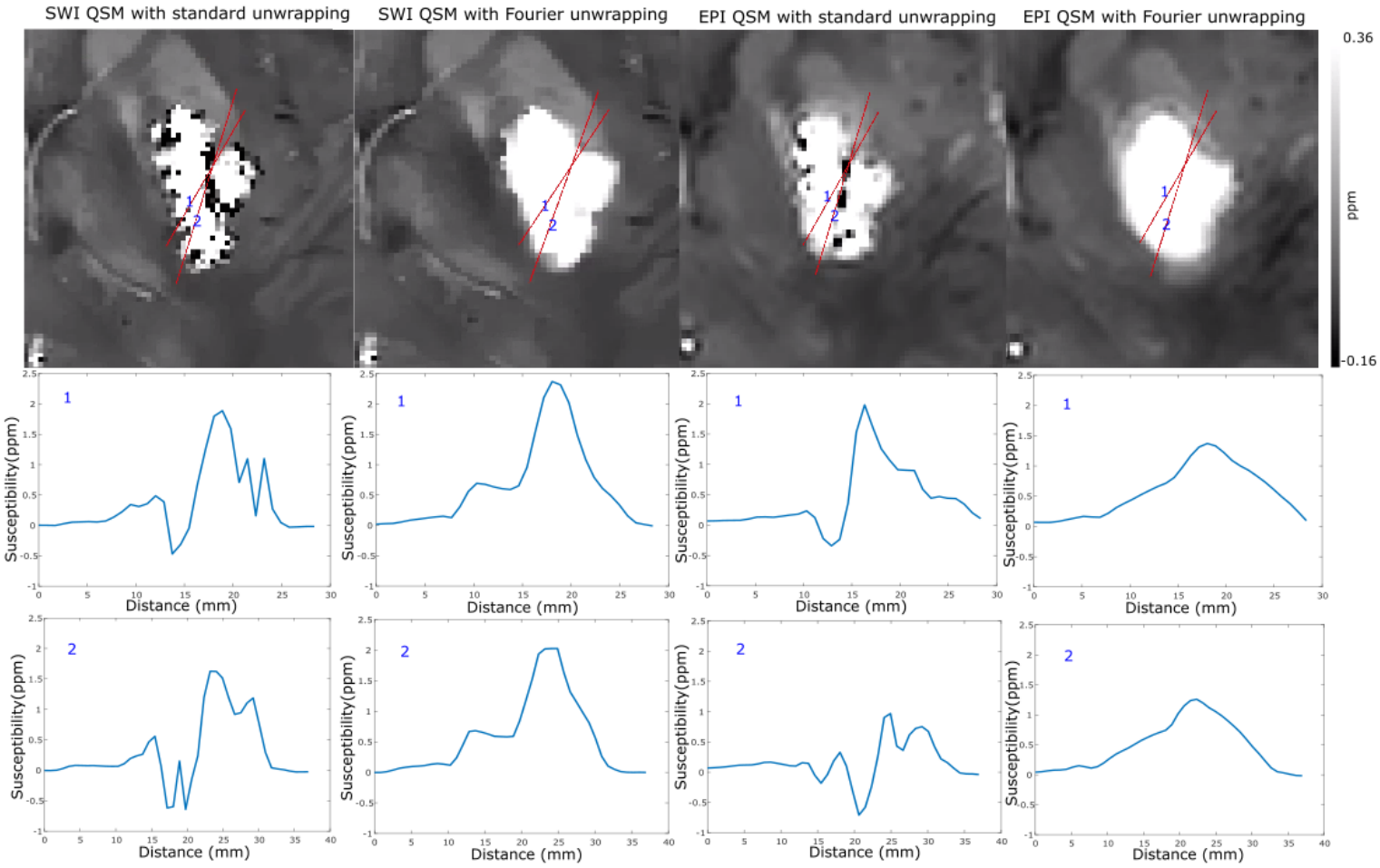

Figure A.4: A comparison of the variations in susceptibility values across a hemorrhage in QSM obtained from conventional and Fourier-domain analysis based unwrapping methods for both SWI and EPI sequences.

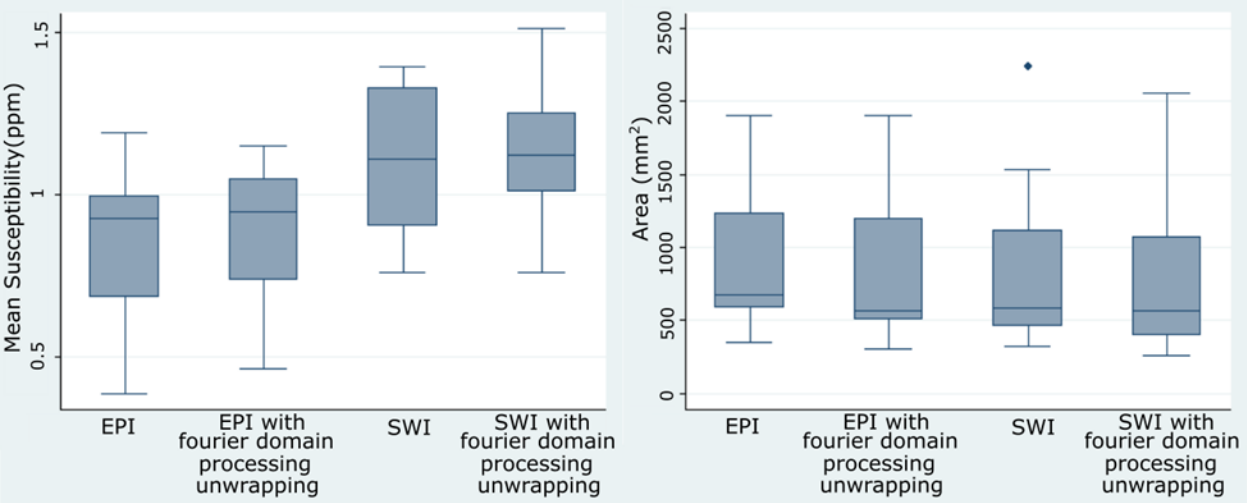

Figure A.5: Side-by-side box plot demonstrating comparison of mean susceptibility and area for 10 patients for EPI-QSM with standard unwrapping and with unwrapping using Fourier-domain analysis, SWI-QSM with standard unwrapping and with unwrapping using Fourier-domain analysis.

A.4 Discussion

QSM requires accurate phase information and hence residual phase wraps after unwrapping can cause artifacts in susceptibility maps. In EPI due to the low resolution, phase unwrapping failure is more predominant than SWI. Using the Fourier-domain analysis based unwrapping provides QSM without such artifact, making the ICH boundaries more distinct. Hence automatic segmentation by thresholding could benefit from use of this method, despite the fact that both methods showed similar mean susceptibility and area. Even though the area measurements are similar, the median of mean susceptibility of EPI-QSM with Fourier-domain analysis-based unwrapping was higher than the conventional unwrapping method. For SWI, the patients (4 out of

10 in this patient group) with unwrapping artifacts (as seen in example Figure 3.3) had an increase in the mean susceptibility value. The susceptibility values of EPI-QSM are still lower than the SWI-QSM due to the lower resolution of EPI [9].

A.5 Conclusion

Unwrapping using Fourier-domain analysis removed residual wraps in the hemorrhage regions with low SNR. This resulted in artifact-free QSM with boundaries of the hemorrhage area more distinct to facilitate area measurement. Thus, this method can provide more precise susceptibility maps in cases where conventional unwrapping methods fail.

A.6 Acknowledgements

Research support from Canadian Institutes of Health Research.

We thank Mitacs for partial salary support to AD.

References

[1] A. Morotti *et al.*, "CT Angiography Spot Sign, Hematoma Expansion, and Outcome in Primary Pontine Intracerebral Hemorrhage," *Neurocrit. Care*, vol. 25, no. 1, pp. 79–85, Aug. 2016, doi: 10.1007/s12028-016-0241-2.

[2] C. J. van Asch, M. J. Luitse, G. J. Rinkel, I. van der Tweel, A. Algra, and C. J. Klijn, "Incidence, case fatality, and functional outcome of intracerebral haemorrhage over time, according to age, sex, and ethnic origin: a systematic review and meta-analysis," *Lancet Neurol.*, vol. 9, no. 2, pp. 167–176, Feb. 2010, doi: 10.1016/S1474-4422(09)70340-0.

[3] S. Chang *et al.*, "Quantitative Susceptibility Mapping of Intracerebral Hemorrhages at Various Stages," *J. Magn. Reson. Imaging JMRI*, vol. 44, no. 2, pp. 420–425, Aug. 2016, doi: 10.1002/jmri.25143.

[4] H. Sun, M. Kate, L. C. Gioia, D. J. Emery, K. Butcher, and A. H. Wilman, "Quantitative susceptibility mapping using a superposed dipole inversion method: Application to intracranial hemorrhage," *Magn. Reson. Med.*, vol. 76, no. 3, pp. 781–791, Sep. 2016, doi: 10.1002/mrm.25919.

[5] A. De, H. Sun, D. J. Emery, K. S. Butcher, and A. H. Wilman, "Rapid quantitative susceptibility mapping of intracerebral hemorrhage," *J. Magn. Reson. Imaging JMRI*, vol. 51, no. 3, pp. 712–718, Mar. 2020, doi: 10.1002/jmri.26850.

[6] H. S. Abdul-Rahman, M. A. Gdeisat, D. R. Burton, M. J. Lalor, F. Lilley, and C. J. Moore, "Fast and robust three-dimensional best path phase unwrapping algorithm," *Appl. Opt.*, vol. 46, no. 26, pp. 6623–6635, Sep. 2007, doi: 10.1364/ao.46.006623.

[7] D. Zhou, T. Liu, P. Spincemaille, and Y. Wang, "Background field removal by solving the Laplacian boundary value problem," *NMR Biomed.*, vol. 27, no. 3, pp. 312–319, Mar. 2014, doi: 10.1002/nbm.3064.

[8] N.-K. Chen and P.-H. Wu, "The use of Fourier-domain analyses for unwrapping phase images of low SNR," *Magn. Reson. Med.*, vol. 82, no. 1, pp. 356–366, Jul. 2019, doi: 10.1002/mrm.27719.

[9] D. Zhou, J. Cho, J. Zhang, P. Spincemaille, and Y. Wang, "Susceptibility underestimation in a high-susceptibility phantom: Dependence on imaging resolution, magnitude contrast, and other parameters," *Magn. Reson. Med.*, vol. 78, no. 3, pp. 1080–1086, Sep. 2017, doi: 10.1002/mrm.26475.

Bibliography

P. S. Özbay, A. Deistung, X. Feng, D. Nanz, J. R. Reichenbach, and F. Schweser, "A comprehensive numerical analysis of background phase correction with V-SHARP," NMR Biomed., vol. 30, no. 4, p. e3550, 2017, doi: 10.1002/nbm.3550.

H. Bagher-Ebadian, Q. Jiang, and J. R. Ewing, "A modified Fourier-based phase unwrapping algorithm with an application to MRI venography," J. Magn. Reson. Imaging JMRI, vol. 27, no. 3, pp. 649–652, Mar. 2008, doi: 10.1002/jmri.21230.

T. Liu et al., "A novel background field removal method for MRI using projection onto dipole fields (PDF)," NMR Biomed., vol. 24, no. 9, pp. 1129–1136, Nov. 2011, doi: 10.1002/nbm.1670.

D. Stäb, S. Bollmann, C. Langkammer, K. Bredies, and M. Barth, "Accelerated mapping of magnetic susceptibility using 3D planes-on-a-paddlewheel (POP) EPI at ultra-high field strength," NMR Biomed., vol. 30, no. 4, Apr. 2017, doi: 10.1002/nbm.3620.

R. L. Ehman and J. P. Felmlee, "Adaptive technique for high-definition MR imaging of moving structures," Radiology, vol. 173, no. 1, pp. 255–263, Oct. 1989, doi: 10.1148/radiology.173.1.2781017.

K. P. Pruessmann, M. Weiger, P. Börnert, and P. Boesiger, "Advances in sensitivity encoding with arbitrary k-space trajectories," Magn. Reson. Med., vol. 46, no. 4, pp. 638–651, 2001, doi: 10.1002/mrm.1241.

Y. Chen, S. Liu, S. Buch, J. Hu, Y. Kang, and E. M. Haacke, "An interleaved sequence for simultaneous magnetic resonance angiography (MRA), susceptibility weighted imaging (SWI) and quantitative susceptibility mapping (QSM)," Magn. Reson. Imaging, vol. 47, pp. 1–6, Apr. 2018, doi: 10.1016/j.mri.2017.11.005.

L. C. Evans, An Introduction to Stochastic Differential Equations. Providence, Rhode Island: American Mathematical Society, 2014.

K. Ty Bae, S.-H. Park, H. Shim, C.-H. Moon, J.-H. Kim, and E. M. Nemoto, "Application of compatible dual-echo arteriovenography in stroke: Preliminary observations," Int. J. Imaging Syst. Technol., vol. 23, no. 2, pp. 152–156, Jun. 2013, doi: 10.1002/ima.22044.

P. M. Cogswell et al., "Associations of quantitative susceptibility mapping with Alzheimer's disease clinical and imaging markers," NeuroImage, vol. 224, p. 117433, Jan. 2021, doi: 10.1016/j.neuroimage.2020.117433.

B. Bilgic, J. Polimeni, L. Wald, and K. Setsompop, “Automated tissue phase and QSM estimation from multichannel data,” p. 22.
D. Zhou, T. Liu, P. Spincemaille, and Y. Wang, “Background field removal by solving the Laplacian boundary value problem,” NMR Biomed., vol. 27, no. 3, pp. 312–319, Mar. 2014, doi: 10.1002/nbm.3064.
J. Fang, L. Bao, X. Li, P. C. M. van Zijl, and Z. Chen, “Background field removal using a region adaptive kernel for quantitative susceptibility mapping of human brain,” J. Magn. Reson. San Diego Calif 1997, vol. 281, pp. 130–140, Aug. 2017, doi: 10.1016/j.jmr.2017.05.004.
H. Sun and A. H. Wilman, “Background field removal using spherical mean value filtering and Tikhonov regularization,” Magn. Reson. Med., vol. 71, no. 3, pp. 1151–1157, 2014, doi: 10.1002/mrm.24765.
T. Liu, P. Spincemaille, L. de Rochefort, B. Kressler, and Y. Wang, “Calculation of susceptibility through multiple orientation sampling (COSMOS): A method for conditioning the inverse problem from measured magnetic field map to susceptibility source image in MRI,” Magn. Reson. Med., vol. 61, no. 1, pp. 196–204, 2009, doi: 10.1002/mrm.21828.
C. Lévy et al., “Carotid and vertebral artery dissections: three-dimensional time-of-flight MR angiography and MR imaging versus conventional angiography,” Radiology, vol. 190, no. 1, pp. 97–103, Jan. 1994, doi: 10.1148/radiology.190.1.8259436.
T. Liu, K. Surapaneni, M. Lou, L. Cheng, P. Spincemaille, and Y. Wang, “Cerebral Microbleeds: Burden Assessment by Using Quantitative Susceptibility Mapping,” Radiology, vol. 262, no. 1, pp. 269–278, Jan. 2012, doi: 10.1148/radiol.11110251.
D. D. Blatter, D. L. Parker, and R. O. Robison, “Cerebral MR angiography with multiple overlapping thin slab acquisition. Part I. Quantitative analysis of vessel visibility.,” Radiology, vol. 179, no. 3, pp. 805–811, Jun. 1991, doi: 10.1148/radiology.179.3.2027996.
L. Yang and S. Luo, “Clinical application of susceptibility-weighted imaging in the evaluation of leptomeningeal collateralization,” Medicine (Baltimore), vol. 97, no. 51, p. e13345, Dec. 2018, doi: 10.1097/MD.0000000000013345.
Y. Wang et al., “Clinical Quantitative Susceptibility Mapping (QSM) – Biometal Imaging and its Emerging Roles in Patient Care,” J. Magn. Reson. Imaging JMRI, vol. 46, no. 4, pp. 951–971, Oct. 2017, doi: 10.1002/jmri.25693.
S. D. Robinson et al., “Combining phase images from array coils using a short echo time reference scan (COMPOSER),” Magn. Reson. Med., vol. 77, no. 1, pp. 318–327, 2017, doi: 10.1002/mrm.26093.
S. Robinson, G. Grabner, S. Witoszynskyj, and S. Trattnig, “Combining phase images from multi-channel RF coils using 3D phase offset maps derived from a dual-echo scan,” Magn. Reson. Med., vol. 65, no. 6, pp. 1638–1648, Jun. 2011, doi: 10.1002/mrm.22753.
K. Gumus et al., “Comparison of optical and MR-based tracking,” Magn. Reson. Med., vol. 74, no. 3, pp. 894–902, Sep. 2015, doi: 10.1002/mrm.25472.
S.-H. Park, C.-H. Moon, and K. T. Bae, “Compatible dual-echo arteriovenography (CODEA) using an echo-specific K-space reordering scheme,” Magn. Reson. Med., vol. 61, no. 4, pp. 767–774, Apr. 2009, doi: 10.1002/mrm.21935.
K. Eckstein et al., “Computationally Efficient Combination of Multi-channel Phase Data From Multi-echo Acquisitions (ASPIRE): Combination of Multi-Channel Phase Data from Multi-Echo Acquisitions (ASPIRE),” Magn. Reson. Med., vol. 79, no. 6, pp. 2996–3006, Jun. 2018, doi: 10.1002/mrm.26963.

A. Morotti et al., “CT Angiography Spot Sign, Hematoma Expansion, and Outcome in Primary Pontine Intracerebral Hemorrhage,” Neurocrit. Care, vol. 25, no. 1, pp. 79–85, Aug. 2016, doi: 10.1007/s12028-016-0241-2.

J. Meineke and T. Nielsen, “Data consistency-driven determination of -fluctuations in gradient-echo MRI,” Magn. Reson. Med., vol. 81, no. 5, pp. 3046–3055, 2019, doi: 10.1002/mrm.27630.

P. E. Kullnig et al., “Detection of multiple intracranial hemorrhages in a child with acute lymphocytic leukemia (ALL) by susceptibility weighted imaging (SWI),” Radiol. Case Rep., vol. 2, no. 4, p. 135, 2007, doi: 10.2484/rcr.v2i4.135.

K. E. Hammond et al., “Development of a robust method for generating 7T multichannel phase images of the brain with application to normal volunteers and patients with neurological diseases,” NeuroImage, vol. 39, no. 4, pp. 1682–1692, Feb. 2008, doi: 10.1016/j.neuroimage.2007.10.037.

J. L. Hect, A. M. Daugherty, K. M. Hermez, and M. E. Thomason, “‘Developmental variation in regional brain iron and its relation to cognitive functions in childhood’: Erratum,” Dev. Cogn. Neurosci., vol. 45, p. No Pagination Specified-No Pagination Specified, 2020.

K. T. Bae, S.-H. Park, C.-H. Moon, J.-H. Kim, D. Kaya, and T. Zhao, “Dual-Echo Arteriovenography Imaging with 7 Tesla MR,” J. Magn. Reson. Imaging JMRI, vol. 31, no. 1, pp. 255–261, Jan. 2010, doi: 10.1002/jmri.22019.

A. M. Eissa and A. H. Wilman, “Effects of RF inhomogeneity at 3.0T on ramped RF excitation: Application to 3D time-of-flight MR angiography of the intracranial arteries,” J. Magn. Reson. Imaging, vol. 25, no. 3, pp. 466–472, 2007, doi: 10.1002/jmri.20832.

L. Chen et al., “Enhanced susceptibility-weighted angiography (ESWAN) of cerebral arteries and veins at 1.5 Tesla,” Br. J. Radiol., vol. 87, no. 1039, p. 20130486, Jul. 2014, doi: 10.1259/bjr.20130486.

M. Uecker et al., “ESPIRiT—an eigenvalue approach to autocalibrating parallel MRI: Where SENSE meets GRAPPA,” Magn. Reson. Med., vol. 71, no. 3, pp. 990–1001, 2014, doi: 10.1002/mrm.24751.

M. J. Cronin, N. Wang, K. S. Decker, H. Wei, W.-Z. Zhu, and C. Liu, “Exploring the origins of echo-time-dependent quantitative susceptibility mapping (QSM) measurements in healthy tissue and cerebral microbleeds,” NeuroImage, vol. 149, pp. 98–113, Apr. 2017, doi: 10.1016/j.neuroimage.2017.01.053.

H. Sun et al., “Extracting more for less: multi-echo MP2RAGE for simultaneous T1 -weighted imaging, T1 mapping, R 2 ∗ mapping, SWI, and QSM from a single acquisition,” Magn. Reson. Med., vol. 83, no. 4, pp. 1178–1191, Apr. 2020, doi: 10.1002/mrm.27975.

H. S. Abdul-Rahman, M. A. Gdeisat, D. R. Burton, M. J. Lalor, F. Lilley, and C. J. Moore, “Fast and robust three-dimensional best path phase unwrapping algorithm,” Appl. Opt., vol. 46, no. 26, pp. 6623–6635, Sep. 2007, doi: 10.1364/ao.46.006623.

M. Jenkinson, “Fast, automated, N-dimensional phase-unwrapping algorithm,” Magn. Reson. Med., vol. 49, no. 1, pp. 193–197, Jan. 2003, doi: 10.1002/mrm.10354.

M. A. Schofield and Y. Zhu, “Fast phase unwrapping algorithm for interferometric applications,” Opt. Lett., vol. 28, no. 14, pp. 1194–1196, Jul. 2003, doi: 10.1364/OL.28.001194.

C. Langkammer et al., “Fast quantitative susceptibility mapping using 3D EPI and total generalized variation,” NeuroImage, vol. 111, pp. 622–630, May 2015, doi: 10.1016/j.neuroimage.2015.02.041.

S. M. Smith, “Fast robust automated brain extraction,” Hum. Brain Mapp., vol. 17, no. 3, pp. 143–155, Nov. 2002, doi: 10.1002/hbm.10062.
B. Xu, T. Liu, P. Spincemaille, M. Prince, and Y. Wang, “Flow Compensated Quantitative Susceptibility Mapping for Venous Oxygenation Imaging,” Magn. Reson. Med. Off. J. Soc. Magn. Reson. Med. Soc. Magn. Reson. Med., vol. 72, no. 2, pp. 438–445, Aug. 2014, doi: 10.1002/mrm.24937.
J. C. Hemphill et al., “Guidelines for the Management of Spontaneous Intracerebral Hemorrhage,” Stroke, vol. 46, no. 7, pp. 2032–2060, Jul. 2015, doi: 10.1161/STR.0000000000000069.
S. Wang, M. Lou, T. Liu, D. Cui, X. Chen, and Y. Wang, “Hematoma volume measurement in gradient echo MRI using quantitative susceptibility mapping,” Stroke, vol. 44, no. 8, pp. 2315–2317, Aug. 2013, doi: 10.1161/STROKEAHA.113.001638.
K. R. Wagner, F. R. Sharp, T. D. Ardizzone, A. Lu, and J. F. Clark, “Heme and iron metabolism: role in cerebral hemorrhage,” J. Cereb. Blood Flow Metab. Off. J. Int. Soc. Cereb. Blood Flow Metab., vol. 23, no. 6, pp. 629–652, Jun. 2003, doi: 10.1097/01.WCB.0000073905.87928.6D.
S. D. Yeatts, Y. Y. Palesch, C. S. Moy, and M. Selim, “High dose deferoxamine in intracerebral hemorrhage (HI-DEF) trial: rationale, design, and methods,” Neurocrit. Care, vol. 19, no. 2, pp. 257–266, Oct. 2013, doi: 10.1007/s12028-013-9861-y.
J. F. Schenck and E. A. Zimmerman, “High-field magnetic resonance imaging of brain iron: birth of a biomarker?,” NMR Biomed., vol. 17, no. 7, pp. 433–445, Nov. 2004, doi: 10.1002/nbm.922.
L. Li and J. S. Leigh, “High-precision mapping of the magnetic field utilizing the harmonic function mean value property,” J. Magn. Reson. San Diego Calif 1997, vol. 148, no. 2, pp. 442–448, Feb. 2001, doi: 10.1006/jmre.2000.2267.
N.-J. Gong, R. Dibb, M. Bulk, L. van der Weerd, and C. Liu, “Imaging beta amyloid aggregation and iron accumulation in Alzheimer’s disease using quantitative susceptibility mapping MRI,” NeuroImage, vol. 191, pp. 176–185, May 2019, doi: 10.1016/j.neuroimage.2019.02.019.
E. M. Haacke et al., “Imaging iron stores in the brain using magnetic resonance imaging,” Magn. Reson. Imaging, vol. 23, no. 1, pp. 1–25, Jan. 2005, doi: 10.1016/j.mri.2004.10.001.
Z. Cheng et al., “Imaging the Nigrosome 1 in the substantia nigra using susceptibility weighted imaging and quantitative susceptibility mapping: An application to Parkinson’s disease,” NeuroImage Clin., vol. 25, p. 102103, 2020, doi: 10.1016/j.nicl.2019.102103.
A. Rauscher, M. Barth, K.-H. Herrmann, S. Witoszynskyj, A. Deistung, and J. R. Reichenbach, “Improved elimination of phase effects from background field inhomogeneities for susceptibility weighted imaging at high magnetic field strengths,” Magn. Reson. Imaging, vol. 26, no. 8, pp. 1145–1151, Oct. 2008, doi: 10.1016/j.mri.2008.01.029.
D. Atkinson, M. Brant-Zawadzki, G. Gillan, D. Purdy, and G. Laub, “Improved MR angiography: magnetization transfer suppression with variable flip angle excitation and increased resolution,” Radiology, vol. 190, no. 3, pp. 890–894, Mar. 1994, doi: 10.1148/radiology.190.3.8115646.
S. Liu et al., “Improved MR venography using quantitative susceptibility-weighted imaging,” J. Magn. Reson. Imaging JMRI, vol. 40, no. 3, pp. 698–708, Sep. 2014, doi: 10.1002/jmri.24413.
J. Y. Choi, J. Lee, Y. Nam, J. Lee, and S.-H. Oh, “Improvement of reproducibility in quantitative susceptibility mapping (QSM) and transverse relaxation rates ($R2^*$) after physiological

noise correction," J. Magn. Reson. Imaging JMRI, vol. 49, no. 6, pp. 1769–1776, Jun. 2019, doi: 10.1002/jmri.26522.
K. Eckstein et al., "Improved susceptibility weighted imaging at ultra-high field using bipolar multi-echo acquisition and optimized image processing: CLEAR-SWI," NeuroImage, vol. 237, p. 118175, Aug. 2021, doi: 10.1016/j.neuroimage.2021.118175.
C. J. van Asch, M. J. Luitse, G. J. Rinkel, I. van der Tweel, A. Algra, and C. J. Klijn, "Incidence, case fatality, and functional outcome of intracerebral haemorrhage over time, according to age, sex, and ethnic origin: a systematic review and meta-analysis," Lancet Neurol., vol. 9, no. 2, pp. 167–176, Feb. 2010, doi: 10.1016/S1474-4422(09)70340-0.
W. Li, A. V. Avram, B. Wu, X. Xiao, and C. Liu, "Integrated Laplacian-based phase unwrapping and background phase removal for quantitative susceptibility mapping," NMR Biomed., vol. 27, no. 2, pp. 219–227, Feb. 2014, doi: 10.1002/nbm.3056.
R. F. Keep, Y. Hua, and G. Xi, "Intracerebral haemorrhage: mechanisms of injury and therapeutic targets," Lancet Neurol., vol. 11, no. 8, pp. 720–731, Aug. 2012, doi: 10.1016/S1474-4422(12)70104-7.
W. Chen et al., "Intracranial calcifications and hemorrhages: characterization with quantitative susceptibility mapping," Radiology, vol. 270, no. 2, pp. 496–505, Feb. 2014, doi: 10.1148/radiol.13122640.
W. L. Davis, S. H. Warnock, H. R. Harnsberger, D. L. Parker, and C. X. Chen, "Intracranial MRA: single volume vs. multiple thin slab 3D time-of-flight acquisition," J. Comput. Assist. Tomogr., vol. 17, no. 1, pp. 15–21, Feb. 1993.
H. Wei et al., "Learning-based single-step quantitative susceptibility mapping reconstruction without brain extraction," NeuroImage, vol. 202, p. 116064, Nov. 2019, doi: 10.1016/j.neuroimage.2019.116064.
B. Larsen et al., "Longitudinal development of brain iron is linked to cognition in youth," J. Neurosci., vol. 40, no. 9, pp. 1810–1818, 2020, doi: 10.1523/JNEUROSCI.2434-19.2020.
M. J. Graves, "Magnetic resonance angiography," Br. J. Radiol., vol. 70, pp. 6–28, Jan. 1997, doi: 10.1259/bjr.70.829.9059290.
E. M. Haacke, R. W. Brown, M. R. Thompson, and R. Venkatesan, Magnetic Resonance Imaging: Physical Principles and Sequence Design, 1st edition. New York: Wiley-Liss, 1999.
K. Shmueli, J. A. de Zwart, P. van Gelderen, T.-Q. Li, S. J. Dodd, and J. H. Duyn, "Magnetic susceptibility mapping of brain tissue in vivo using MRI phase data," Magn. Reson. Med., vol. 62, no. 6, pp. 1510–1522, Dec. 2009, doi: 10.1002/mrm.22135.
T. Liu et al., "Morphology enabled dipole inversion (MEDI) from a single-angle acquisition: comparison with COSMOS in human brain imaging," Magn. Reson. Med., vol. 66, no. 3, pp. 777–783, Sep. 2011, doi: 10.1002/mrm.22816.
M. Zaitsev, J. Maclaren, and M. Herbst, "Motion artifacts in MRI: A complex problem with many partial solutions," J. Magn. Reson. Imaging JMRI, vol. 42, no. 4, pp. 887–901, Oct. 2015, doi: 10.1002/jmri.24850.
J. Meineke et al., "Motion artifacts in standard clinical setting obscure disease-specific differences in quantitative susceptibility mapping," Phys. Med. Biol., vol. 63, no. 14, p. 14NT01, Jul. 2018, doi: 10.1088/1361-6560/aacc52.
F. Godenschweger et al., "Motion correction in MRI of the brain," Phys. Med. Biol., vol. 61, no. 5, pp. R32–R56, Mar. 2016, doi: 10.1088/0031-9155/61/5/R32.
W. G. Bradley, "MR appearance of hemorrhage in the brain," Radiology, vol. 189, no. 1, pp. 15–26, Oct. 1993, doi: 10.1148/radiology.189.1.8372185.

B. Bilgic, A. Pfefferbaum, T. Rohlfing, E. V. Sullivan, and E. Adalsteinsson, “MRI estimates of brain iron concentration in normal aging using quantitative susceptibility mapping,” NeuroImage, vol. 59, no. 3, pp. 2625–2635, Feb. 2012, doi: 10.1016/j.neuroimage.2011.08.077.

Y. P. Du, Z. Jin, Y. Hu, and J. Tanabe, “Multi-echo acquisition of MR angiography and venography of the brain at 3 Tesla,” J. Magn. Reson. Imaging JMRI, vol. 30, no. 2, pp. 449–454, Aug. 2009, doi: 10.1002/jmri.21833.

Y. Ye, J. Lyu, Y. Hu, Z. Zhang, J. Xu, and W. Zhang, “MULTI-parametric MR imaging with fLEXible design (MULTIPLEX),” Magn. Reson. Med., vol. 87, no. 2, pp. 658–673, Feb. 2022, doi: 10.1002/mrm.28999.

S. Eskreis-Winkler et al., “Multiple sclerosis lesion geometry in quantitative susceptibility mapping (QSM) and phase imaging,” J. Magn. Reson. Imaging JMRI, vol. 42, no. 1, pp. 224–229, Jul. 2015, doi: 10.1002/jmri.24745.

G. Mihai, O. P. Simonetti, and P. Thavendiranathan, “Noncontrast MRA for the Diagnosis of Vascular Diseases,” Cardiol. Clin., vol. 29, no. 3, pp. 341–350, Aug. 2011, doi: 10.1016/j.ccl.2011.04.006.

Y. Ye, J. Hu, D. Wu, and E. M. Haacke, “Noncontrast-enhanced magnetic resonance angiography and venography imaging with enhanced angiography,” J. Magn. Reson. Imaging JMRI, vol. 38, no. 6, pp. 1539–1548, Dec. 2013, doi: 10.1002/jmri.24128.

J. H. Gao, S. K. Holland, and J. C. Gore, “Nuclear magnetic resonance signal from flowing nuclei in rapid imaging using gradient echoes,” Med. Phys., vol. 15, no. 6, pp. 809–814, Dec. 1988, doi: 10.1118/1.596197.

L. F. Shampine, “Numerical Recipes, The Art of Scientific Computing. By W. H. Press, B. P. Flannery, S. A. Teukolsky, and W. T. Vetterling,” Am. Math. Mon., vol. 94, no. 9, pp. 889–893, Nov. 1987, doi: 10.1080/00029890.1987.12000737.

J. Wen, A. H. Cross, and D. A. Yablonskiy, “On The Role of Physiological Fluctuations in Quantitative Gradient Echo MRI – Implications for GEPCI, QSM and SWI,” Magn. Reson. Med., vol. 73, no. 1, pp. 195–203, Jan. 2015, doi: 10.1002/mrm.25114.

E. M. Haacke et al., “Optimizing blood vessel contrast in fast three-dimensional MRI,” Magn. Reson. Med., vol. 14, no. 2, pp. 202–221, May 1990, doi: 10.1002/mrm.1910140207.

W. Jung, S. Bollmann, and J. Lee, “Overview of quantitative susceptibility mapping using deep learning: Current status, challenges and opportunities,” NMR Biomed., vol. 35, no. 4, p. e4292, 2022, doi: 10.1002/nbm.4292.

N. F. Ramsey et al., “Phase navigator correction in 3D fMRI improves detection of brain activation: quantitative assessment with a graded motor activation procedure,” NeuroImage, vol. 8, no. 3, pp. 240–248, Oct. 1998, doi: 10.1006/nimg.1998.0358.

S. Witoszynskyj, A. Rauscher, J. R. Reichenbach, and M. Barth, “Phase unwrapping of MR images using Phi UN--a fast and robust region growing algorithm,” Med. Image Anal., vol. 13, no. 2, pp. 257–268, Apr. 2009, doi: 10.1016/j.media.2008.10.004.

Y. Nam, D.-H. Kim, and J. Lee, “Physiological noise compensation in gradient-echo myelin water imaging,” NeuroImage, vol. 120, pp. 345–349, Oct. 2015, doi: 10.1016/j.neuroimage.2015.07.014.

D. Nishimura, Principles of Magnetic Resonance Imaging. Lulu, 2010.

Y. Wang, Principles of Magnetic Resonance Imaging: Physics Concepts, Pulse Sequences, & Biomedical Applications. CreateSpace Independent Publishing Platform, 2012.

H. Mattern, A. Sciarra, F. Lüsebrink, J. Acosta-Cabronero, and O. Speck, “Prospective motion correction improves high-resolution quantitative susceptibility mapping at 7T,” Magn. Reson. Med., vol. 81, no. 3, pp. 1605–1619, Mar. 2019, doi: 10.1002/mrm.27509.
N. Yaghmaie et al., “QSMART: Quantitative susceptibility mapping artifact reduction technique,” NeuroImage, vol. 231, p. 117701, May 2021, doi: 10.1016/j.neuroimage.2020.117701.
S.-H. Park, H. Shim, C.-H. Moon, J.-H. Kim, and K. T. Bae, “Quantitative evaluation of k-space reordering schemes for compatible dual-echo arteriovenography (CODEA),” Magn. Reson. Med., vol. 63, no. 5, pp. 1404–1410, May 2010, doi: 10.1002/mrm.22304.
F. Schweser, A. Deistung, B. W. Lehr, and J. R. Reichenbach, “Quantitative imaging of intrinsic magnetic tissue properties using MRI signal phase: an approach to in vivo brain iron metabolism?,” NeuroImage, vol. 54, no. 4, pp. 2789–2807, Feb. 2011, doi: 10.1016/j.neuroimage.2010.10.070.
L. de Rochefort et al., “Quantitative susceptibility map reconstruction from MR phase data using bayesian regularization: validation and application to brain imaging,” Magn. Reson. Med., vol. 63, no. 1, pp. 194–206, Jan. 2010, doi: 10.1002/mrm.22187.
B. Xiao et al., “Quantitative susceptibility mapping based hybrid feature extraction for diagnosis of Parkinson’s disease,” NeuroImage Clin., vol. 24, p. 102070, 2019, doi: 10.1016/j.nicl.2019.102070.
J. R. Reichenbach, F. Schweser, B. Serres, and A. Deistung, “Quantitative Susceptibility Mapping: Concepts and Applications,” Clin. Neuroradiol., vol. 25 Suppl 2, pp. 225–230, Oct. 2015, doi: 10.1007/s00062-015-0432-9.
C. Liu, H. Wei, N.-J. Gong, M. Cronin, R. Dibb, and K. Decker, “Quantitative Susceptibility Mapping: Contrast Mechanisms and Clinical Applications,” Tomogr. Ann Arbor Mich, vol. 1, no. 1, pp. 3–17, Sep. 2015, doi: 10.18383/j.tom.2015.00136.
A. Deistung et al., “Quantitative susceptibility mapping differentiates between blood depositions and calcifications in patients with glioblastoma,” PloS One, vol. 8, no. 3, p. e57924, 2013, doi: 10.1371/journal.pone.0057924.
H. Sun et al., “Quantitative Susceptibility Mapping for Following Intracranial Hemorrhage,” Radiology, vol. 288, no. 3, pp. 830–839, Sep. 2018, doi: 10.1148/radiol.2018171918.
H. Sun, “Quantitative Susceptibility Mapping in Human Brain: Methods Development and Applications,” ERA, Fall 2015. https://era.library.ualberta.ca/items/9fca9424-2918-4b65-a4f6-07d30bf99e0c (accessed Mar. 23, 2022).
C. Langkammer et al., “Quantitative susceptibility mapping in multiple sclerosis,” Radiology, vol. 267, no. 2, pp. 551–559, May 2013, doi: 10.1148/radiol.12120707.
P.-Y. Lin, T.-C. Chao, and M.-L. Wu, “Quantitative susceptibility mapping of human brain at 3T: a multisite reproducibility study,” AJNR Am. J. Neuroradiol., vol. 36, no. 3, pp. 467–474, Mar. 2015, doi: 10.3174/ajnr.A4137.
W. Li, B. Wu, and C. Liu, “Quantitative susceptibility mapping of human brain reflects spatial variation in tissue composition,” NeuroImage, vol. 55, no. 4, pp. 1645–1656, Apr. 2011, doi: 10.1016/j.neuroimage.2010.11.088.
S. Chang et al., “Quantitative Susceptibility Mapping of Intracerebral Hemorrhages at Various Stages,” J. Magn. Reson. Imaging JMRI, vol. 44, no. 2, pp. 420–425, Aug. 2016, doi: 10.1002/jmri.25143.
X. Feng, A. Deistung, and J. R. Reichenbach, “Quantitative susceptibility mapping (QSM) and R2* in the human brain at 3T: Evaluation of intra-scanner repeatability,” Z. Für Med. Phys., vol. 28, no. 1, pp. 36–48, Feb. 2018, doi: 10.1016/j.zemedi.2017.05.003.

Y. Zhang et al., “Quantitative Susceptibility Mapping (QSM) As a Means to Monitor Cerebral Hematoma Treatment,” J. Magn. Reson. Imaging JMRI, vol. 48, no. 4, pp. 907–915, Oct. 2018, doi: 10.1002/jmri.25957.
Y. Wang and T. Liu, “Quantitative susceptibility mapping (QSM): Decoding MRI data for a tissue magnetic biomarker,” Magn. Reson. Med., vol. 73, no. 1, pp. 82–101, Jan. 2015, doi: 10.1002/mrm.25358.
C. Wisnieff, S. Ramanan, J. Olesik, S. Gauthier, Y. Wang, and D. Pitt, “Quantitative susceptibility mapping (QSM) of white matter multiple sclerosis lesions: Interpreting positive susceptibility and the presence of iron,” Magn. Reson. Med., vol. 74, no. 2, pp. 564–570, Aug. 2015, doi: 10.1002/mrm.25420.
H.-G. Kim et al., “Quantitative susceptibility mapping to evaluate the early stage of Alzheimer’s disease,” NeuroImage Clin., vol. 16, pp. 429–438, 2017, doi: 10.1016/j.nicl.2017.08.019.
H. Sun, M. Kate, L. C. Gioia, D. J. Emery, K. Butcher, and A. H. Wilman, “Quantitative susceptibility mapping using a superposed dipole inversion method: Application to intracranial hemorrhage,” Magn. Reson. Med., vol. 76, no. 3, pp. 781–791, Sep. 2016, doi: 10.1002/mrm.25919.
H. Sun and A. H. Wilman, “Quantitative susceptibility mapping using single-shot echo-planar imaging,” Magn. Reson. Med., vol. 73, no. 5, pp. 1932–1938, May 2015, doi: 10.1002/mrm.25316.
B. Bilgic et al., “Rapid multi-orientation quantitative susceptibility mapping,” NeuroImage, vol. 125, pp. 1131–1141, Jan. 2016, doi: 10.1016/j.neuroimage.2015.08.015.
A. De, H. Sun, D. J. Emery, K. S. Butcher, and A. H. Wilman, “Rapid quantitative susceptibility mapping of intracerebral hemorrhage,” J. Magn. Reson. Imaging JMRI, vol. 51, no. 3, pp. 712–718, Mar. 2020, doi: 10.1002/jmri.26850.
P. Mansfield, “Real-time echo-planar imaging by NMR,” Br. Med. Bull., vol. 40, no. 2, pp. 187–190, Apr. 1984, doi: 10.1093/oxfordjournals.bmb.a071970.
P. van Gelderen, J. A. de Zwart, P. Starewicz, R. S. Hinks, and J. H. Duyn, “Real-time shimming to compensate for respiration-induced B0 fluctuations,” Magn. Reson. Med., vol. 57, no. 2, pp. 362–368, Feb. 2007, doi: 10.1002/mrm.21136.
M. A. Bernstein, M. Grgic, T. J. Brosnan, and N. J. Pelc, “Reconstructions of phase contrast, phased array multicoil data,” Magn. Reson. Med., vol. 32, no. 3, pp. 330–334, Sep. 1994, doi: 10.1002/mrm.1910320308.
P.-F. Van de Moortele, J. Pfeuffer, G. H. Glover, K. Ugurbil, and X. Hu, “Respiration-induced B0 fluctuations and their spatial distribution in the human brain at 7 Tesla,” Magn. Reson. Med., vol. 47, no. 5, pp. 888–895, May 2002, doi: 10.1002/mrm.10145.
S. J. Vannesjo et al., “Retrospective correction of physiological field fluctuations in high-field brain MRI using concurrent field monitoring,” Magn. Reson. Med., vol. 73, no. 5, pp. 1833–1843, May 2015, doi: 10.1002/mrm.25303.
K. P. Pruessmann, M. Weiger, M. B. Scheidegger, and P. Boesiger, “SENSE: sensitivity encoding for fast MRI,” Magn. Reson. Med., vol. 42, no. 5, pp. 952–962, Nov. 1999.
R. Topfer, F. Schweser, A. Deistung, J. R. Reichenbach, and A. H. Wilman, “SHARP edges: recovering cortical phase contrast through harmonic extension,” Magn. Reson. Med., vol. 73, no. 2, pp. 851–856, Feb. 2015, doi: 10.1002/mrm.25148.
Y. P. Du and Z. Jin, “Simultaneous acquisition of MR angiography and venography (MRAV),” Magn. Reson. Med., vol. 59, no. 5, pp. 954–958, May 2008, doi: 10.1002/mrm.21581.

W. Bian et al., “Simultaneous imaging of radiation-induced cerebral microbleeds, arteries and veins, using a multiple gradient echo sequence at 7 Tesla,” J. Magn. Reson. Imaging JMRI, vol. 42, no. 2, pp. 269–279, Aug. 2015, doi: 10.1002/jmri.24802.
B. Bilgic, H. Ye, L. L. Wald, and K. Setsompop, “Simultaneous Time Interleaved MultiSlice (STIMS) for Rapid Susceptibility Weighted Acquisition,” NeuroImage, vol. 155, pp. 577–586, Jul. 2017, doi: 10.1016/j.neuroimage.2017.04.036.
W.-J. Do, S. H. Choi, and S.-H. Park, “Simultaneous Variable-Slab Dual-Echo TOF MR Angiography and Susceptibility-Weighted Imaging,” IEEE Trans. Med. Imaging, vol. 37, no. 7, pp. 1632–1640, Jul. 2018, doi: 10.1109/TMI.2018.2789923.
I. Chatnuntawech et al., “Single-step quantitative susceptibility mapping with variational penalties,” NMR Biomed., vol. 30, no. 4, Apr. 2017, doi: 10.1002/nbm.3570.
E. G. Larsson, D. Erdogmus, R. Yan, J. C. Principe, and J. R. Fitzsimmons, “SNR-optimality of sum-of-squares reconstruction for phased-array magnetic resonance imaging,” J. Magn. Reson. San Diego Calif 1997, vol. 163, no. 1, pp. 121–123, Jul. 2003, doi: 10.1016/s1090-7807(03)00132-0.
M. E. Fewel, B. G. Thompson, and J. T. Hoff, “Spontaneous intracerebral hemorrhage: a review,” Neurosurg. Focus, vol. 15, no. 4, p. E1, Oct. 2003.
S. Wharton, A. Schäfer, and R. Bowtell, “Susceptibility mapping in the human brain using threshold-based k-space division,” Magn. Reson. Med., vol. 63, no. 5, pp. 1292–1304, May 2010, doi: 10.1002/mrm.22334.
D. Zhou, J. Cho, J. Zhang, P. Spincemaille, and Y. Wang, “Susceptibility underestimation in a high-susceptibility phantom: Dependence on imaging resolution, magnitude contrast, and other parameters,” Magn. Reson. Med., vol. 78, no. 3, pp. 1080–1086, Sep. 2017, doi: 10.1002/mrm.26475.
S. Liu, J.-C. Brisset, J. Hu, E. M. Haacke, and Y. Ge, “Susceptibility weighted imaging and quantitative susceptibility mapping of the cerebral vasculature using ferumoxytol,” J. Magn. Reson. Imaging, vol. 47, no. 3, pp. 621–633, 2018, doi: 10.1002/jmri.25809.
A. M. Halefoglu and D. M. Yousem, “Susceptibility weighted imaging: Clinical applications and future directions,” World J. Radiol., vol. 10, no. 4, pp. 30–45, Apr. 2018, doi: 10.4329/wjr.v10.i4.30.
S. Liu et al., “Susceptibility-weighted imaging: current status and future directions,” NMR Biomed., vol. 30, no. 4, Apr. 2017, doi: 10.1002/nbm.3552.
A. Rauscher, J. Sedlacik, A. Deistung, H.-J. Mentzel, and J. R. Reichenbach, “Susceptibility Weighted Imaging: Data Acquisition, Image Reconstruction and Clinical Applications,” Z. Für Med. Phys., vol. 16, no. 4, pp. 240–250, Jan. 2006, doi: 10.1078/0939-3889-00322.
M. Wang, Y. Dai, Y. Han, E. M. Haacke, J. Dai, and D. Shi, “Susceptibility weighted imaging in detecting hemorrhage in acute cervical spinal cord injury,” Magn. Reson. Imaging, vol. 29, no. 3, pp. 365–373, Apr. 2011, doi: 10.1016/j.mri.2010.10.016.
E. M. Haacke and J. R. Reichenbach, Eds., Susceptibility Weighted Imaging in MRI: Basic Concepts and Clinical Applications, 1st edition. Hoboken, N.J: Wiley-Blackwell, 2011.
E. M. Haacke, Y. Xu, Y.-C. N. Cheng, and J. R. Reichenbach, “Susceptibility weighted imaging (SWI),” Magn. Reson. Med., vol. 52, no. 3, pp. 612–618, Sep. 2004, doi: 10.1002/mrm.20198.
T. Boeckh-Behrens et al., “Susceptibility-weighted angiography (SWAN) of cerebral veins and arteries compared to TOF-MRA,” Eur. J. Radiol., vol. 81, no. 6, pp. 1238–1245, Jun. 2012, doi: 10.1016/j.ejrad.2011.02.057.

C. Liu, W. Li, K. A. Tong, K. W. Yeom, and S. Kuzminski, “Susceptibility-weighted imaging and quantitative susceptibility mapping in the brain,” J. Magn. Reson. Imaging, vol. 42, no. 1, pp. 23–41, 2015, doi: 10.1002/jmri.24768.
S. R. S. Barnes and E. M. Haacke, “Susceptibility-weighted imaging: clinical angiographic applications,” Magn. Reson. Imaging Clin. N. Am., vol. 17, no. 1, pp. 47–61, Feb. 2009, doi: 10.1016/j.mric.2008.12.002.
S. Liu et al., “Susceptibility-weighted imaging: current status and future directions,” NMR Biomed., vol. 30, no. 4, Apr. 2017, doi: 10.1002/nbm.3552.
[140] E. M. Haacke, S. Mittal, Z. Wu, J. Neelavalli, and Y.-C. N. Cheng, “Susceptibility-Weighted Imaging: Technical Aspects and Clinical Applications, Part 1,” Am. J. Neuroradiol., vol. 30, no. 1, pp. 19–30, Jan. 2009, doi: 10.3174/ajnr.A1400.
S. Haller, E. M. Haacke, M. M. Thurnher, and F. Barkhof, “Susceptibility-weighted Imaging: Technical Essentials and Clinical Neurologic Applications,” Radiology, vol. 299, no. 1, pp. 3–26, Apr. 2021, doi: 10.1148/radiol.2021203071.
T. Nägele, U. Klose, W. Grodd, D. Petersen, and J. Tintera, “The effects of linearly increasing flip angles on 3D inflow MR angiography,” Magn. Reson. Med., vol. 31, no. 5, pp. 561–566, May 1994, doi: 10.1002/mrm.1910310515.
P. B. Roemer, W. A. Edelstein, C. E. Hayes, S. P. Souza, and O. M. Mueller, “The NMR phased array,” Magn. Reson. Med., vol. 16, no. 2, pp. 192–225, Nov. 1990, doi: 10.1002/mrm.1910160203.
Y. Xu and E. M. Haacke, “The role of voxel aspect ratio in determining apparent vascular phase behavior in susceptibility weighted imaging,” Magn. Reson. Imaging, vol. 24, no. 2, pp. 155–160, Feb. 2006, doi: 10.1016/j.mri.2005.10.030.
N.-K. Chen and P.-H. Wu, “The use of Fourier-domain analyses for unwrapping phase images of low SNR,” Magn. Reson. Med., vol. 82, no. 1, pp. 356–366, Jul. 2019, doi: 10.1002/mrm.27719.
F. W. Wehrli, A. Shimakawa, G. T. Gullberg, and J. R. MacFall, “Time-of-flight MR flow imaging: selective saturation recovery with gradient refocusing,” Radiology, vol. 160, no. 3, pp. 781–785, Sep. 1986, doi: 10.1148/radiology.160.3.3526407.
A. Deistung, E. Dittrich, J. Sedlacik, A. Rauscher, and J. R. Reichenbach, “ToF-SWI: simultaneous time of flight and fully flow compensated susceptibility weighted imaging,” J. Magn. Reson. Imaging JMRI, vol. 29, no. 6, pp. 1478–1484, Jun. 2009, doi: 10.1002/jmri.21673.
S. Tan et al., “Utility of quantitative susceptibility mapping and diffusion kurtosis imaging in the diagnosis of early Parkinson’s disease,” NeuroImage Clin., vol. 32, p. 102831, 2021, doi: 10.1016/j.nicl.2021.102831.
Y. Duerst et al., “Utility of real-time field control in T2 *-Weighted head MRI at 7T,” Magn. Reson. Med., vol. 76, no. 2, pp. 430–439, Aug. 2016, doi: 10.1002/mrm.25838.
N. He et al., “Visualizing the lateral habenula using susceptibility weighted imaging and quantitative susceptibility mapping,” Magn. Reson. Imaging, vol. 65, pp. 55–61, Jan. 2020, doi: 10.1016/j.mri.2019.09.005.
B. Wu, W. Li, A. Guidon, and C. Liu, “Whole brain susceptibility mapping using compressed sensing,” Magn. Reson. Med., vol. 67, no. 1, pp. 137–147, Jan. 2012, doi: 10.1002/mrm.23000.

H. Sun, Y. Ma, M. E. MacDonald, and G. B. Pike, “Whole head quantitative susceptibility mapping using a least-norm direct dipole inversion method,” NeuroImage, vol. 179, pp. 166–175, Oct. 2018, doi: 10.1016/j.neuroimage.2018.06.036.

W. Li et al., “Whole-Brain Arteriography and Venography Using Improved Velocity-Selective Saturation Pulse Trains,” Magn. Reson. Med., vol. 79, no. 4, pp. 2014–2023, Apr. 2018, doi: 10.1002/mrm.26864.

V. L. Feigin, C. M. M. Lawes, D. A. Bennett, S. L. Barker-Collo, and V. Parag, “Worldwide stroke incidence and early case fatality reported in 56 population-based studies: a systematic review,” Lancet Neurol., vol. 8, no. 4, pp. 355–369, Apr. 2009, doi: 10.1016/S1474-4422(09)70025-0.

M. Selim et al., “Deferoxamine mesylate in patients with intracerebral haemorrhage (i-DEF): a multicentre, randomised, placebo-controlled, double-blind phase 2 trial,” Lancet Neurol., vol. 18, no. 5, pp. 428–438, May 2019, doi: 10.1016/S1474-4422(19)30069-9.

B. Behrouzi et al., “Action of iron chelator on intramyocardial hemorrhage and cardiac remodeling following acute myocardial infarction,” Basic Res. Cardiol., vol. 115, no. 3, p. 24, Mar. 2020, doi: 10.1007/s00395-020-0782-6.

J. Wu, Y. Hua, R. F. Keep, T. Nakamura, J. T. Hoff, and G. Xi, “Iron and Iron-Handling Proteins in the Brain After Intracerebral Hemorrhage,” Stroke, vol. 34, no. 12, pp. 2964–2969, Dec. 2003, doi: 10.1161/01.STR.0000103140.52838.45.

D. S. Moore, W. I. Notz, and M. A. Fligner, The Basic Practice of Statistics. New York: W H Freeman & Co, 2015.